QUANTIFYING THE CONTRIBUTION OF MEAN FLOW AND EDDY ADVECTION TO THE WARM SST BIAS IN THE SOUTHEAST TROPICAL ATLANTIC REGION

A Dissertation

by

PIN LI

Submitted to the Office of Graduate and Professional Studies of
Texas A&M University
in partial fulfillment of the requirements for the degree of

DOCTOR OF PHILOSOPHY

Chair of Committee,	Ping Chang
Committee Members,	Xiaopei Lin
	Robert Hetland
	Achim Stössel
	Ramalingam Saravanan
Head of Department,	Shari Yvon-Lewis

August 2018

Major Subject: Oceanography

ABSTRACT

In current-generation climate models, the warm sea surface temperature (SST) bias problem is most commonly seen in the eastern boundary upwelling systems (EBUSs), and is most pronounced and most prevalent in the Southeast Tropical Atlantic (SETA) region. Previous studies have shown that the coastal wind pattern in this region, namely the Benguela low-level coastal jet (BLLCJ), is of great importance for the generation of such SST bias, because the coastal ocean circulation is highly sensitive to the off-shore structure of the wind forcing.

Using an eddy-resolving regional ocean model, we first show that the SST bias in the region is drastically reduced when forced with simulated winds from a high-resolution regional atmospheric model. We subsequently demonstrate that the SST bias is highly sensitive to the spatial structure of the wind stress curl (WSC). We also find that when the ocean model is forced by a realistic high-resolution wind, the ocean model resolution is of second order importance in reducing the SST bias. Furthermore, we use a double-time average (DTA) method to quantify the contribution of heat budget terms, and show that the horizontal advection contributes significantly to the SST bias.

We then examined the question: To what extent do ocean eddies play a role in balancing the coastal ocean heat budget and affecting the SST bias? By experimenting with a submesoscale eddy-permitting regional ocean model, we show that ocean eddies in the Southeast Tropical Atlantic region are most energetic near the Angola-Benguela Front (ABF), the Lüderitz Upwelling Cell region and the Agulhas Leakage region. In

these three regions, comparisons between the two model simulations forced with the low- vs high-resolution winds suggest that the SST bias is mainly generated by mean flow advection with ocean eddies playing the role of counteracting the warming induced by the mean flow advection in this region.

DEDICATION

I dedicate this dissertation to my fiancé, Yao Lu.

ACKNOWLEDGEMENTS

I would like to thank my committee chair, Dr. Ping Chang, who kept encouraging and guiding me through my Ph.D. study at Texas A&M University. Without his generous help, this dissertation would be impossible to complete.

I would also like to thank my committee members, Dr. Xiaopei Lin, Dr. Robert Hetland, Dr. Achim Stoessel, and Dr. Ramalingam Saravanan, for their suggestions and supports during the past few years.

I am also grateful for my colleagues at Texas A&M University for their help. I am extremely thankful for Dr. Jaison Kurian, who helped me selflessly with running models and analyzing the results. Without him, lots of the analyses in this dissertation would take much more time and even become impossible.

I would also express my gratitude to China Scholarship Council for financially supporting me during my first four year. I am also grateful for the Texas A&M University Supercomputing Facility and the Texas Advanced Computing Center (TACC) at the University of Texas in Austin. Only with the resources provided by them, all of the model simulations and data analyses in this dissertation can be processed so efficiently.

Finally, thanks to my mother and father for their love and encouragement and to my fiancé for her love and understanding. They have given me the courage not to give up to the difficulties in my Ph.D. years.

CONTRIBUTORS AND FUNDING SOURCES

This work was supervised by a dissertation committee consisting of Professor Ping Chang, Professor Xiaopei Lin, Professor Robert Hetland and Professor Achim Stoessel of the Department of Oceanography and Professor Ramalingam Saravanan of the Department of Atmospheric Science.

The figures analyzed for Chapter 3 was provided by Dr. Jaison Kurian. The Nansen CTD data analyzed in Chapter 3 was provided by Dr. Marcus Dengler, and the Benguela CTD data was provided by Dr. Martin Schmidt. All other work conducted for the dissertation was completed by the student independently.

Graduate study was supported by a fellowship from Texas A&M University and China Scholarship Council.

NOMENCLATURE

ABF	Angola-Benguela Front
AMIP	Atmospheric Model Intercomparison Project
AMSR-E	Advanced Microwave Scanning Radiometer on the Earth Observing System
AVHRR	Advanced Very High Resolution Radiometer
AVISO	Archiving, Validation, and Interpretation of Satellite Oceanographic data
BLLCJ	Benguela Low-Level Coastal Jet
CAM	Community Atmosphere Model
CFSR	Climate Forecast System Reanalysis
CMIP3	Coupled Model Intercomparison Project Phase 3
CMIP5	Coupled Model Intercomparison Project Phase 5
COARE	Coupled Ocean–Atmosphere Response Experiment
CORE2	Coordinated Ocean-ice Reference Experiments Version 2
CTD	Conductivity-Temperature-Depth
DTA	Double-Time Average
EBUS	Eastern Boundary Upwelling System
EHT	Eddy Heat Transport
EKE	Eddy Kinetic Energy
FAO	Food and Agricultural Organization of the United Nations
HYCOM	Hybrid Coordinate Ocean Model

KPP	K-Profile Parameterization
LLCJ	Low-Level Coastal Jet
MOM	Modular Ocean Model
NCEP	National Centers for Environment Prediction
OAflux	Objectively Analyzed air-sea Fluxes
OISST	Optimum Interpolation Sea Surface Temperature
PUC	Poleward Undercurrent
QuikSCAT	Quick Scatterometer
ROMS	Regional Ocean Modelling System
RRTMG	Rapid Radiative Transfer Model for General Circulation Models
SCOW	Scatterometer Climatology of Ocean Winds
SLA	Sea Level Anomaly
SRTM	Shuttle Radar Topography Mission
SSS	Sea Surface Salinity
SST	Sea Surface Temperature
SETA	Southeast Tropical Atlantic
WRF	Weather Research and Forecasting
WSC	Wind Stress Curl
YSU	Yonsei University

TABLE OF CONTENTS

Page

LIST OF FIGURES

Page

LIST OF TABLES

Page

CHAPTER I

GENERAL INTRODUCTION

1.1 Importance of Southeast Tropical Atlantic Region

The Southeast Tropical Atlantic (SETA) region holds special importance in global climate change studies, because of its direct linkage to local marine ecosystems and fisheries that bear far-reaching implications for economy and society of the coastal African nations in the region. To the north of this region, equatorial fluctuations associated with the Atlantic Niño (Zebiak 1993) are characterized by periods of anomalous warming during austral winter. Interactions between the Atlantic Niño and El Niño make this region an important component of the global climate system (Chiang and Sobel 2002; Chiang and Lintner 2005). To the south, the Angola-Benguela region is under the influence of the Benguela Niño events, which refer to the warm sea surface temperature (SST) anomaly that usually lasts for months on interannual time scales off the west coast of southern Africa (Shannon et al. 1986). These events can have profound impacts on the behavior of Angola-Benguela Front (ABF) and local sea surface temperature (SST) (Mohrholz et al. 2004). Moreover, the SST in the Benguela region is an important indicator of coastal upwelling, which brings nutrients to the surface, thus enhancing biological productivity and the commercial fishery yield (Rossi et al. 2008). Since local economy and governments depend heavily on the wellbeing of the marine ecosystem, it is highly beneficial for the region to develop predictive capability for long-term climate change and short-term climate variability in this region.

1.2 The Benguela SST Bias Problem in Current Generation Climate Models

Accurate climate predictions require climate models that are capable of faithfully simulating and representing both the mean state of climate and its variability. Satisfying this requirement has proven very challenging for the climate modeling community. Generations of climate models have exhibited major biases in the SETA region. In fact, coupled atmosphere-ocean climate model simulations underestimate upwelling in all eastern boundary upwelling systems (EBUSs), producing warm SST biases in reference to the observations (Fig.1.1). This warm SST bias problem is particularly severe and difficult to remove along the Benguela upwelling region. Recent improvements in atmosphere and ocean model resolution and physics have helped to significantly reduce the warm SST bias in the Peru-Chile and California EBUS in the Pacific, and the Canary EBUS in the north Atlantic. These model improvements, however, have had minimum effects on the bias in the Benguela region where the magnitude of the warm SST bias is typically above 5^{o}C (Grodsky et al. 2012, McClean et al. 2011; Delworth et al. 2012; Gent et al. 2010; Small et al. 2015). This SST bias has far-reaching consequences because 1) it weakens the credibility of climate models in simulating and projecting future climate change in this region, 2) it has strong remote influence on the simulation of tropical climate in global models (Xu et al. 2014a, Richter et al. 2014; Ding et al. 2015; Large and Danabasoglu 2006) and 3) this is one of the region with the most prominent SST warming trend over 20th century (Deser et al. 2010). Many attempts have been made to improve the warm SST bias problem in the SETA region.

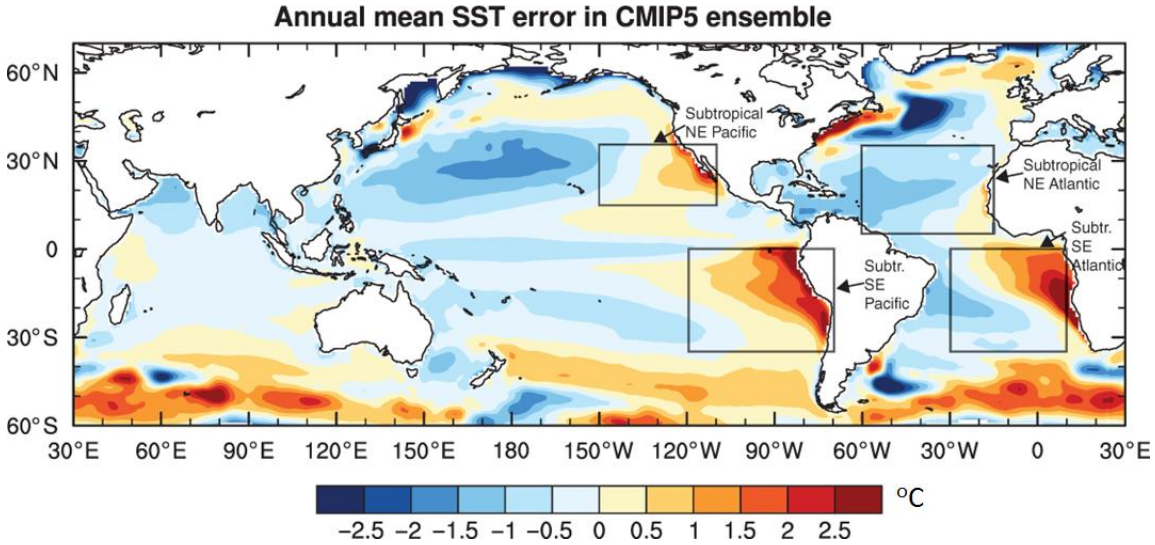

Fig.1.1 CMIP5 ensemble annual-mean SST error in the historical 1960–2004 integrations of 25 Fifth Assessment Report coupled GCMs relative to the OISST observations. Reprinted from Richter (2015).

One of the major features of EBUS is the strong equatorward flowing atmospheric low-level coastal jet (LLCJ) parallel to the coast, which is the main driver of the upwelling. The LLCJ is primarily caused by land-sea thermal contrast (Parish 2000) and the presence of a steep coastal terrain can increase its maximum speed and therefore determine the location of its core (Samelson 1992; Patricola and Chang 2017). A positive feedback appears to exist between the LLCJ and upwelling. The upwelling enhances the local land-ocean temperature contrast and intensifies the jet, which in turn intensifies the upwelling (Nicholson 2010). So any error in simulating the strength of the LLCJ can lead to a strong SST bias in the EBUS regions. The LLCJ in climate models is weak primarily because of the coarse resolution of atmospheric grid (>1^{o}), which cannot

adequately resolve LLCJ dynamics. While climate models with a relatively high horizontal resolution atmospheric grid (<0.5^o) improve the LLCJ simulation and significantly reduce the warm SST bias in the southeast tropical Pacific, the improvement is minimal in the Benguela upwelling region. For example, SST bias of 7^{o}C with 2^o or 1^o resolution atmospheric grid is only reduced to 5^{o}C with a 0.5^o resolution grid (Gent et al. 2010; Small et al. 2015). It appears that the LLCJ and the SST bias problems in the SETA region are more unique, and thus deserve a closer examination.

Remote forcing from the equatorial region has been suggested to contribute to the warm SST bias in the SETA region. In simulations with weaker zonal surface winds in the equatorial region (due to rainfall deficit in the Amazon basin, mainly in boreal spring), the equatorial thermocline is deeper and the cold tongue in the Eastern Equatorial Atlantic Ocean is warmer (Chang et al. 2007; Grodsky et al. 2012). This equatorial warm bias can be transported southward along the coast by the Angola Current, contributing to the SST bias around the ABF (Florenchie et al. 2003; Richter et al. 2010; Xu et al. 2014b; Lubbecke et al. 2010; Grodsky et al. 2012; Wahl et al. 2011). The lag of one month between the equatorial warming and that in the SETA region suggests the possibility of a remote influence from the equatorial region. However, remote influence alone cannot explain the observed warm SST bias in this region since it is always stronger than the equatorial SST bias or thermocline bias. Excessive rainfall in the southern tropical region and resulting high discharge of the Congo River can lead to excessive surface freshening and an extended barrier layer formation in the Gulf of

Guinea, which can lead to the erroneous SST warming in this region (Breugem et al. 2008; Grodsky et al. 2012). However, no obvious SST signal can be found due to Congo River discharge in the off-shore SETA region, and a temperature change of only $<0.25^{o}$C is found near the river mouth (Hopkins et al. 2013; White and Toumi 2014). Therefore, Congo River discharge is not considered as an important contributor to the SST bias in the SETA region.

Another prominent feature of EBUS systems is the presence of low-level stratocumulus cloud decks. Coupled climate models often underestimate the cloud deck, causing too much shortwave radiation to reach the ocean surface (Ma et al. 1996; Yu and Mechoso 1999; Huang et al. 2007; Chang et al. 2007) and a northerly wind anomaly along the coast (Nigam 1997). It has been argued that increased shortwave radiation directly heats the ocean surface while the northerly wind anomaly warms the ocean surface indirectly by reducing coastal upwelling. The additional shortwave radiation from lack of clouds is estimated around 40 W/m^2 in the Pacific (eg. de Szoeke et al. 2012, Coupled Model Intercomparison Project Phase 3 (CMIP3) ensemble) and 25 W/m^2 in the Atlantic (eg. Xu et al. 2014b, Coupled Model Intercomparison Project Phase 5 (CMIP5) ensemble). By comparing CMIP5 (Taylor et al. 2012) coupled models and Atmospheric Model Intercomparison Project (AMIP) experiment (within the CMIP5 archive) heat flux components to Objectively Analyzed air-sea Fluxes (OAflux, Yu et al. 2004) observations in the southeastern tropical Atlantic, Xu et al. (2014b) concluded that even with positive biases in the shortwave radiation, the net heat flux bias is negative (-50 up to -80 W/m2) because of the large errors in the longwave radiation and latent heat

flux. This is even true for atmosphere only models forced with observed SST. It thus appears that the deficiency in simulating low-level cloud does also not contribute significantly to the warm SST bias in the SETA region, and it cannot explain the higher than 5^{o}C bias in this region (Xu et al. 2014b; Large and Danabasoglu 2006; Wahl 2009).

More recent studies suggest that the coastal warm SST bias in the SETA region can be sensitive to the small-scale structure of the coastal winds. Errors in the position of the Benguela Low-Level Coast Jet (BLLCJ) jet core relative to the coast can change the prominent upwelling mechanism in the model, leading to the SST bias (Small et al. 2015). If the jet core is located near the coast, upwelling is driven by offshore transport of surface water due to Ekman divergence and a downwind (equatorward) coastal jet forms in the upper ocean (McCreary and Chao 1985; Fennel et al. 2012). On the other hand, if the jet core is located offshore, it induces a broad region of negative wind stress curl (WSC) associated with the weakening of winds towards the coast. The associated Ekman pumping (upward vertical velocity) will significantly enhance regional upwelling (Enriquez and Friehe 1995). According to Enriquez and Friehe (1995), a non-zero WSC can affect an area larger than its actual horizontal extent. Several studies have shown the strong impact of the WSC pattern on the regional coastal upwelling (Capet et al. 2004; Renault et al. 2012). The Benguela region features contributions from both Ekman divergence and Ekman pumping upwelling mechanisms because the BLLCJ is close to the coast at some locations and away from the coast at other locations (see Fig.1a of Patricola and Chang 2017). The core of the simulated BLLCJ in climate models is far offshore compared to observations because of their low horizontal resolution (Grodsky

et al. 2012; Small et al. 2015; Patricola and Chang 2017; Gent et al. 2010). If the WSC zone is sufficiently wide with a far offshore LLCJ, the coastal region will allow for the Sverdrup balance, modified by mixing to some extent, with the presence of deep poleward currents at the boundary (McCreary and Chao 1985; Fennel et al. 2012). This may explain the absence of the equatorward Benguela Current and the associated intense coastal upwelling in the Benguela upwelling region, as well as the common overshoot problem of the poleward Angola Current near the ABF in coarse resolution climate models, all contributing to the severe warm SST bias along the Benguela coast.

Coarse resolution (~1^o) ocean models are unable to simulate coastal upwelling dynamics including coastal Kelvin waves, horizontal heat advection through coastal currents and mesoscale eddies and filaments, even with realistic winds (Wahl 2009; Xu et al. 2014a; Colberg and Reason 2006; Grodsky et al. 2012). Around 17^oS latitude, the width of the first baroclinic Kelvin wave mode is <60 km (Colberg and Reason 2006; Veitch et al. 2010). Improving the resolution of either one or both components of coupled ocean-atmosphere models have shown to help reduce the SST bias significantly in the southeastern tropical Pacific but not in the Atlantic counterpart (McClean et al. 2011; Delworth et al. 2012; Gent et al. 2010). Small et al. (2015) reported an improvement of about 0.6^oC when ocean grid resolution is increased from 1^o to 7 km in the Atlantic region, similar to other studies (Seo et al. 2006; Doi et al. 2012). Both the Ekman pumping and Ekman divergence mechanisms were still weak in these models as indicated by a weak upward velocity (Small et al. 2015). However, since these studies all

have an erroneous BLLCJ structure, it remains to be examined how ocean model resolution can influence SST bias under a more realistic wind forcing.

Moreover, many recent advances have been made in understanding the dynamics and influence of mesoscale eddies in eastern boundary upwelling regions (Capet et al. 2008a; Capet et al. 2008b; Gruber et al. 2011; Capet et al. 2014). Evidence is mounting that ocean eddies make considerable contributions to global ocean transports of heat, salt, freshwater and chemical tracers (Jayne and Marotzke 2002; Volkov et al. 2008; Dong et al. 2014, Zhang et al. 2014). Since few of the current generation of climate models are capable of explicitly resolving ocean eddies, it remains generally unknown whether ocean eddies make a significant contribution to the warm SST bias in the Benguela region. However, modeling studies in other EBUSs, especially the Peru-Chile region, suggest that eddy heat transport can be a significant contributor to the ocean heat budget (Beckmann et al. 1994; Toniazzo et al. 2010; Colas et al. 2012). In particular, Beckmann et al. (1994) showed that by increasing the horizontal resolution of an ocean model from 1/3°x2/5° to 1/6°x1/5°, eddy kinetic energy (EKE) is significantly increased while the mean circulation does not alter substantially. Toniazzo et al. (2010) found that eddies contribute to the local upper-ocean heat budget at small spatial and temporal scales (several hundred kilometers and period of a year), even though their contribution is small over long time scales. A subsequent study by Colas et al. (2012) confirmed these results, and showed further that eddies in the Peru-Chile system are dominated by cyclonic eddies at the surface. Given the general similarity between the Peru-Chile and Benguela regions, it seems logical to postulate that resolving ocean eddies in climate

models may also be important in reducing SST biases in the SETA region. However, to the best of our knowledge, no studies up to now have attempted to address this issue. Although the Peru-Chile and Benguela regions share many similarities, the Benguela system has some unique features that make it more likely to be influenced by ocean eddies. For example, the ABF that has no counterpart in the Peru-Chile system creates a unique environment for potentially strong eddy-induced heat transport. Interestingly, the ABF is also the region where the strongest warm SST bias resides. This motivates us to undertake a systematic investigation about the role of ocean eddies in possibly reducing the strong warm SST bias in this region.

1.3 Overview of the Key Circulation Features

To help understand the mechanisms behind the formation of the warm SST bias, an introduction of basic circulations in the SETA region is given in this section. A schematic sketch of the main circulation structures in the South Atlantic Ocean is presented in Fig.1.2, which includes the SETA circulation system and shows the connections between the SETA region and other circulation systems such as the equatorial Atlantic Ocean, Southwest Tropical Atlantic Ocean and Southern Ocean.

The SETA region encompasses a region extending from the Gulf of Guinea to the southern tip of South Africa, including the coast of Angola, the ABF region, the Benguela upwelling region and Agulhas Leakage region. Based on satellite SST observations, Meeuwis and Lutjeharms (1990) show that the position of ABF varies from 14°S (austral winter) to 16°S (austral summer). To the south of this region, that of

the Agulhas Leakage is found near the Cape of Good Hope at 34.4°S. The upwelling events are induced by the equatorward coastal winds with strong seasonal variability (Risien et al. 2004), and are observed to be in the form of multiple bathymetry-directed upwelling cells with cold-water centers (Shannon and Nelson 1996; Weeks et al. 2006).

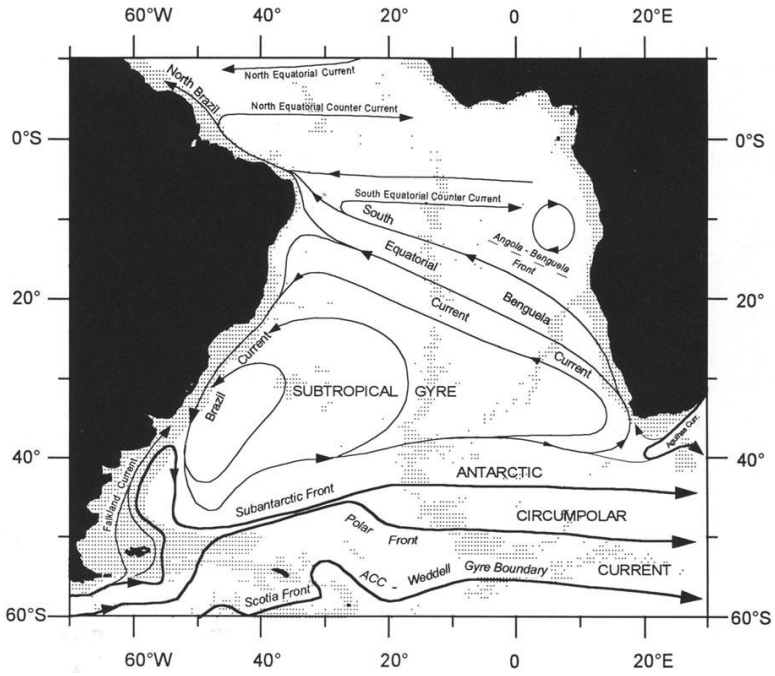

Fig.1.2 Schematic representation of the large-scale surface circulation features in the South Atlantic Ocean. Reprinted from Schneider et al. (1996).

The dominant current within the Benguela upwelling region is the Benguela Current, which is an equatorward eastern boundary current of the Southern Atlantic Ocean. The spatial structure of the Benguela Current has been thoroughly described (Defant 1961; Reid et al. 1977; Fu 1981; Tsuchiya 1985; Reid 1989; Stramma and Peterson 1989): it starts at the Cape of God Hope and flows northward in a relatively

narrow band along the African coast, before it flows northwestward leaving the coast at approximately 30 °S while broadening rapidly. The Benguela Current is primarily fed by the South Atlantic Current, the southern band of the subtropical gyre (Stramma and Peterson 1990), the Agulhas Current and the Subantarctic Surface Water (Shannon et al. 1989).

1.4 Objectives of the Study

Inspired by previous studies and theories, the prime objectives of this study is to assess and quantify the importance of resolving fine structures of the BLLCJ and ocean eddies in reducing the warm SST bias. We will conduct and compare suites of regional ocean model simulations in the SETA region by 1) using low-resolution vs. high-resolution atmosphere forcing and 2) varying ocean model horizontal resolutions to test the following scientific hypotheses:

Hypothesis I: The fine spatial structure of the BLLCJ has a fundamental influence on the coastal circulation and associated SST along the Angola-Benguela coast. Only the high-resolution atmospheric forcing that adequately resolves the fine spatial structure of the BLLCJ can give a realistic representation of the coastal circulation and SST distribution along the Angola-Benguela coast.

Hypothesis II: Ocean eddies play a secondary but important role in maintaining the ocean budget along the Angola-Benguela coast, particularly in eddy active regions such as the ABF and Lüderitz Upwelling Cell region. However, the role of ocean eddies

depends on whether the atmospheric forcing resolves the fine spatial structure of the BLLCJ.

The organization of this dissertation is as follows. Chapter 2 describes the modeling tool, atmospheric forcing datasets, model sensitivity experiments and observational datasets to validate the simulations. Chapter 3 tests hypothesis I by comparing two sets of model sensitivity experiments forced respectively by a high- vs. low-resolution atmospheric forcing. Chapter 4 tests hypothesis II by analyzing and comparing a pair of eddy-resolving ocean model simulations. Chapter 5 summarizes the major findings of the study and discusses the implications of these findings for reducing model biases in global climate models.

CHAPTER II

DATASETS AND MODEL EXPERIMENTS

2.1 Datasets

Reanalysis and observational datasets used for model experiments and validation are described in this chapter. Datasets during the period from 1987 to 2004 are used for the spin-up simulation and from 2005 to 2009 for model sensitivity experiments and model-data comparison analyses

2.1.1 Ocean Reanalysis Data

The ocean component of the Climate Forecast System Reanalysis (CFSR) product (Saha et al. 2010) is used to provide initial and boundary conditions, constraining regional ocean model simulations at the lateral boundaries and sea surface salinity (SSS) at the ocean surface. CFSR is a coupled atmosphere-ocean-land surface-sea ice product. The ocean model used in CFSR is Modular Ocean Model (MOM4p0d) in which a 3DVAR data assimilation module is used to assimilate temperature and salinity observations from historical hydrographic measurement, including fixed mooring arrays and Argo floats. When direct salinity observations are not available, synthetic salinity profiles are estimated using local climatological T-S correlation. Temperature and salinity in the top model level are relaxed to gridded fields of observed SST and SSS. CFSR ocean reanalysis has 40 vertical levels, 0.5^{o} horizontal resolution and hourly time resolution. As argued by Xu et al. (2014b), CFSR data have realistic

representation of SST and temperature distribution, coastal currents and upwelling in the SETA. According to more recent studies (Kopte et al. 2017; Tchipalanga et al. 2018), the salinity bias of CFSR products can be as large as 0.6 compared with Conductivity-Temperature-Depth (CTD) observations, but temperature bias is less severe, which is close to 0 near the ocean surface, and gradually increases to about 1^{o}C at 500 m depth. The original CFSR ocean data is sampled hourly, but a 5-day mean dataset is derived for model-data comparison analyses in this study.

2.1.2 Atmospheric Forcing Dataset

The Coordinated Ocean-ice Reference Experiments Version 2 (CORE2) dataset (Large and Yeager 2008), designed as a common dataset to force ocean models, is used in this study. CORE2 is a set of globally gridded atmospheric variables that are used to compute air-sea momentum, heat and fresh-water fluxes. It is based on a combination of National Centers for Environment Prediction (NCEP) reanalysis and satellite observations with a focus on reducing biases and limitations of the reanalysis. In particular, winds from NCEP are corrected for magnitude and direction using 2000-2004 Quick Scatterometer (QuikSCAT) satellite wind observations. The CORE2 dataset provides 6 hourly near surface atmospheric variables on a global grid of ~1.875^{o} resolution.

The CORE2 resolution is rather low and there is no currently available high-resolution common dataset for forcing ocean models. To test the ocean model sensitivity to atmospheric forcing resolution, we thus use a high-resolution dataset from a set of

regional atmospheric model simulations forced with observed SST at the atmosphere lower boundary and reanalysis along the lateral boundaries. Patricola and Chang (2017) described the regional atmospheric simulations in detail, which were based on the Weather Research and Forecasting (WRF) model (Skamarock et al. 2008). WRF is a non-hydrostatic terrain-following regional climate model. The high-resolution forcing dataset used in this study is derived from the WRF experiment with 27 km horizontal grid and 32 vertical levels in a Southeast Tropical Atlantic domain between 52^{o}S-32^{o}N and 22^{o}W-25^{o}E (see Patricola and Chang 2017). The set of physical parameterizations for this WRF experiment includes the Community Atmosphere Model (CAM) microphysics, Rapid Radiative Transfer Model for General Circulation Models (RRTMG) radiation, Yonsei University (YSU) planetary boundary layer, a Monin–Obukhov surface scheme, the Noah land-surface model and the Zhang and McFarlane cumulus scheme. Comparison with satellite observations of surface winds shows that the 27 km WRF model is able to reproduce observed features of BLLCJ in terms of strength, spatial pattern, location of jet core and the double jet-core structure. Forcing variables derived from the 9 km WRF experiment in Patricola and Chang (2017) are also used to force the regional ocean model, but after a careful examination we decide against using them due to biases in the shortwave radiation in the Benguela offshore region that give rise to a warm SST bias. These biases seemingly arise from the lack of convective parameterization in the 9 km WRF experiment, as discussed in Patricola and Chang (2017).

2.1.3 Global Observed Dataset

In order to validate simulated SST, Reynold's daily Optimum Interpolation Sea Surface Temperature (OISST) analysis version 2.0 on a 0.25^{o} grid (Reynolds et al. 2007) is used. This is a blended product using satellite observation from AVHRR and Advanced Microwave Scanning Radiometer on the Earth Observing System (AMSR-E) and in situ data from ships and buoys. Infrared measurements from Advanced Very High Resolution Radiometer (AVHRR) yield accurate high-resolution data near land, whereas AMSR-E provides measurement in most weather conditions in the open ocean. Platform differences and sensor biases are accounted for by a bias adjustment procedure and the final data is interpolated to fill in gaps.

In addition, sea level anomaly (SLA) from the Archiving, Validation, and Interpretation of Satellite Oceanographic data (AVISO) is used. It is a multi-mission product which processes satellite data from all altimeter missions. This gridded product has a $1/4^{o}$ (approximately 27 km) horizontal resolution, with weekly sampling frequency. The anomaly is calculated with respect to a twenty-year mean sea level height. Since the first baroclinic Rossby deformation radius represents the spatial scale of baroclinic eddies (Pedlosky 2013), datasets with finer resolution should be able to resolve such eddies. In the SETA region, the first baroclinic Rossby deformation radius is around 50 km in the ABF region and decreases to around 30 km in the Lüderitz Upwelling Cell region (Chelton et al. 1998), where eddies are robust (see Chapter 1). Therefore, the AVISO SLA data is capable of resolving eddies and can be used to validate the model geostrophic eddy fields (Chaigneau et al. 2008).

2.1.4 In Situ 3-D Observations

CTD datasets are obtained from the Nansen Program, which is performed by Food and Agricultural Organization of the United Nations (FAO) and is funded by the Norwegian government. This program mainly focuses on the ocean near the African coast and few other countries (Bianchi et al. 2016), and acquires bi-annual hydrographic and velocity data from the Angolan continental margin during the main downwelling and upwelling seasons for the period of 1995-2014. In this study, we have obtained the Nansen CTD temperature data from 2006 to 2009 to validate the general vertical structures of model experiments, because our main experiments and analysis covers that period (see details in section 2.2). During this period, Nansen CTD observation locations, and locations grouped into February-April (austral summer) and June-August (austral winter) are shown in Fig.2.1. The data available between 100 m and 800 m depth are considered for the analysis here. Out of the 2303 stations available during 2006-2009, 1838 stations are within the 100-800 m depth range. Out of these 1838 stations, 955 are in austral summer and 790 are in austral winter. There is no data quality information available with the CTD data and hence it is assumed that the quality flags were already applied.

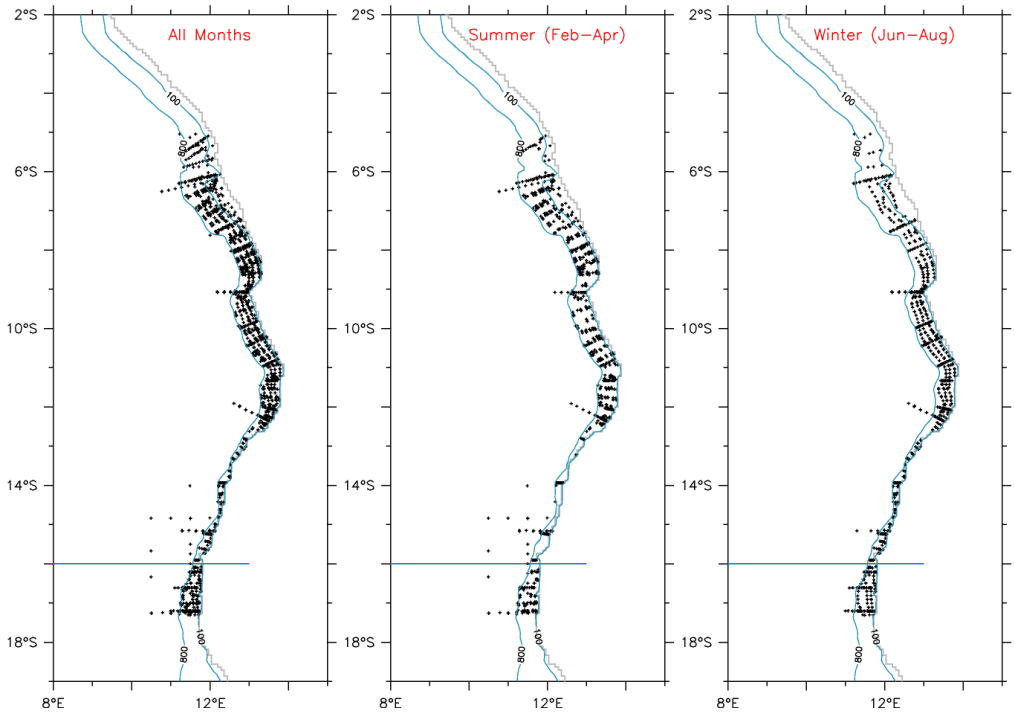

Fig.2.1 Nansen CTD stations during 2006-2009 period, showing all months (left), February-April (middle, austral summer) and June-August (right, austral winter) period. The thin gray line indicates the coastline and blue contours show the 100 m and 800 m isobaths. The data between these two isobaths are used for our analysis. The blue line at 16°S indicates the location of Angola-Benguela Front (ABF).

In addition, we also use the Benguela CTD observations to validate simulations. This dataset is provided by Martin Schmidt from the Leibniz Institute for Baltic Sea Research at Warnewünde, Germany (http://thredds-iow.io-warnemuende.de/thredds/dodsC/benguela). Only three sections in 2008 are available during the 2006-2009 period along latitudes 23°S (on 17-May-2008) and 17°S (on 22-May-2008), and roughly along longitude 12°E (on 17-Mar-2008) (Fig.2.2). The salinity and temperature data is interpolated to a dx=constant (km) based X-axis. This data is also interpolated to a dz=constant Z-axis. Time information, latitude and longitude of the original CTD

stations are available with the interpolated data. In addition, the distance of original stations from the near-coastal station (considered as 0 km) is also available.

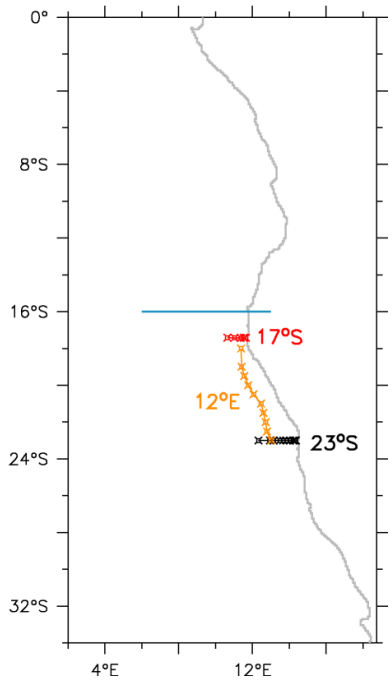

Fig.2.2 Benguela CTD sections in 2008, near 23°S (on 17-MAY-2008), 17°S (on 22-MAY-2008) and 12°E (on 17-MAR-2008). The blue line shows the location of ABF.

2.2 Model and Experiments

The SETA SST bias in coupled climate models is strong (>6°C) and extends further offshore from the West Africa coast as a single pattern (see Fig.1 in Delworth et al. (2012) for example) compared to that in ocean-only simulations (Large and Danabasoglu 2006; Grodsky et al. 2012). This is because the coastal SST bias in the coupled model can be amplified and spread offshore through atmosphere-ocean interaction and feedback (Grodsky et al. 2012). As stated in Chapter 1, the focus of this

study is on the coastal SST bias. As such, to examine the impact of resolving fine structures of the near-coastal winds on the coastal SST bias in the SETA region, this study employs different resolution atmospheric fields to force an ocean-only model to isolate the contribution of various oceanic and atmospheric processes to the SST bias. The following gives some details of the model and experiment design.

2.2.1 Regional Ocean Model and Model Physics Options

The Regional Ocean Modelling System (ROMS) model (Haidvogel et al. 2008; Shchepetkin and McWilliams 2005) is used for all the experiments in this study. ROMS is a primitive-equation, free-surface, split-explicit oceanic model. ROMS solves the three dimensional hydrostatic equations using horizontal curvilinear coordinates and a "z-sigma" or "s" vertical coordinate system (Lemarié et al. 2012; Shchepetkin and McWilliams 2009). All configurations in this study use harmonic horizontal mixing of momentum and tracers, the K-Profile Parameterization (KPP) scheme (Large et al. 1994) for vertical mixing, 4th-order Akima horizontal and vertical tracer advection, and the Coupled Ocean–Atmosphere Response Experiment (COARE) 3.0 bulk formulation (Fairall et al. 2003) for computing the atmospheric fluxes using input atmospheric surface variables, such as winds, air-temperature, humidity, etc.. The open lateral boundary conditions consist of a combination of radiation and nudging schemes for the three-dimensional velocity and tracers. Specifically, the Chapman (1985) scheme is used for the free-surface and the Flather (1976) scheme for the two-dimensional velocities. At the bottom, a quadratic bottom drag with coefficient Cd = 0.003 is used.

2.2.2 Model Configuration

As the study focuses on the SST bias along the West Africa coast, the model domain covers the region between 16^{o}W-24^{o}E and 48^{o}S-13^{o}N with a closed boundary to the north (Fig.2.3). Model bathymetry is from the Shuttle Radar Topography Mission (SRTM30) dataset (Becker et al. 2009) with a depth range of 10-5700 m and smoothed on the model horizontal grid to reduce horizontal pressure gradient errors associated with sigma-coordinates using the Sikiric et al. (2009) method. After smoothing, the maximum slope factor (rx0) for any two adjacent grid point is 0.25 and maximum hydrostatic inconsistency number or Haney number (rx1), which measures the horizontal pressure gradient error, is 7. All configurations use 50 sigma-layers in the vertical and their spacing is set by the surface stretching parameter (θ_S) of 10, bottom stretching parameter (θ_B) of 2, and a surface/bottom layer width of 400 m. For a water depth of 150 m (typical for the Benguela upwelling region), the vertical grid has around 2 m resolution in the upper 70 m and about 4 m resolution around 100 m depth. Since the model does not include river runoff forcing and there are two major rivers draining into the model domain (Niger and Congo), the model SSS is relaxed to CFSR reanalyzed SSS. Over a 6-grid point wide buffer zone at open lateral boundaries, model tracer and momentum fields are nudged to prescribed reanalysis data for a smooth transition from the outer boundary condition to the interior model solution.

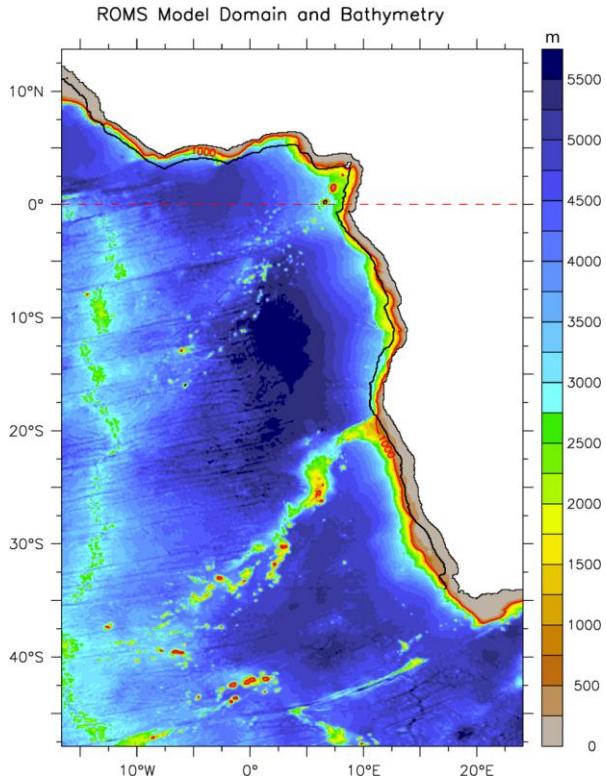

Fig.2.3 The model domain and bathymetry (color shading, from SRTM30 (Becker et al. 2009) dataset) of the 9 km ROMS grid. The red contour shows the 1000 m bathymetry and dashed red line shows the equator. The black contour parallel to the coastline marks the 30 grid point wide coastal zone, which is used for various near-coastal averaging calculations used in this study. The model domain is similar for other configurations with 3, 27 and 81 km resolutions used in this study. The WRF regional model solutions used in this study from Patricola and Chang (2017) have a slightly larger domain than that shown here.

2.2.3 Model Sensitivity Experiments

This study focuses on the formation of the coastal warm SST bias in the SETA region for a given atmospheric forcing. The main two physical factors considered in this study include: strength and spatial structure of the coastal winds, particularly the BLLCJ, and the increase of the horizontal resolution of the ocean model toward resolving ocean

eddies and the associated eddy heat transport. For these reasons, two sets of ROMS experiments are designed in this study, and are described below.

All sensitivity experiments start from a restart condition on 1 January 2005, which comes from an 18-year spinup run from 1987 to 2004. The spinup run is forced with CORE2 atmospheric data with the ocean initial and boundary conditions from the CFSR dataset. Model sensitivity experiments are run from January 2005 to December 2009 with identical CFSR boundary conditions. Two sets of sensitivity runs are carried out, differing only in their atmospheric forcing: one comes from the low-resolution CORE2 and the other comes from the high-resolution (27 km) WRF simulation described above. The coarse resolution CORE2 dataset used in the first set of experiments is representative of the resolution of the atmosphere in a typical climate model, leading to a poor representation of the BLLCJ (Patricola and Chang 2017). The high-resolution atmospheric forcing used in the second set of experiments has been shown to have a more realistic representation of BLLCJ based on satellite wind observations by Patricola and Chang (2017). 10-day mean outputs are archived for analysis of all experiments except for the 3 km ROMS simulations where daily mean fields are saved in order to evaluate the role of eddy heat transport in SST biases. This is because 10-day average model output may potentially smooth out short temporal scale eddy activities and daily average output may be more accurate for analyzing eddy heat transport contributions.

In order to test the impact of ocean model horizontal resolution, each set of ROMS sensitivity experiments described above contains 4 different horizontal resolution

runs, ranging from 81, 27, 9 to 3 km. The coarsest resolution at 81 km is comparable to 1^o resolution of ocean grids used in typical climate models. All other resolutions are higher than typical high-resolution global climate model simulations at ~0.5^o. We consider 81 km as non-eddy permitting, 27 km as mesoscale eddy permitting, 9 km as mesoscale eddy resolving and 3 km as submesoscale eddy permitting. All cases are spun-up from 1987-2004, except for the 3 km simulation since it is computationally too intensive. The restart condition for the 3 km experiment is interpolated from that of the 9 km experiment on 01-January-2005. For each case, a grid appropriate time step and a nudging time scale have been used to ensure numerical stability but all other settings and options remain the same. All of the above described experiments are labeled with the grid resolution and the respective atmospheric forcing product. For example, 3 km ROMS simulations forced by CORE2 and 27 km WRF forcing are named as 3km_CORE2 and 3km_WRF27, respectively.

In addition to the above sets of sensitivity experiments, a few other sensitivity experiments have been carried out to distinguish the relative contribution of the winds, heat fluxes and the northern core of BLLCJ, which locates near the ABF region at 16^oS. Since the warm SST bias develops within a few months of the model run, all these additional sensitivity experiments are run for one year (year 2005) on the 9 km ROMS grid. The relative importance of wind and heat flux are tested in two new atmospheric forcing combinations obtained by 1) replacing the winds in CORE2 dataset with that from the WRF winds and 2) replacing the winds in WRF forcing by that in CORE2. The heat flux fields in each dataset were kept the same for these experiments. The impact of

the northern core of BLLCJ on the warm bias is tested in another experiment, with the location of the winds of the northern core of the BLLCJ in the WRF dataset being replaced by its mean location. Note that in these two sensitivity runs the forcing was derived from the 9 km WRF simulation rather than the 27 km WRF simulation. Similar simulations with the 27 km WRF forcing have not yet been completed. Table 1 summarizes all sensitivity runs and their abbreviated names.

Table 1 Sensitivity runs and abbreviated names

Oceanic Resolution	Atmospheric Forcing	Integration Time	Output Frequency	Abbreviated Names
3 km	CORE2	2005-2009	Daily	3km_CORE2
9 km	CORE2	2005-2009	10-day	9km_CORE2
27 km	CORE2	2005-2009	10-day	27km_CORE2
81 km	CORE2	2005-2009	10-day	81km_CORE2
3 km	WRF27	2005-2009	Daily	3km_WRF27
9 km	WRF27	2005-2009	10-day	9km_WRF27
27 km	WRF27	2005-2009	10-day	27km_WRF27
81 km	WRF27	2005-2009	10-day	81km_WRF27
9 km	WRF09 with CORE2 winds	2005	10-day	9km_WRF09CW
9 km	CORE2 with WRF09 winds	2005	10-day	9km_CORE2WW
9 km	WRF27 with no northern core	2005	10-day	9km_WRF27NN

CHAPTER III

IMPACT OF OCEAN MODEL RESOLUTION AND BLLCJ SPATIAL STRUCTURE ON SST BIAS

3.1 Introduction

As introduced in Chapter 1, various atmospheric and oceanic origins have been suggested as a possible source for the warm SST bias in the SETA region in previous studies. The lack of stratocumulus clouds in the upwelling region in climate models and the erroneous representation of the barrier layer formation in the tropical Atlantic were found to be less effective contributors to the warm bias. Instead, the inability of climate models to realistically represent the equatorial trade winds and the BLLCJ along the coast of West Africa was consistently shown to be a more fundamental cause of the bias problem in the SETA region. However, most of the previous studies are based on relatively coarse resolution atmospheric models (~1^{o}) that cannot fully resolve the spatial structure of the BLLCJ. Recently, Small et al. (2015) have shown that the location of the BLLCJ core can have a direct impact on the coastal circulation along the Benguela coast. By manually shifting the BLLCJ core towards the coast by ~100 km, they show that Ekman divergence can be significantly increased, leading to a reduction in the warm SST bias along the Benguela upwelling region by 3-4^{o}C.

The SETA region is unique compared to other EBUSs in terms of both atmospheric and oceanic regional circulations. In the atmosphere, the BLLCJ is a dominant feature along the coast. However, the detailed structure of the BLLCJ was not well documented

until the very recent work by Patricola and Chang (2017), who used the high-resolution satellite-based Scatterometer Climatology of Ocean Winds (SCOW) data (Risien and Chelton 2008) to reveal detailed structures of the BLLCJ. Unlike its counterpart along the west coast of South America, a double-core structure can be identified in the BLLCJ, with its northern core near the location of the ABF (17.5°S) and southern core near the Lüderitz Upwelling Cell (25-30°S). The BLLCJ shows strong seasonality, with the northern core reaching its peak in austral fall and spring, and the southern core in summer and spring. Both cores are located very close to the coast, which forms a strong and narrow WSC band along the coast. In order to fully resolve the fine and rich structure of the BLLCJ, high-resolution atmospheric models are required in the SETA region, but may not be a necessity in other LLCJ regions.

In the ocean, the SETA region also has unique features compared to the southeast tropical Pacific. Two of the most prominent features are 1) the southward flowing (from equatorial region) warm coastal current, known as the Angola Current, extending from the equatorial region to about 15°-17°S and 2) the strong SST front between ~15°S and ~17°S known as the ABF where the Angola Current meets the northward flowing cold Benguela Current (Shannon et al. 1987; Lass et al. 2000). Any error in simulating these two features can lead to a large error in SST over this region. For example, an erroneously strong Angola Current can transport more warm water to the south, contributing to a warm SST bias. The Benguela Current and WSC to the north of the ABF control its location (Colberg and Reason 2006) and any error in local winds can lead to a shift in its position and strength. If the Benguela Current is too weak due to

errors in the BLLCJ and upwelling, the Angola Current can also overshoot and transport warm equatorial waters southward, leading to a strong SST bias in this region (Grodsky et al. 2012; Xu et al. 2014a; Xu et al. 2014b).

Note that the ABF coincides with the northern core of the BLLCJ, whereas the Lüderitz Cell is located at the southern core of the BLLCJ. This leads to the first hypothesis that the regional ocean circulations and associated SST structures depend on the details of the overlying BLLCJ. Among the possible oceanic mechanisms that cause the warm SST bias, a too weak Benguela Current, causing an underestimate of horizontal advection of cold water and a southward shift in position of the ABF, is found to be a credible contributor to the formation of the warm SST bias. But only few systematic studies have investigated the mechanism under different spatial structures of the BLLCJ in relation to the warm SST bias. Moreover, the impact of ocean model resolution on the warm SST bias is also not fully examined. Following Small et al. (2015) and Patricola and Chang (2017), this chapter aims to investigate how ocean model resolutions and the spatial structure and strength of the BLLCJ affect the formation of the warm SST bias in SETA. Our investigation will utilize both high-resolution atmospheric forcing fields and high-resolution ocean models that are capable of resolving the fine structures in both the ocean and atmosphere.

The chapter is organized as follows. Section 3.2 introduces the analysis strategy. Section 3.3 examines the annual mean SST bias and the impact of ocean model horizontal resolutions on the bias. Section 3.4 analyzes the seasonal cycle and spatial structure of the coastal circulation. Section 3.5 focuses on the impact of the BLLCJ

strength and spatial structure on the bias. Section 3.6 presents the results of a double-time average analysis of the upper ocean heat budget. Section 3.7 and 3.8 provide discussions and conclusions.

3.2 Analysis Strategy

This study uses ROMS at various spatial resolutions forced with low-resolution and high-resolution atmospheric data, respectively, the latter of which is capable of explicitly resolving the observed double-core structure of the BLLCJ (see Chapter 2). This is needed to investigate the effect of the detailed structure of the BLLCJ on the coastal circulation and the associated temperature and salinity structure that relate to the SST bias problem. The sensitivity experiments with varying model horizontal resolutions (from a non-eddy permitting grid of 81 km to a submesoscale eddy permitting grid of 3 km) and different atmospheric forcing (~1.75^{o} CORE2 forcing and a 27 km resolution WRF model simulation), as well as a few other sensitivity experiments are conducted and analyzed in this chapter to understand the relative importance of resolving small-scale features in the atmospheric forcing field vs. in the ocean circulation in reducing the warm SST bias. In this section, we provide a brief discussion on the analysis strategy used to test the scientific hypothesis.

3.2.1 Datasets

The data analysis and presentation of results are organized around topics related to features of the SST bias in the model simulation and possible mechanisms causing the

SST bias. The realism of model simulations with respect to observations is addressed under each of these topics. All analyses use model outputs and compare them to observational data and reanalysis data during 2006-2009 except for the heat budget analyses for model simulations that use model outputs for the entire simulation period of 2005-2009. Annual climatology fields are analyzed for most purposes except for the seasonal comparisons and heat budget. For comparison purposes, satellite observational and reanalysis data are linearly interpolated to the model horizontal grids and a common vertical grid when required.

For in situ observational datasets, model simulations are treated differently to compare with different datasets. Before comparing with the Nansen CTD data, ROMS outputs are interpolated to the time and location of Nansen CTD observations (during the 2006-2009 period for all CTD stations within the 100-800 m depth range) and then followed by the same procedure for latitude-binning to obtain the latitude-depth sections. This is to keep the model outputs consistent with CDT observations, allowing a direct model-data comparison. After resampling the model outputs, all data (both CTD and model) available for February-April period is averaged into 0.5^{o} latitude bins between $17.5\text{-}5.0^{o}$S to get a mean latitude-depth section of temperature or salinity for austral summer. This procedure is repeated for austral winter season (June-August). A similar procedure is applied to compare model results with the Benguela CTD dataset.

3.2.2 Heat Budget Analysis and Double-time Average Method

The heat budget analysis, which estimates the contribution of different physical

processes to the warm SST bias in the SETA region, is performed using the model output of temperature equation diagnostic terms, i.e. temperature tendency, total advection and total diffusion. It is guaranteed by the model that the summation of total advection and total diffusion balances the temperature tendency. However, as argued by Madec (2008) and Oerder et al. (2016), taking a direct time average of the heat budget terms may cause difficulties interpreting the contribution from various physical terms to the heat budget in the climatological sense. Therefore, as a remedy, Oerder et al. (2016) proposed a substitute method, termed as double-time average (DTA) method, to perform the heat budget analysis.

The DTA of temperature reads:

$$\langle T \rangle = \frac{\int_{to}^{t1} T dt}{\Delta t} = \frac{\iint_{to}^{t1} \frac{\partial T}{\partial t} dt^2}{(\Delta t)} + T_0, \quad (1)$$

where ⟨T⟩ represents the long term average of temperature, T_0 the initial temperature, to is the initial time, $t1$ the final time, and Δt the integration time period. In discretized form, equation (1) is rewritten as:

$$\langle T \rangle = \frac{\sum_{n=1}^{Nstep} T \delta t}{\Delta t} = \frac{\sum_{n=1}^{Nstep} \sum_{p=1}^{n} \frac{\partial T}{\partial t} \delta t^2}{(\Delta t)} + T_0. \quad (2)$$

In equation (2), δt denotes the sampling time interval of model outputs. Accordingly, in this study δt is 1 day for the experiments with 3 km ocean horizontal resolution, and 10 days for all other experiments. In addition, $\frac{\partial T}{\partial t}$ represents the average tendency of that period, which can be replaced by any particular heat budget term that contributes to the tendency.

Note that the DTA method in (1) and (2) depends on the initial temperature T_0. Since the pair of ROMS runs forced by the coarse-resolution CORE2 and fine-resolution WRF have the same initial condition, the difference between the DTA temperatures <T> derived from these runs will eliminate the influence of the initial temperature T_0 on the heat budget. And such temperature difference is only contributed by the heat budget term (e.g. total advection) that is calculated using DTA method. Therefore, in the following discussions, the DTA method is only applied to the difference of the heat budgets between the pair of CORE2- and WRF-forced runs.

To validate the feasibility of the DTA method, we first compare the climatological temperature difference between the pair of CORE2- and WRF-forced runs computed using direct model temperature output to that calculated using the DTA method based on the model output of temperature tendency according to (2). Once the results are validated, a comparison of different heat budget terms between CORE2-forced and WRF-forced ROMS experiments will be made.

3.3 Annual Mean SST Bias and Impact of Ocean Model Horizontal Resolutions

We use the 9 km ROMS simulations as a reference in this chapter. The annual climatology of the simulated SST from the 9km_CORE2 and 9km_WRF runs is compared to the observed SST from the Reynolds dataset in Fig.3.1. The spatial pattern and value of SST of the model simulations generally match with that of the observations except in the coastal region of the African continent. While 9km_CORE2 lacks the

presence of upwelled cold water in the Benguela region, the upwelled cold water in 9km_WRF is not transported far enough offshore.

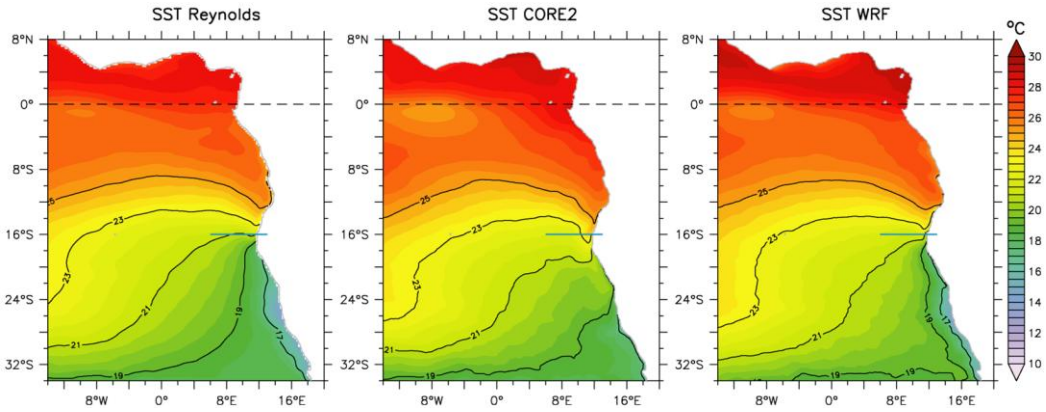

Fig.3.1 2006-2009 mean SST (^{o}C) from Reynolds observational data (left) and from the 9km_CORE2 (middle) and 9km_WRF27 experiments (right). Selected contours are marked in black. The dashed line marks the equator and the light blue line marks the Angola-Benguela Front location.

The impact of horizontal resolution of ocean model grid is explored in Fig.3.2. With CORE2 forcing, the overall pattern of the SST bias and its magnitude are similar for all ocean model resolutions (Fig.3.2a-d). Two distinct patches of SST bias above 1^{o}C appear along the coast, one to the north of 12^{o}S with a maximum bias of about 2^{o}C and one to the south of it with a maximum bias of about 4^{o}C. The highest SST bias in the northern patch varies between 2.1^{o}C (on the 81, 27 and 9 km grids) to 2.9^{o}C (on the 3 km grid). For the southern patch, it is in the range of 4.0^{o}C (3 km grid) to 4.8^{o}C (27 km grid). The total area of SST bias above 1^{o}C decreases slightly from about 100x10^{4} km^{2} in 81 km to about 82x10^{4} km^{2} in 9 km, with a slight increase to 85x10^{4} km^{2} in case of 3 km. The discontinuity in the coastal bias and the higher magnitude of the SST bias in the

Benguela upwelling region shows that different mechanisms may be contributing to these biases north and south of 12°S. Outside of these patches, the bias is generally below 0.8°C with the exception of a smaller patch of a weak cold bias (~-1°C) in the equatorial region centered about 6°W.

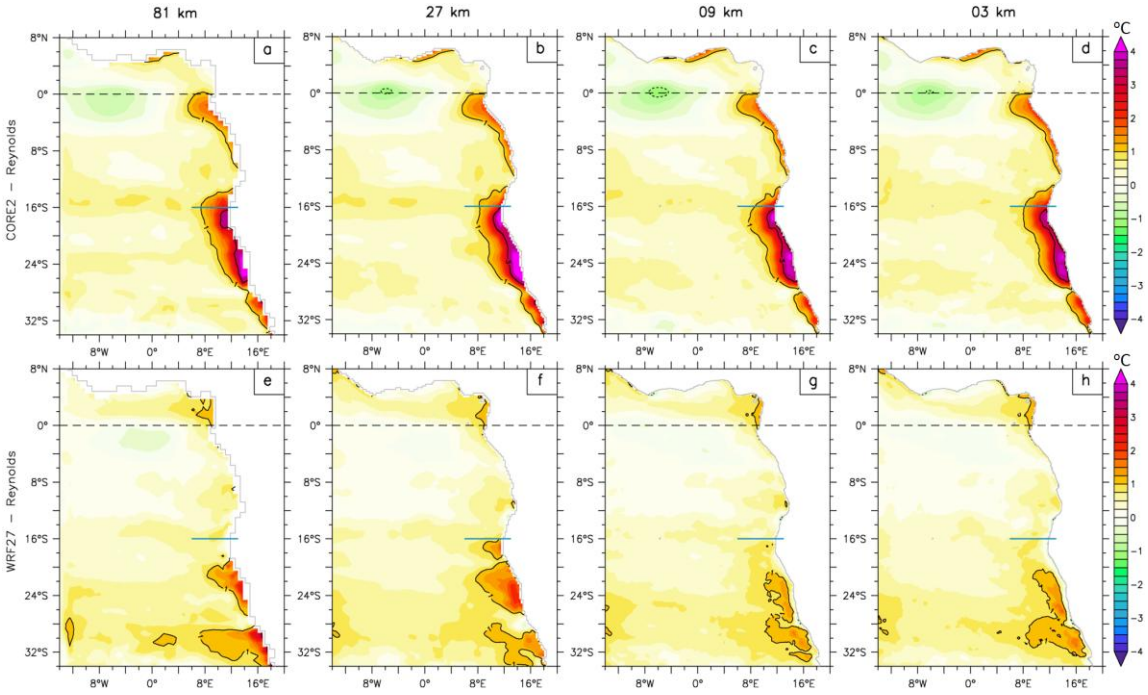

Fig.3.2 2006-2009 mean SST bias (°C) in CORE2-forced (upper panel) and WRF27-forced (lower panel) runs with respect to Reynolds observations. From left to right, ROMS grid resolution increases from 81 km to 3 km. Contours are shown for the 1 and 3°C SST biases.

The SST bias is significantly reduced in the set of WRF27-forced runs (Fig.3.2e-h), with a complete absence of bias above 1°C between 12°S and the equator at all model resolutions. To the south of 12°S, the magnitude and area of the SST bias are significantly reduced in the WRF27-forced runs compared to the CORE2-forced runs. In this region, the SST bias appears in multiple small patches rather than extending

systematically along the whole coastline as in the CORE2-forced runs. In contrast to the insensitivity of the SST bias to model resolutions in the CORE2-forced runs, there is a marked sensitivity to ocean model resolution change in the WRF27-forced runs. The maximum value of SST bias in WRF27-forced runs is in the range of 1.6^{o}C (9 km grid), but increases to 3.1^{o}C (81 km grid). For the 3, 9 and 27 km grids, the improvement in maximum SST bias is about 2.2-2.5^{o}C relative to the CORE2-forced runs. Compared to the CORE2-forced runs, the maximum reduction in the bias area (SST bias above 1^{o}C between 33^{o}S-12^{o}S) is for 9km_WRF (41%) and the minimum reduction is for 27km_WRF (7%). While the CORE2-forced runs show the maximum SST bias hugging the coast, it emerges slightly offshore and in multiple small patches in the WRF27-forced runs. For the 9km_WRF and 3km_WRF, the maximum SST biases are not attached to the coast (Fig.3.2g-h). Comparing the WRF27-forced runs at different ocean grid resolutions has the advantage of resolving mesoscale eddies at 9 km grid and permitting submesoscale eddies at 3 km grid. For both the 9km_WRF and 3km_WRF, the maximum SST bias is around 1.6^{o}C, which is significantly smaller than what is being achieved with the 81km_WRF and 27km_WRF forcing (Figs. 3). In particular, there is a significant reduction in the area (~43%) and magnitude (~0.5^{o}C) of the SST bias in the Benguela upwelling region when the grid resolution increases from 27 km to 9 km (Fig.3.2f-g). The offshore region has a small (< 0.75^{o}C) positive bias but over a slightly smaller area than that in the CORE2-forced runs. The cold bias in the equatorial region is rather broad in the WRF27-forced runs with maximum values about -0.25^{o}C.

This comparison shows that the combination of a high-resolution atmospheric forcing that resolves the BLLCJ and a high-resolution (<~9 km) ocean model which resolves coastal upwelling and mesoscale eddies helps reducing the warm SST bias. The lack of any such improvement with the coarse resolution CORE2 forcing (Fig.3.2a-d) shows that the increasing ocean model resolution alone does not lead to a significant reduction of the SST bias. Even with an 81 km ocean grid that is close to typical climate model resolution, the high-resolution (27 km) atmospheric forcing critically reduces the SST bias, both in terms of area and magnitude (Fig.3.2a and e). This clearly shows that resolving the fine structure of the atmosphere is more important for reducing the SST bias along the Benguela coast than resolving mesoscale ocean processes. However, there is a significant reduction in the maximum amplitude and area of the SST bias when the ocean model resolution increases from 27 km to 9 km but not from 9 km to 3 km. At 9 km and 3 km resolution the ocean model resolves the near-coastal upwelling and the associated ocean mesoscale processes better than at 27 km and 81 km, as evidenced by the near zero SST bias in the inner coastal zone (less than 100 km from the coast) (Fig.3.2g-h). Warm SST bias of values above 1^{o}C outside this inner coastal zone indicates that model still needs improvements in the representation of both the strength of upwelling and the offshore advection of upwelled cold water. This intercomparison analysis clearly shows that a 9 km horizontal resolution for the ocean model is able to reduce the warm SST bias significantly when forced with a high-resolution atmospheric forcing capable of resolving the fine structure of the coastal winds. For all subsequent

analysis presented in this Chapter, we focus on the results from the 9 km ROMS simulations.

3.4 Seasonal Cycle and Spatial Structure of the Coastal Region

3.4.1 Comparison with In Situ Observations

In situ observations in the SETA region are very sparse. Until recently, only a few published observational studies were available for this region, raising concern about the quality of ocean reanalysis products, such as CFSR. As introduced in Chapter 2, the Nansen CDT dataset and Benguela CTD dataset are used to validate the model outputs, the sampling method of which was introduced in section 3.2.

The general pattern of near coastal temperature of the model simulation matches well with that of the CTD observations (Fig.3.3 and Fig.3.4). In the 9km_CORE2 run, for the austral summer season (February-April) the temperature of the upper 50 m is significantly higher than that of the CTD observations owing to the anomalously strong Angola current transporting warm equatorial waters southward along the coast (Fig.3.3, middle panels). Below 50 m depth, the 9km_CORE2 run shows a slight cold bias of about 1^{o}C. The agreement is much better between the observations and 9km_WRF27 run in both surface and deeper ocean. This is attributed to the more realistic simulation of the Angola Current and the associated coastal dynamics owing to the more accurate near-coastal winds in WRF27 compared to CORE2. For the austral winter season (June-August), the 9km_WRF27 run also shows a better agreement with the CTD observations than the 9km_CORE2 run. The pronounced difference between the 9km_CORE2 and

the 9km_WRF27 runs around 13^{o}S could result from the low number of CTD observations available close to this latitude compared to other regions.

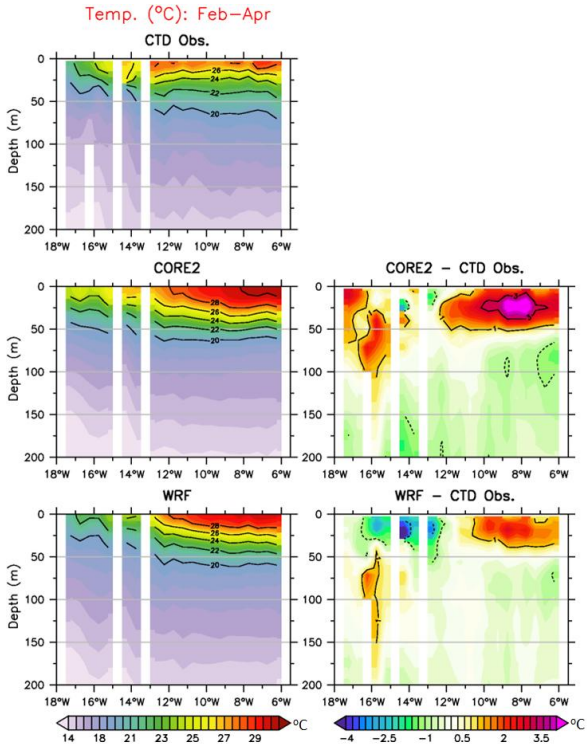

Fig.3.3 Near-coastal depth-longitude sections of temperature from CTD observations (top) and ROMS experiments (middle & lower, left panels), and the difference between them (middle and lower, right panels) for the austral summer (Feb-Apr) months of years 2006-2009. The white stripes indicate missing data.

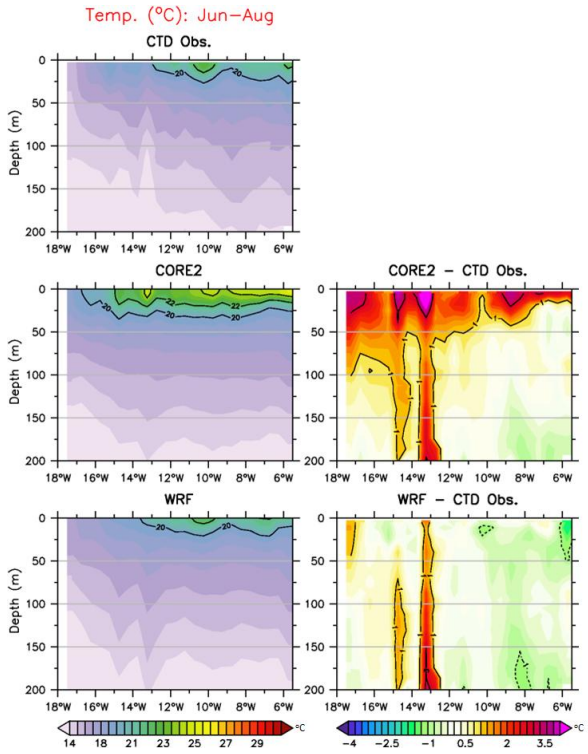

Fig.3.4 Near-coastal depth-latitude section of temperature from CTD observations (top) and ROMS experiments (middle & lower, left panels) and the difference between them (middle and lower, right panels) for the austral winter months (June-August) months. The white region in plots indicates missing data.

Salinity comparison (Fig.3.5 and Fig.3.6) also shows a similar pattern to the temperature. Broad features like low-salinity waters near surface close to the equator and high-salinity waters below it are well reproduced in both experiments. The 9km_CORE2 run has excessive low-salinity water near surface, again resulting from overly strong Angola current transporting low-salinity water from the equatorial region. The high-salinity water pattern below surface is well reproduced in the 9km_WRF27 run rather than that in 9km_CORE2.

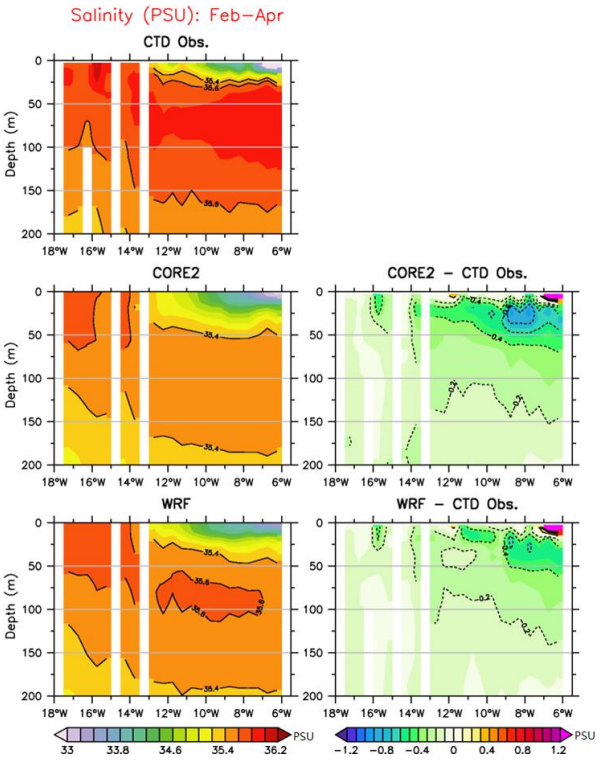

Fig.3.5 Near-coastal depth-latitude section of salinity (PSU) from CTD observations (top) and ROMS experiments (middle & lower, left panels) and the difference between them (middle and lower, right panels) for the austral summer (Feb-Apr) months. The white region in plots indicates missing data.

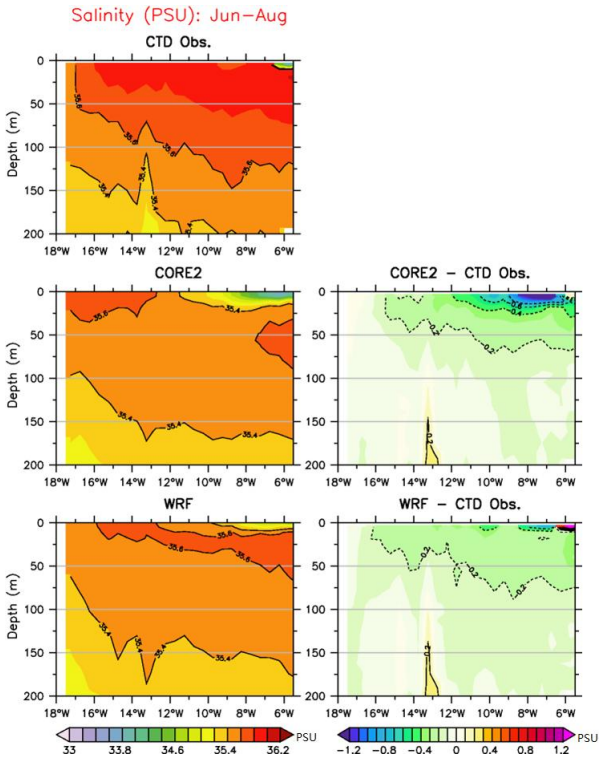

Fig.3.6 Near-coastal depth-latitude section of salinity (PSU) from CTD observations (top) and ROMS experiments (middle & lower, left panels) and the difference between them (middle and lower, right panels) for the austral winter months (June-August) months. The white region in plots indicates missing data.

Similar comparisons are performed between the model simulations and the Benguela CTD data. SST and general spatial distribution of temperature is better simulated in the 9km_WRF27 run than in the 9km_CORE2 run (Fig.3.7), although along the 23^{o}S section the upwelling and the coastal-offshore temperature simulated by 9km_WRF27 run is still weaker than that in the CTD measurement. Also, the 9km_WRF27 run is not able to simulate fine-scale features observed at the 12^{o}E CTD section (Fig.3.7, bottom panel). However for the 9km_CORE2 run, the simulated

temperature is consistently much too warm near the surface in all sections compared to the observations and isotherms tilt to a wrong direction along 23°S and 17°S.

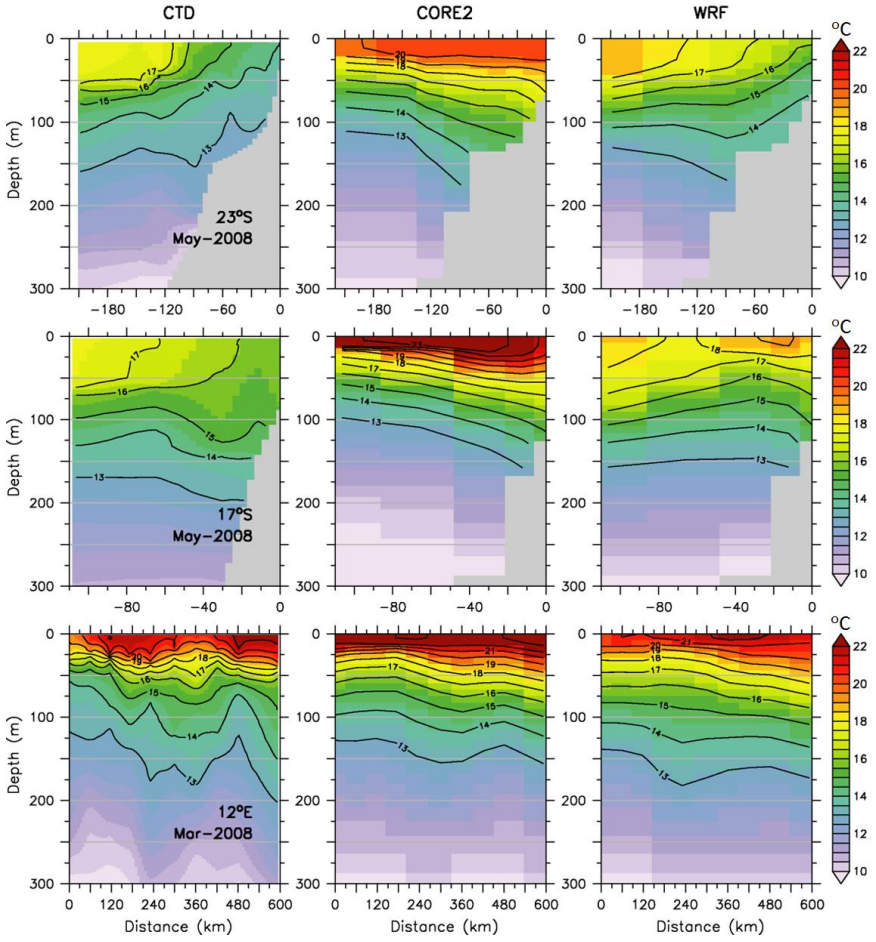

Fig.3.7 Comparison of temperature (°C) between the Benguela CTD data and ROMS simulations. The grey shading indicates bathymetry in case of model and bathymetry or missing data in case of CTD observations. Selected isotherms are shown in black contours. The distance (km) on upper and middle rows is the offshore (westward) distance from near-coastal CTD location and for the lower row is the northward distance from the southern-most CTD location.

In terms of salinity (Fig.3.8), at 23°S, salinity in the CDT observation and the 9km_WRF27 run has a deep mixed layer with salinity lower than 35.4 in the upper 100-

200 m, while the 9km_CORE2 run has shallower mixed layer with salinity decreasing rapidly from 35.6 near the surface to 35.2 near 100 m depth. At 17^{o}S, the 9km_WRF27 run fails to reproduce the deeper mixed layer near the coast seen in the CTD observations. However, such problem can also be seen in the 9km_CORE2 run and even more serious. Along approximately 12^{o}E, both 9km_CORE2 and 9km_WRF27 runs can reproduce the general structure of salinity, but does not resolve the fine structures as observed in the CTD data. Collectively, the 9km_WRF27 run is also more realistic than the 9km_CORE2 run in terms of salinity distribution too.

Comparisons with both Nansen and Benguela CTD datasets suggest that generally the 9km_WRF27 run can simulate a much better spatial structure of the observed 3-D temperature and salinity than the 9km_CORE2 run. Therefore, the 9km_WRF27 run will be used in the following sections to show the influence of a more realistic BLLCJ on not only the surface ocean, but also on the subsurface ocean. The 9km_CORE2 run, on the other hand, serves as a comparison to show the impact of a poorly represented BLLCJ as an ocean model forcing.

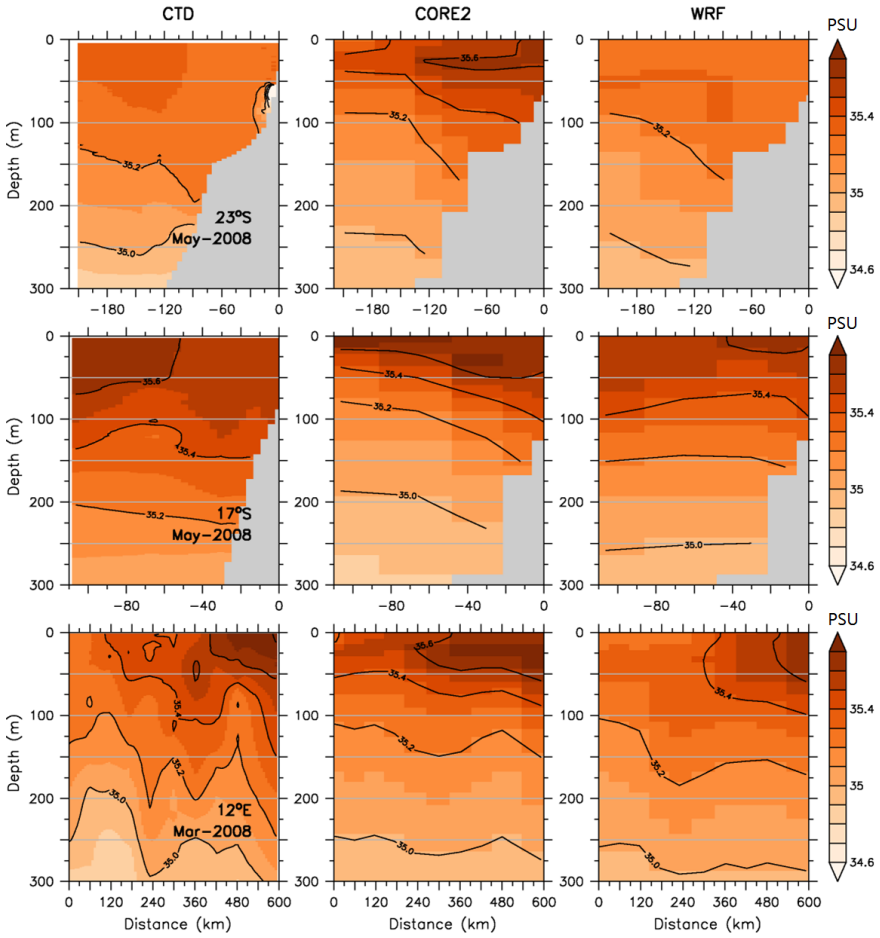

Fig.3.8 Comparison of salinity (PSU) between the Benguela CTD data and ROMS simulations. The grey shading indicates bathymetry in case of model and bathymetry or missing data in case of CTD observations. Selected isotherms are shown in black contours. The distance (km) on upper and middle rows is the offshore (westward) distance from near-coastal CTD location and for the lower row is the northward distance from the southern-most CTD location.

3.4.2 Seasonal Cycle of Coastal SST

The seasonal cycle of coastal SST from both the 9km_CORE2 run and the 9km_WRF27 run are compared to Reynolds SST (Fig.3.9) using an average over ~1^{o} wide coastal stripe (15 grid points from the model coast line, on the 9-km ROMS grid; see Fig.2.3). In observation, SSTs are warmer and the 17^{o}C (roughly represents the

boundary of upwelled cold water) isotherm is in its southernmost position (24^{o}S) during December-March period (Fig.3.9a). SSTs are the coolest along the coast and the 17^{o}C isotherm reaches its northernmost location (~17^{o}S) during July-September. A well-defined ABF is visible as strong SST gradient at about 16^{o}S throughout the year (Fig.3.9a). Compared to the observations, the 9km_CORE2 run always has a weaker ABF and a southward displaced location. The upwelling is weak south of the ABF and SST cooler than 17^{o}C is visible only during July-October to the south of 26^{o}S. In the 9km_WRF27 run, the position of 17^{o}C isotherm is remarkably close to the observations throughout the months (Fig.3.9c). In addition, the cooling during June-September occurred between the ABF and equatorial region, marked by the position of 25^{o}C isotherm, is also very well simulated in the 9km_WRF27 run compared to the 9km_CORE2 run. However, the SST during April-May is warmer than observations between equator and 12^{o}S. The simulated ABF is slightly less sharp compared to that in observation (Fig.3.9a and c). Overall the 9km_WRF27 run is able to simulate the observed seasonal cycle of SST within the inner coastal zone remarkably well.

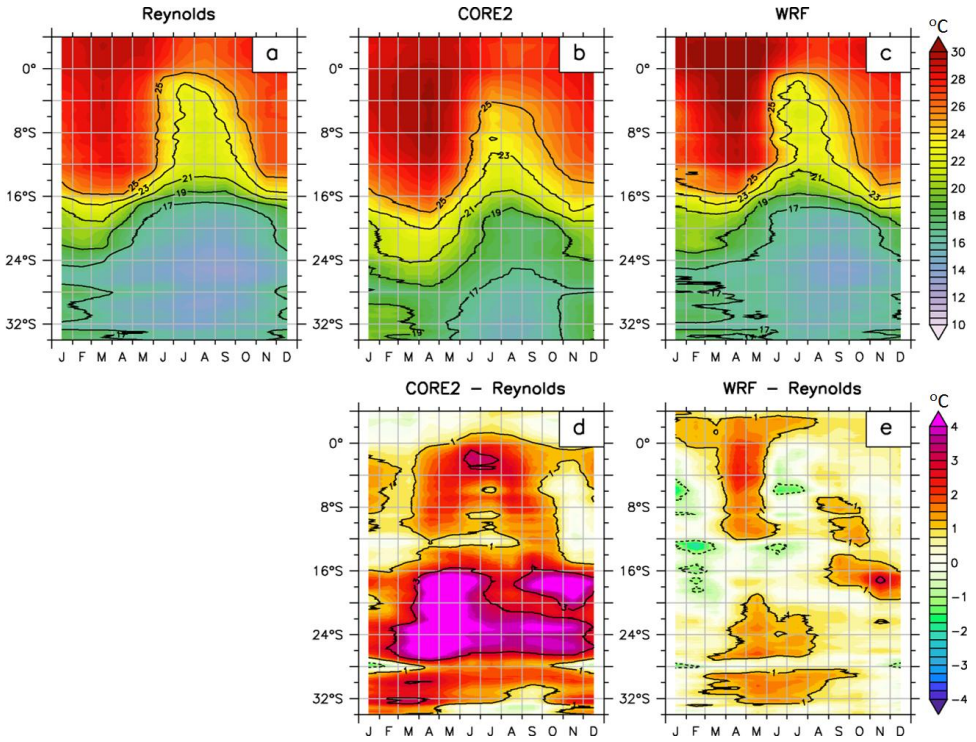

Fig.3.9 Seasonal cycle of SST (^{o}C, upper panels) and SST difference (^{o}C, lower panels) averaged over ~1^{o} wide coastal stripe (15 grid points from the coastline of 9-km ROMS grid, see Fig.3.1.3). Data shown is the monthly climatology for 2006-2009 period. Reynolds data has been interpolated to 9-km ROMS grid before plotting.

3.4.3 Coastal Temperature Structure

One of the major reasons suggested for the formation of climate model SST bias in the SETA region is the lack of coastal upwelling. In order to evaluate upwelling from the 9km_CORE2 run and the 9km_WRF27 run, we analyze and compare vertical section of temperature (2006-2009 annual mean) along 24^{o}S (latitude where SST bias is maximum in the 9km_CORE2 run, see Fig.3.2c) in Fig.3.10 and along a 1^{o} wide coastal stripe (see Fig.2.3) in Fig.3.11. CFSR Reanalysis data is used as a validation of model simulations, even though the reanalysis itself may contain large errors. We note that CFSR

assimilates SST using the Reynolds data and hence the SST from CFSR is nearly identical to that from Reynolds data used for the SST validation.

The general upwelling structure at 24^{o}S in the CFSR, shown by the upward sloping isotherms towards the coast, is well reproduced in the 9km_WRF27 run but not so in the 9km_CORE2 run (Fig.3.10a-c). The shallowest position of isotherms occurs close to the coast in both CFSR and the 9km_WRF27 run, indicating that both the Ekman pumping caused by wind stress curl and Ekman transport caused by the alongshore winds are maximum close to the coast. In contrast, in the 9km_CORE2 run, the shallowest positions of 13^{o}-15^{o}C isotherms occur at about 100-200 km away from the coast and then slopes downward to the coast. This indicates that the upwelling circulation is very weak at the coast but becomes slightly stronger away from the coast. However, close to the coastline a very weak and shallow (<50 m depth) upwelling is present over few grid points (Fig.3.10b). The slope of the isotherms between CFSR and the 9km_WRF27 run indicates that the strong upwelling in the 9km_WRF27 run exists only over a narrow region within the inner coastal zone compared to a wider region in the CFSR. As a consequence, the near coastal temperature in the 9km_WRF27 run is slightly warmer than that in CFSR (Fig.3.9e). The 9km_CORE2 run has very large temperature bias near the coast due to the weak and shallow upwelling (Fig.3.10d). The large cold bias seen in the 9km_CORE2 run at offshore between 50 and 300 m depth also has contributions from the subsurface upwelling away from the cost.

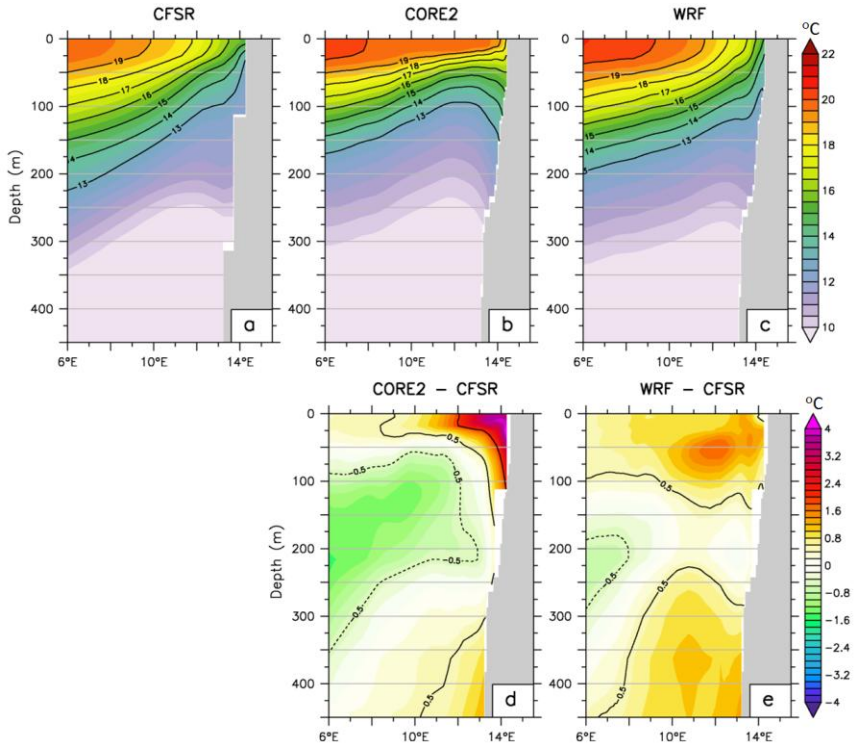

Fig.3.10 Temperature (^{o}C, top panels) and temperature difference (^{o}C, bottom panels) along 24^{o}S from CFSR Reanalysis data and from the 9km_CORE2 run and the 9km_WRF27 run. Mean data for 2006-2009 period is shown here. Grey shading indicate topography.

The inner coastal temperature comparison in Fig.3.11 shows that the 9km_WRF27 run reproduces temperature vertical structure that is much closer to that of CFSR. This close agreement between CFSR and the 9km_WRF27 run includes the position of the ABF at about 16^{o}S, outcropping latitude of isotherms 18-24^{o}C and the overall upwelling structure in the Benguela region (30-20^{o}S). However, a less sharp thermocline in the Angola region (to the north of the ABF) and a weaker upwelling in the Benguela region lead to warm temperatures in the upper 150 m, with a maximum of 2^{o}C bias to the north of ABF (Fig.3.11e). the 9km_CORE2 run has very large subsurface warm bias reaching 4^{o}C in both the region north of ABF and in the Benguela upwelling region (Fig.3.11d).

The bias in the Angola region appears to originate from both a diffused thermocline and southward transport of warm waters from the equatorial region by the Angola Current (Fig.3.11b). A less sharp ABF and southward overshooting of warm waters about ABF are clearly visible in the 9km_CORE2 run (Fig.3.11b). The temperature bias in the Benguela upwelling region extends below 100 m with the maximum at the surface.

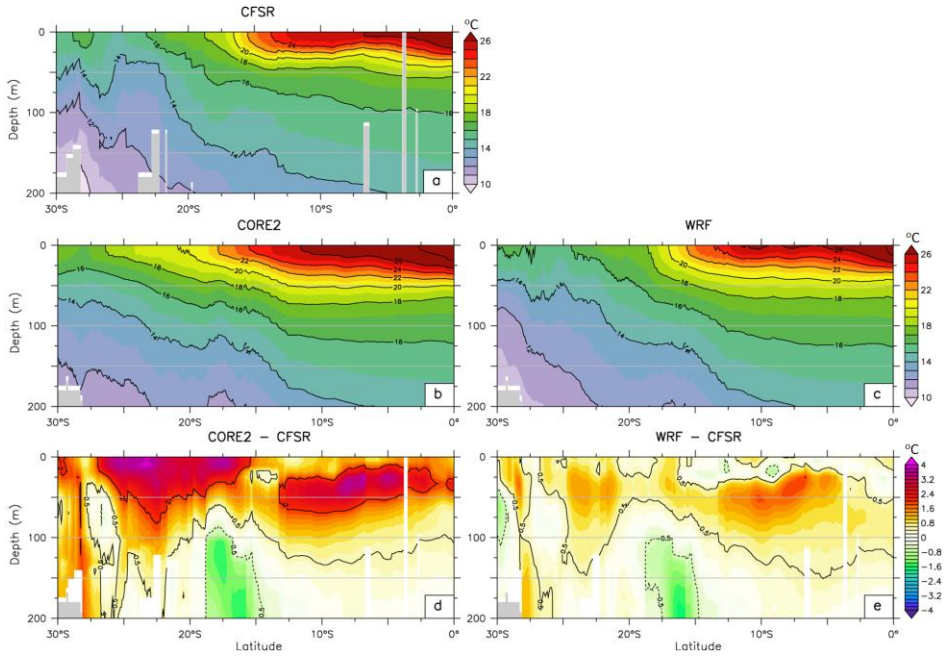

Fig.3.11 As in Fig.3.2.9, but temperature (a-c) and temperature difference (e-f) averaged over 15 grid points (9 km grid, roughly 1o longitude in width) across the coastal region. Grey shading indicates topography (from CFSR in (a) and from ROMS 9 km grid in (b)-(e)).

3.4.4 Coastal Currents

The role of coastal currents in the formation of warm SST bias is explored in Fig.3.12. In the 9km_CORE2 run the southward flowing Angola Current near the surface is strong and broad and overshoots to the south of ABF up to about 30^{o}S. The

northward flowing Benguela Current, on the other hand, is completely absent, consistent with the near absence of the Benguela coastal upwelling. The near surface Angola Current is less organized and weak in the 9km_WRF27 run and does not extend beyond the ABF region. A strong, well-organized Benguela Current is seen in the 9km_WRF27 run, companying with the strong coastal upwelling (Fig.3.10c). The difference between surface currents in 9km_CORE2 and 9km_WRF27 runs clearly shows the much stronger southward surface flow all along the coast from the equatorial region in the 9km_CORE2 run than in the 9km_WRF27 run. This comparison confirms many aspects of the upwelling and coastal currents contribution to the formation of warm SST bias in the SETA region.

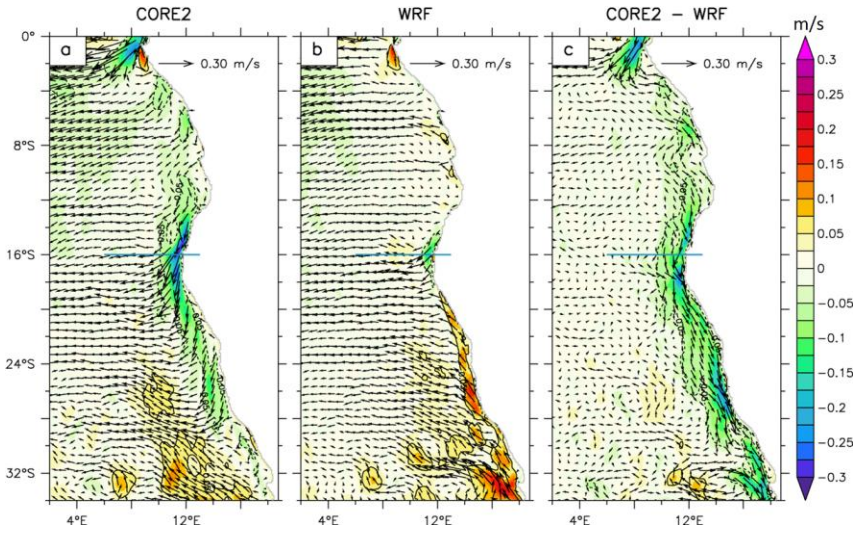

Fig.3.12 Meridional velocity (v, m/s, color shading) and surface currents (vectors) from the 9km_CORE2 run (left) and the 9km_WRF27 run (middle) experiments and their difference (right). Mean data for the period 2006-2009 and upper 15 m depth is shown here. In the 9km_CORE2 run, there is anomalous southward coastal current to the south of ABF zone (marked by blue line). In the 9km_WRF27 run, there is a strong near coastal Benguela current flowing north up to the latitude of ABF, which is in good agreement with observations and reanalysis datasets.

3.5 Impact of BLLCJ Strength and Spatial Structure

As shown above, the 9km_WRF27 run is able to significantly reduce SST bias in the SETA region by simulating a much more realistic upwelling and coastal currents compared to that in the 9km_CORE2 run. In this section, we will dissect how the BLLCJ strength and spatial structure affect the bias and circulation in the simulations, so that we will gain a better understanding of the underlying dynamics causing the SST bias.

3.5.1 Importance of Sverdrup Dynamics

As argued in previous sections, coastal winds are critical to maintain a realistic SST in SETA region. One important dynamical process relating to the coastal winds is argued to be the WSC of BLLCJ, which significantly influences the coastal SST via altering coastal currents and upwelling (Hurlburt and Thompson 1973; McCreary and Chao 1985; McCreary et al. 1987; Fennel et al. 2012; Junker 2014; Small et al. 2015). Thus, in order to understand the dynamics of the SST bias, in this section we mainly analyze the coastal structure of WSC and the WSC-driven Sverdrup flow along the Benguela coast.

The Sverdrup balance is governed by the following equation:

$$\beta\rho_0 \int_{-H}^{0} v_s dz = \nabla \times \boldsymbol{\tau} \cdot \boldsymbol{k}, \quad (3)$$

where β denotes the meridional gradient of the Coriolis parameter, ρ_0 the reference density of ocean water, v_s the meridional velocity of the current, $\boldsymbol{\tau}$ the wind stress vector, $\boldsymbol{k}$ the unit vector in verdical direction and H the layer thickness from ocean surface to the depth where vertical velocity equals 0, in order to avoid abyssal currents (Marchesiello et al. 2003; Wunsch 2011). In order to stress on the influence of Sverdrup

transport to surface SST, and to made the results comparable to earlier studies (e.g. Small et al. 2015), this study chooses H=500 m as the layer thickness to calculate the meridional transport. The Sverdrup balance will hold after the adjustment by long Rossby waves excited along eastern ocean boundaries is completed. In the vicinity of the eastern boundary, the adjustment proceeds very quickly so that the Sverdrup balance practically holds as an equilibrium ocean response to the winds.

The Sverdrup balance predicts a poleward transport under a negative WSC in the southern hemisphere. However, the balance will hold under the following assumptions: 1) the flow is in geostrophic balance, i.e., the Coriolis force balances the horizontal pressure gradient; 2) there is a level of no motion at certain depth below surface where both horizontal flows and pressure gradient vanish; and 3) frictional and non-linear processes can be ignored (Sverdrup 1947). In reality, lateral and bottom frictions are expected to be strong within the inner coastal region and nonlinear processes are likely to be active along the upwelling front and near the ABF. Therefore, the third assumption that frictional and non-linear processes can be ignored may not hold in the inner coastal region. As shown in Patricola and Chang (2017), the BLLCJ has two maxima that are trapped very close to the coast, producing a narrow coastal WSC structure. In the case that the off-shore length scale of the strong WSC is comparable to the width of the inner coastal regime where frictional and nonlinear processes cannot be ignored, the Sverdrup dynamics may not be applicable to the coastal circulation. On the other hand, if the scale of WSC is broader than that of inner coastal regime, such as the case in coarse-resolution climate model simulations where the BLLCJ is not explicitly resolved and its double-

core structure is not well represented with the simulated wind structure being located further off-shore (Small et al. 2015), then a Sverdrup flow can develop further off-shore, outside of the inner coastal regime. This will cause a strengthening in poleward transport along the coast, leading to a southward overshoot of the Angola Current at the ABF, carrying warm tropical water into the Benguela upwelling region and contributing to the warm SST bias.

As discussed by Junker (2014) using an analytical model, the applicability of the Sverdrup dynamics to coastal circulations depends on the zonal scale (L) of the longshore winds. It is shown that a critical length scale is at L ~ 300 km, above which the poleward Sverdrup flow driven by a negative WSC associated with the BLLCJ will dominate the coastal circulation. Such a theoretical result has been further confirmed by Small et al. (2015) in a set of numerical experiments. In this study, we estimate the scale of the inner coastal region where frictional and nonlinear processes are important and the Sverdrup balance breaks down by examining the linear momentum balance. The linear momentum equations that omit all the nonlinear and frictional processes can be written as:

$$-\rho f v = -\frac{\partial p}{\partial x} + \frac{\partial \tau^x}{\partial z}, \quad (4)$$

$$\rho f u = -\frac{\partial p}{\partial y} + \frac{\partial \tau^y}{\partial z}, \quad (5)$$

from which the Sverdrup solution is derived. By integrating (4) and (5) vertically over an upper ocean layer (H=500 m), the momentum balance becomes:

$$-f \int_{-H}^{0} \rho v dz + \int_{-H}^{0} \frac{\partial p}{\partial x} dz - \tau^x|_{-H}^{0} = 0, \quad (6)$$

$$f\int_{-H}^{0}\rho u\,dz+\int_{-H}^{0}\frac{\partial p}{\partial y}dz-\tau^{y}|_{-H}^{0}=0. \quad (7)$$

In reality, the linear balance is unlikely to hold, and thus the right-hand-side of (6) and (7) will not be exactly zero but given by a residual term R that can be used to measure the importance of nonlinear and frictional processes. (6) can then be cast into:

$$|\mathrm{R}_x|=\left|-f\int_{-H}^{0}\rho v dz+\int_{-H}^{0}\frac{\partial p}{\partial x}dz-\tau^{x}\right|, \quad (8)$$

where the magnitude of the residual term, ($|R_x|$), which includes all the frictional and nonlinear processes, can be used to evaluates the validity of the Sverdrup balance. It may be interpreted that when $|\mathrm{R}_x|$ is high, the influence of nonlinear and frictional processes is strong and the Sverdrup balance is likely to breakdown. However, ocean depth varies considerably from the coast to open ocean. Many areas of the coastal region have depth less than 500 m, making depth integrated residual term, $|\mathrm{R}_x|$, difficult to apply. A remedy to this difficulty is to use a vertically averaged residual term, ($\frac{|\mathrm{R}_x|}{H}$), to estimate areas where Sverdrup balance breaks down. The results are discussed in the following subsection.

3.5.2 Validity of Sverdrup Balance

As shown in Fig.3.2.13, the meridional component of coastal wind stress is stronger in the high-resolution WRF27 forcing (Fig.3.13b) than in the low-resolution CORE2 forcing (Fig.3.13a). The largest difference between WRF27 and CORE2 winds occurs near 16^{o}S where the ABF resides and 26^{o}S where Lüderitz Upwelling Cell resides

(Fig.3.13c). These large differences reflect the fact that the CORE2 winds do not resolve the double-core structure in the BLLCJ (Patricola and Chang 2017).

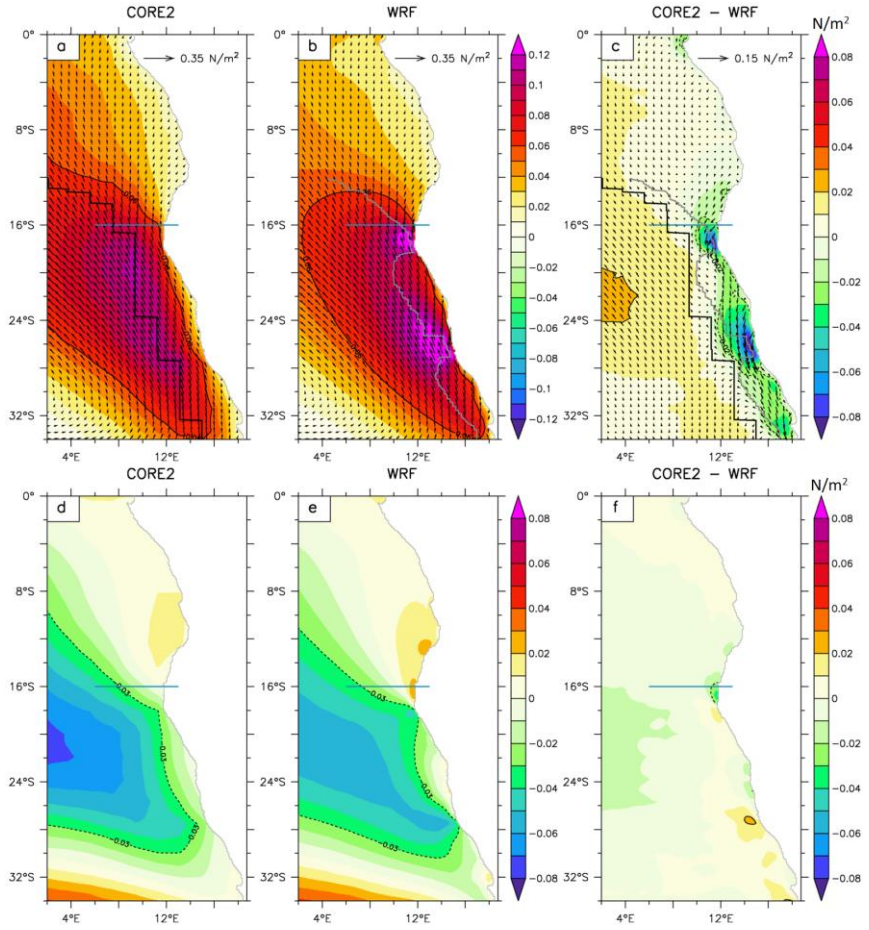

Fig.3.13 Meridional (upper panels) and zonal (lower panels) wind stress (N/m^2) from CORE2 and WRF27 and their differences on the 9-km ROMS grid. Arrows in upper panels (data for every 8th grid point is shown here) show wind direction (a and b) and direction difference (c). In all panels selected contours are used to highlight regions of interest. The location of BCLLJ core from CORE2 is shown using a black line (a) and (c) and from WRF27 is shown using a thick grey line in (b) and (c).

Additionally, the position of maximum wind stress is much closer to the coastline in the high-resolution WRF27 forcing than in the low-resolution CORE2 forcing, especially near the double-core region. Such stronger and closer-to-coast wind stresses in the WRF27 forcing creates a strong zonal wind stress shear near the coast, which in turn results in a stronger and narrower WSC (Fig.3.15e). In contrast, the CORE2 forcing produces a weaker and broader coastal WSC in the region (Fig.3.15a).

According to the previous discussion, the value of $\frac{|R_x|}{H}$ can be used to evaluate the validity of the Sverdrup balance. We computed $\frac{|R_x|}{H}$ at every grid and compare them between 9km_CORE2 and 9km_WRF27 runs in Fig.3.14, in order to identify regions where nonlinear and frictional processes are important. Fig.3.14 shows that $\frac{|R_x|}{H}$ in both experiments shares very similar spatial structures: First, the area of high $\frac{|R_x|}{H}$ values are mainly confined within in an inner coastal zone along the coast, suggesting that nonlinear and frictional processes within this zone can cause Sverdrup balance to breakdown. Second, there is a considerable variation in the width of the inner coastal zone along the coast from the equator to the southern tip of the West African Coast. The width of the inner coastal zone is extremely narrow north of Cape Frio (18^oS), with an offshore scale of about 0.5^o, while on the southern side of Cape Frio there is a linear increase of the width as latitude increases. The maximum width is about 2^o ($L \approx 200$ km). We note that the above momentum balance analysis only give a necessary but not sufficient condition for the Sverdrup balance to hold, because the Sverdrup balance

can only be achieved after the long Rossby wave adjustment. The wave adjustment process is not taken into the consideration by the momentum balance analysis.

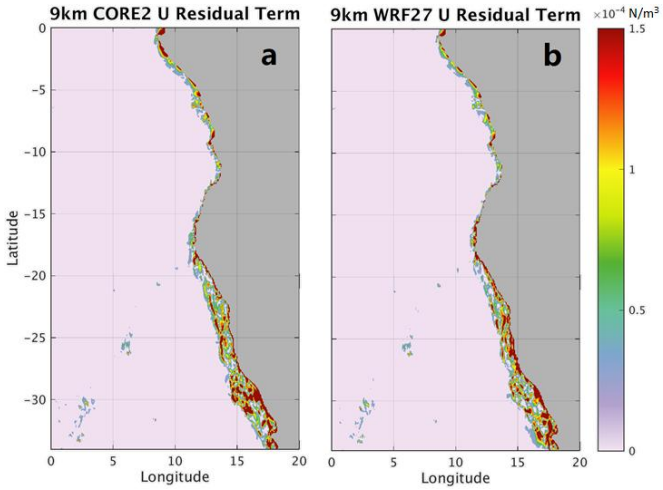

Fig.3.14 Absolute value of the residual term from the u-momentum equation, averaged over the upper 500 m ($\frac{|R_x|}{H}$, N/m^2). a, the 9km_CORE2 run. b, the 9km_WRF27 run.

In order to verify the validity of the Sverdrup balance (3) in the model simulations, the WSCs, i.e., $\nabla \times \boldsymbol{\tau}$, from CORE2 forcing (Fig.3.15a) and WRF27 forcing (Fig.3.15e) are compared with the vertical integrated meridional ocean velocity (multiplied with $\beta\rho_0$), i.e., $V = \beta\rho_0 \int_{-H}^{0} v_s dz$, from 9km_CORE2 and 9km_WRF27 runs (Fig.3.15b and f), respectively: In both CORE2 and WRF27 winds, the WSC is strong along the southeastern coast from 12^{o}S to 34^{o}S, however, the offshore scale of the winds is about 3-4^o in CORE2 (Fig.3.15a) but only around 2^o in WRF27 (Fig.3.15e), suggesting the Sverdrup balance holds up better in the 9km_CORE2 run than in the 9km_WRF27 run. This is confirmed by comparing WSC and V: In the 9km_CORE2 run WSC and V have similar amplitude and offshore structure along the coast with a scale as broad as 3^o

(Fig.3.15a and b). Accordingly, one can conclude that the Sverdrup transport dominates the poleward vertically integrated v-velocity (V) from 12^{o}S to 34^{o}S in the 9km_CORE2 run (Fig.3.15a and b). In contrast, WSC and V do not agree well in the 9km_WRF27 run: While WSC shows strong negative value in the inner coastal region everywhere south of 12^{o}S, V shows only strong negative value near the ABF, suggesting that the Sverdrup balance holds only over that region. South of the ABF, V is slightly negative within an offshore stripe, but retains positive values within the inner coastal region, suggesting that V in the 9km_WRF27 run is not governed by Sverdrup dynamics. These results are consistent with the previously argument and theoretical studies: In the 9km_CORE2 run, the offshore scale of WSC (3^{o}-4^{o}) is wider than the width of the inner coastal region (1^{o}-2^{o}) where nonlinear and frictional processes dominate, which allows the Sverdrup balance to hold (Fig.2.15a and b). On the other hand, in the 9km_WRF27 run, the WSC scale is comparable to that of the inner coastal region (1^{o}-2^{o}). Therefore, even though the WSC in the 9km_WRF27 run is stronger than that in the 9km_CORE2 run, it mostly occurs within the inner coastal region where nonlinear and frictional processes are strong, causing the breakdown of the Sverdrup balance (Fig.3.15f). Based on these analyses, we conclude that the validity of the Sverdrup balance in a model can strongly dictates the nature of the poleward transport along the coast that strongly influences the near surface circulation and the location of the ABF, which in turn further impacts the SST bias.

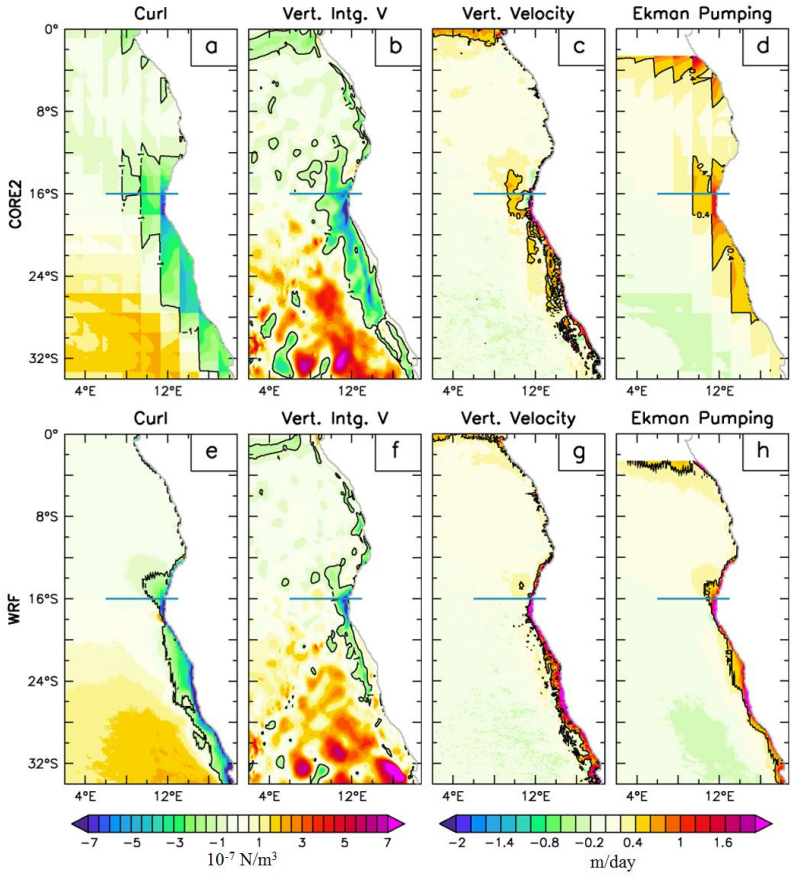

Fig.3.15 Wind stress curl (10^{-7} N/m^3, panels a, e), vertically integrated (0-500 m) meridional velocity (v) multiplied by $\beta\rho_0$ (β=meridional gradient of Coriolis force, ρ_0 is a reference ocean density) (10^{-7} N/m^3, panels b & f), vertical velocity at 40 m depth (m/day, panels c & g) and Ekman Pumping velocity (m/day, panels d & h) from the 9km_CORE2 run (upper panels) and the 9km_WRF27 run (lower panels) experiments. Please note that the first colorbar is common for columns 1-2 and the second colorbar is common for columns 3-4.

As noted previously, the Sverdrup flow is barotropic that influences the flow within the entire water column. Thus, further analysis is done here to test how the validity of the Sverdrup balance can influence surface response. Fig.3.16 compares the vertical structure of meridional velocity averaged over a 1^o-wide stripe following the coastline among CFSR, 9km_CORE2 and 9km_WRF27 runs. As shown in the coastal cross

section of meridional ocean velocity in CFSR reanalysis (Fig.3.16a), a poleward undercurrent (PUC) resides the subsurface layer from 20 m to 200 m deep, transporting from the equatorial region to the ABF region. Whereas a strengthening of PUC can be observed in both 9km_CORE2 (Fig.3.16b) and 9km_WRF27 (Fig.3.16c) runs, which is due to Sverdrup balance. Since the validity of Sverdrup balance in the 9km_CORE2 run is much higher than in the 9km_WRF27 run, the resulted strengthening of PUC is also much larger in the 9km_CORE2 run (Fig.3.16d) than in the 9km_WRF27 run (Fig.3.16e). Accordingly, the PUC in the 9km_CORE2 run is spatially expanded, which leads to the emerging of PUC and transports the warm surface water to the cold surface Benguela region. In contrast, the PUC in the 9km_WRF27 run is only slightly increased that the influence is not strong enough to reach the surface, and hence the Angola Current does not overshoot into the Benguela region to cause such strong SST bias as the 9km_CORE2 run. This result confirms the argument of Fennel et al. (2012), which used a linear theoretical model and revealed that a seaward shift of maximum wind (therefore the WSC is broadened) can cause the PUC to reaching the surface. Therefore, conclusion can be made that the spatial scale of coastal WSC is of first order importance to the SST bias.

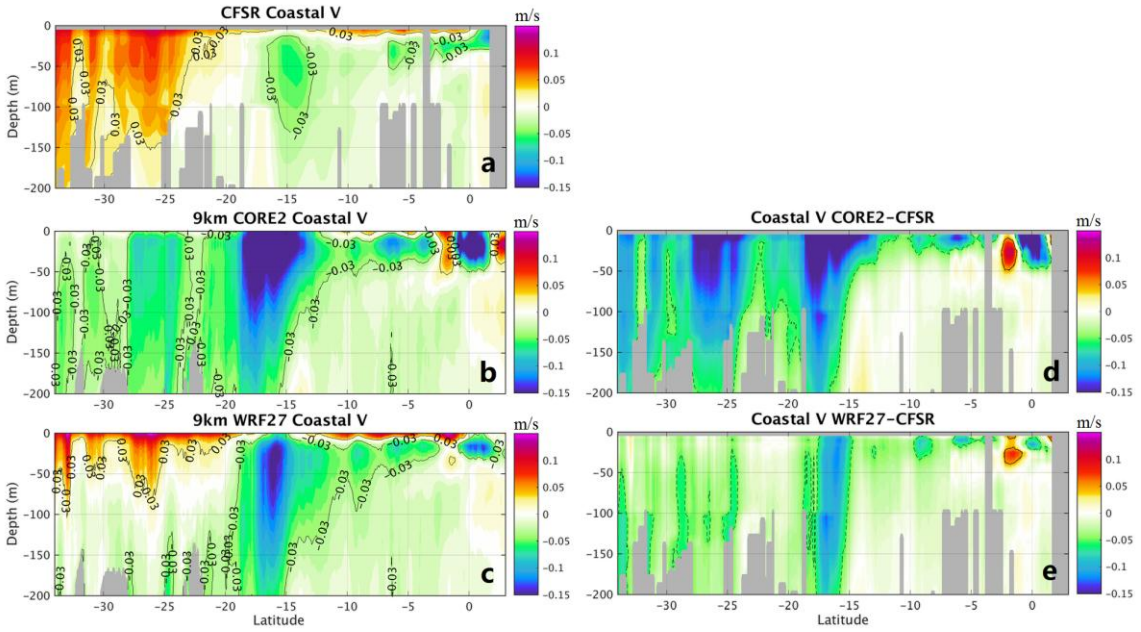

Fig.3.16 Meridional velocity and difference cross sections (m/s) along the coastal 1^{o} wide band (a-e). a-c, Meridional velocity of the CFSR reanalysis data (Saha et al., 2010), the 9km_CORE2 run and the 9km_WRF27 run respectively. d-e, Difference of meridional velocity for 9km_CORE2 and 9km_WRF27 runs respectively, with respect to CFSR data. Mean data for years 2006-2009 is shown here. Grey shading mainly indicates topography and missing data in CFSR data. Selected values are marked in black contour.

3.5.3 Role of Ekman Dynamics

Theory of Sverdrup Balance sheds light on the cause of the overly exaggerated Angola Current and its contribution to the warm SST bias induced by overshooting of warm water southward across the ABF. However, other processes may also contribute greatly to the formation of SST bias.

Within the top 100 m of the ocean, Ekman transport (Ekman 1905) resulted from the balance between Coriolis force and wind stresses dominates the water transport processes, moving the water to the left (right) of wind forceing direction in the southern

(northern) hemisphere. As such, in the SETA region, the BLLCJ will induce an offshore Ekman transport at the surface and create a divergence zone along the West Africa coast. Such a surface divergence will cause water from underneath to move upward, resulting an upwelling along the Benguela coast. As a part of this upwelling circulation, sea level increases in the off-shore direction, resulting a negative zonal pressure gradient that will drive an equatorward geostrophic flow along the coast. The northward Benguela Current along the Benguela upwelling zone is largely explained as an Ekman upwelling driven current. Thus, an evaluation of Ekman transport in the ROMS experiments is important in understanding the mechanisms of coastal circulation and formation of SST bias.

Fig.3.17 shows the Ekman transport computed using the wind stress in 9km_CORE2 and 9km_WRF27 runs and their difference. The the 9km_CORE2 run has very weak off-shore water transport everywhere within the inner coastal region due to the weak near coastal wind stress (Fig.3.13a). The maximum transport occurs near the northern BLLCJ core (16^oS) with magnitude of ~1.0 m^2/s, and near the southern core (26^oS) with magnitude of ~0.5 m^2/s. In contrast, the 9km_WRF27 run has much stronger off-shore water transport in the inner coastal region with maximum amplitude of ~2.0 m^2/s near the northern core and of ~1.5 m^2/s near the southern core. The difference of the Ekman transport between the two experiments as in Fig.3.17c clearly indicates that the off-shore Ekman transport is uniformly weaker in the 9km_CORE2 run than in the 9km_WRF27 run within a coastal zone extending from 10^oS all the way to 34^oS. The difference is especially large in the BLLCJ double-core regions. Consequently, the upwelling and the associated geostrophic equatorward flow induced by Ekman

divergence are both considerably weaker in the 9km_CORE2 run than in the 9km_WRF27 run, which is consistent with the coastal upwelling strength shown in Fig.3.2.15c and g, and the meridional velocity in Fig.3.12 and Fig.3.16.

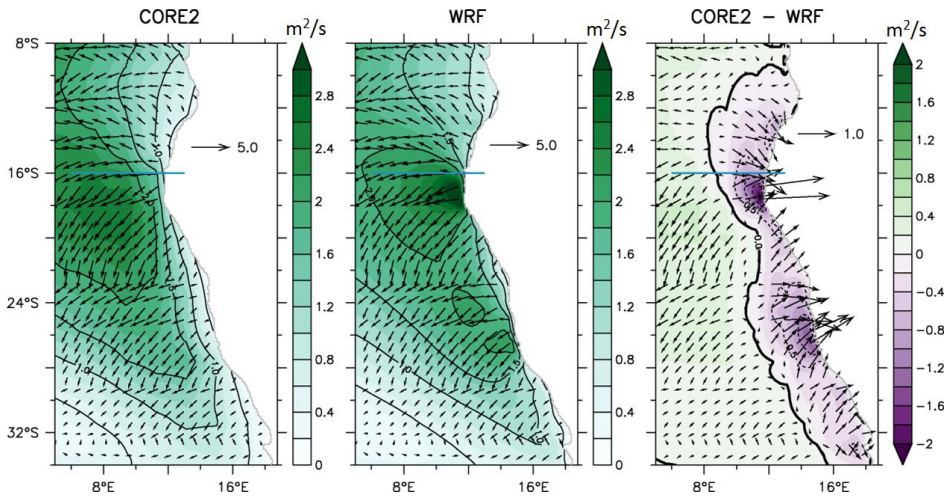

Fig.3.17 Total Ekman transport (m^2/s) computed from CORE2 (left) and WRF27 (middle) mean wind stress and their difference (right). Shading and contour shows the Ekman transport while arrows show the direction of transport. Data for 2005-2009 has been used and the zonal and meridional wind stress components were rotated to across and alongshore directions using coastline angle with respect to true north. The difference plot highlights the weak Ekman transport in the 9km_CORE2 run from very weak winds close to the coast line.

The weaker equatorward Benguela Current in the 9km_CORE2 run is also likely to contribute to the southward overshoot of the ABF, as it marks the convergence of the Angola Current and Benguela and should be maintained by both these currents. It is also interesting to note that the northern and southern core of the BLLCJ correspond to the location of the ABF and Lüderitz Upwelling Cell, both of which are marked by strong

offshore near-surface transport, indicating the importance of fine structure of the coast winds in maintaining the coastal circulation.

Another relevant process to SST bias is Ekman pumping, which is directly influenced by the strength of WSC. The Ekman pumping induced vertical velocity (w_E) can be calculated as such (Smith 1968):

$$w_E = \frac{\nabla \times \tau}{\rho f}. \quad (9)$$

The WSC induced Ekman pumping can be as important as the upwelling caused by off-shore Ekman transport (Rodrigues and Lorenzzetti 2001). While the off-shore Ekman transport induced upwelling is highly confined to the coastline, WSC can arouse upwelling within several hundred kilometers off-shore (Junker 2014). To assess the importance of Ekman pumping, we compare the model simulated vertical velocity at 40 m deep (Fig.3.15c and g) with the Ekman pumping velocity (Fig.3.15d and h). In the 9km_CORE2 run, the WSC induced Ekman pumping covers an approximately 2^o wide band along the coast from 12^oS to 28^oS (Fig.3.15d). The model output vertical velocity has a similar wide band between 12^oS and 28^oS, but has a stronger magnitude along the inner coastal region, which is contributed by the off-shore Ekman transport. In the 9km_WRF27 run, while the model output upwelling has very good correlation with Ekman pumping in general structure, the magnitude is stronger than Ekman pumping, which also proves the contribution of off-shore Ekman transport.

To conclude, in the 9km_CORE2 run, a weak Ekman transport induced Benguela Current and a strong Sverdrup Balance induced Angola Current both contributes to the overshoot of warm water and causes the SST bias. On the other hand, both Ekman

transport induced coastal upwelling and Ekman pumping are weak in the Benguela region, therefore less cold water is upwelled to the surface to reduce SST, which acts to strengthen the warm SST bias.

3.6 Double-time Averaged Heat Budget

As introduced in Section 3.2, DTA method is used to dissect the contribution of each heat budget term. Here, we use this method to determine which oceanic process contributes dominantly to the temperature difference between 9km_CORE2 and 9km_WRF27 runs. To validate the DTA analysis, we first compare the climatological mean temperature difference between 9km_CORE2 and 9km_WRF27 runs (Fig.3.18a) to the difference of DTA-derived temperature difference between the two experiments (Fig.3.18b). Evidently, the two temperature fields are nearly identical, suggesting that the DTA analysis is a valid approach. The temperature difference between the two experiments resembles the warm SST bias in the 9km_CORE2 run (Fig.3.2c) with only a small difference of 1-2^{o}C north of ABF (16^{o}S) and much larger and broader temperature difference (1-4^{o}C) in the Benguela region (28^{o}S-16^{o}S). This is expected because the 9km_WRF27 run has much weaker SST biases than the 9km_CORE2 run. For simplicity, in the following we refer to the temperature difference between the two model simulations as SST bias.

Next, we examine how each process in the temperature equation contributes to the SST bias shown in Fig.3.18b. Fig.3.18c shows the contribution of total advection of heat, including both the horizontal and vertical heat advection, to the SST bias. It is evident

that the advection of heat contributes positively to the bias in Fig.3.18b. In fact, the advection-induced temperature difference shown in Fig.3.18c is one order magnitude larger than the SST bias shown in Fig.3.18b, suggesting the warm SST bias along the coast in the 9km_CORE2 run is primarily caused by the different advective processes between 9km_CORE2 and 9km_WRF27 runs.

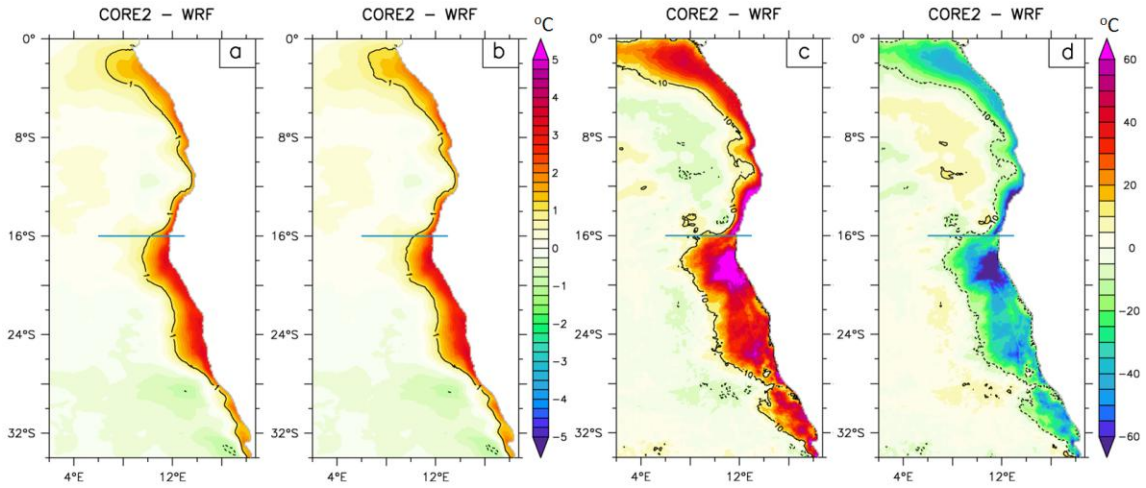

Fig.3.18 True temperature difference (^{o}C) between 9km_CORE2 and 9km_WRF27 runs is shown in panel (a). Difference of double time averaged (DTA) temperature tendency (dT/dt; ^{o}C) between 9km_CORE2 and 9km_WRF27 runs is shown in panel (b). Difference of total advection (c) and total diffusion (d) are shown in other panels. All data shown here is averaged for upper 20 m depth and have units of ^{o}C.

Fig.3.18d shows the contribution from diffusive processes in the temperature equation, which include both the surface heat fluxes and vertical and horizontal diffusive processes in the ocean. Note that the diffusion-induced temperature difference is negative everywhere and its amplitude is comparable to, but smaller than, the advection-induced temperature difference, so that the net contribution from both processes gives

rise to the warm SST bias shown in Fig.3.18b. This suggests that the difference in the advective processes between the two experiments dominates the SST bias by creating the warm SST bias in the first place. The diffusive process then works to counteract with advective processes by removing the warm SST bias through surface heat flux damping and vertical and horizontal mixing.

The above analysis has shown that the advective processes have a positive contribution on the warm SST bias, while diffusion works against it. This leads to the question whether it is the horizontal or the vertical advection that has the most significant contribution. Therefore we further decomposed the total advection into a horizontal component and a vertical component, which are shown in Fig.3.19. In the inner-coastal region (within a 2^o band along the coast) advection difference between the two experiments shows large positive values (>700^{o}C) in horizontal direction and negative values (~-700^{o}C) in vertical direction. In the off-shore region, horizontal advection difference shows negative values (~-300^{o}C) and vertical advection difference shows positive values (~300^{o}C). This suggests that it is mainly the horizontal advection that increases the warm SST bias in the inner-coastal region, and the vertical advection has a positive contribution to the warm SST bias in the off-shore region. Thus, it can be concluded that both horizontal advection and vertical advection are important contributors to the warm SST bias, and can compensate with each other. Therefore, it is more reasonable to consider these two processes as a whole, rather than separating them.

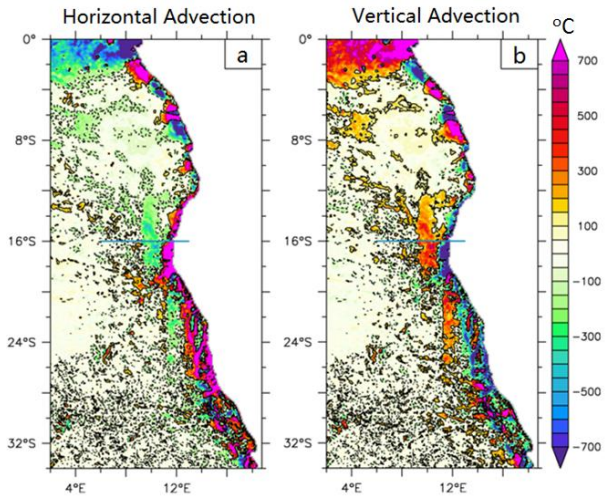

Fig.3.19 Difference of double time averaged (DTA) horizontal advection (a) vertical advection (b). Contours show -100 and 100 ^{o}C values. As Fig.3.18, data shown is average for 20m depth and for the 2005-2009 period.

3.7 Discussion

Several aspects require further discussions. To begin, comparison between the 9km_CORE2 run and the 9km_WRF09 run indicates that the largest differences in SST and wind forcing emerge at the position of the BLLCJ double-core. It therefore raises the question about the relationship between the coastal circulation and the double-core structure of the BLLCJ. In particular, to what extent does the northern core of the BLLCJ determine the location of the ABF? To shed light on these questions, a sensitivity run using the WRF27 forcing with artificially removed northern core near the ABF region is conducted and compared with the 9km_WRF27 run (Fig.3.20). The meridional wind stress is artificially removed near the ABF, so that the strong WSC near the coast caused by the rapidly decreasing winds is essentially removed. Outside the ABF region, the winds and WSC are intact, which allows us to examine the effect of

removing the northern core of the BLLCJ on the ABF. Forced by such winds, an increase of SST by >1^{o}C occurs in the coastal ABF region, suggesting that the northern core structure does play a critical role in the formation of the ABF. Without the northern core, the ABF weakens, causing a warm SST bias to form. However, the SST increase in the absence of the northern core is not as large as the SST difference between 9km_WRF27 and 9km_CORE2. Future studies are needed to further understand the influence of the northern core on the ABF. Moreover, since the circulation system in the southern core region is dominated by the Lüderitz Upwelling Cell which is different from that in the northern core region, it is worth exploring how the southern core can contribute to the Lüderitz Upwelling Cell and related SST distribution in the region.

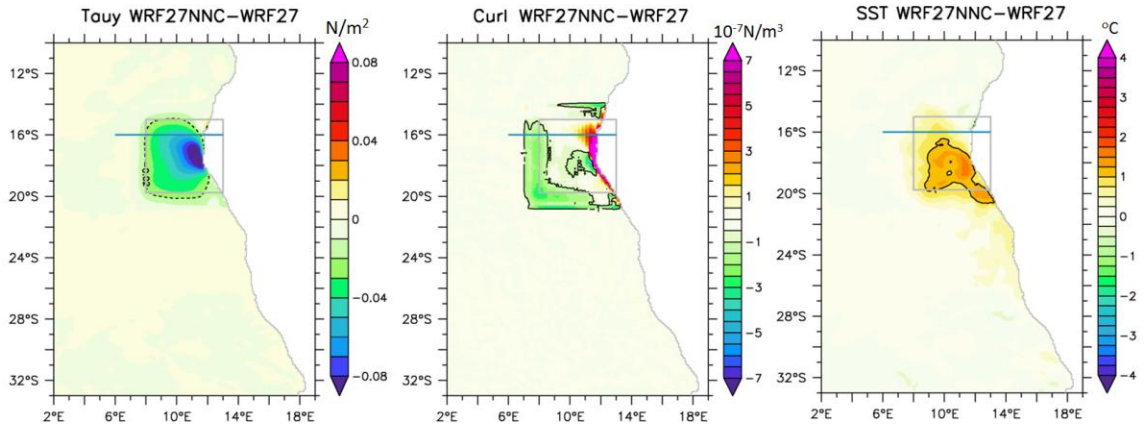

Fig.3.20 Difference between the 9km_WRF27NNC run with no northern core of the BLLCJ and the 9km_WRF27 run with original wind field in meridional wind stress (N/m^2, left), wind stress curl (10^{-7} N/m^3) and SST (^{o}C). This experiment has run only for one annual cycle (2005).

The CORE2 forcing and WRF forcing are not only different in winds but also in heat fluxes. To further separate the influence of the winds from that of the heat fluxes,

two more sensitivity runs are carried out using CORE2 and 9 km WRF forcing with their winds exchanged but keeping the original heat fluxes (see details in Section 2.2.3 and Table 1). As Fig.3.21 shows, the SST difference between the 9km_WRF09CW run and the 9km_WRF09 run is significantly larger than that between the 9km_CORE2WW run and the 9km_WRF09 run. This suggests that the SST bias is mainly contributed by the wind forcing.

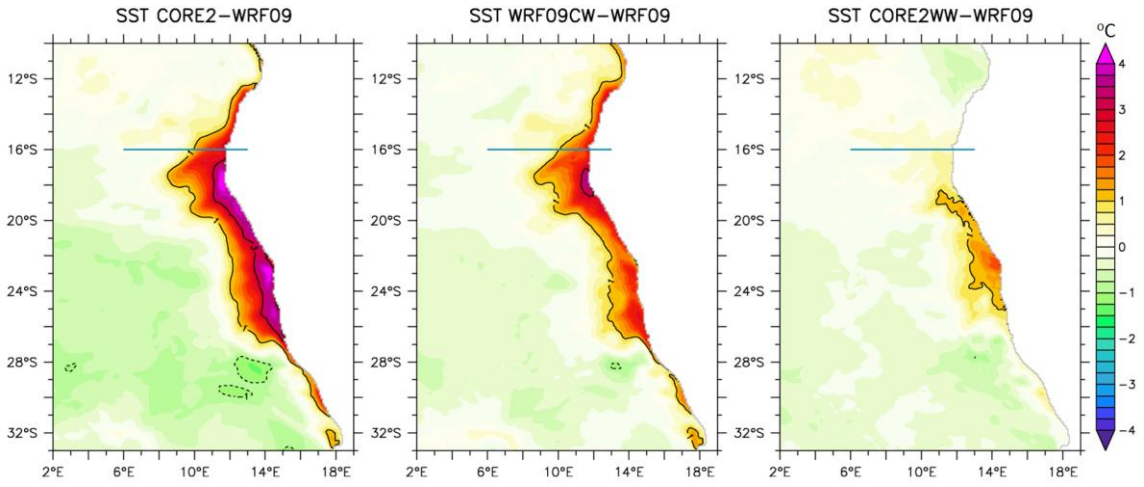

Fig.3.21 SST difference with respect to the 9km_WRF09 run from the 9km_CORE2 run (left), WRF09CW case with WRF09 heat flux and CORE2 winds (middle) and CORE2WW case with CORE2 heat flux and WRF09 winds (right). This comparison further illustrates that the first order of importance for the SST biases observed in the 9km_CORE2 run is the deficiencies in the CORE2 winds.

Furthermore, as suggested by the heat budget analysis, it is mainly the horizontal advection that contributes to the warm SST bias. This horizontal advection can be further decomposed into eddy and mean flow components. The contribution from eddy-induced advection has not been studied in the SETA region before, to the best of our

knowledge. In order to assess the potential importance of eddy-induced advection in the SST bias in the SETA region, the next chapter will mainly focus on separating the eddy and mean flow contribution to the local heat budget, and quantifying their influences on the warm SST bias.

3.8 Summary

This chapter used suites of high resolution ROMS simulations, including varying ocean model resolutions and changing atmospheric forcing from coarse resolution CORE2 forcing to high resolution forcing derived from 27 km WRF simulations forced by observed SST and reanalysis at the lateral boundaries. In general, the WRF27-forced runs have successfully reduced the area and magnitude of the warm SST bias in the SETA region. The fine structure of the BLLCJ in the inner coastal region plays the most important role in affecting the warm SST bias. When the core of the BLLCJ is located further off-shore (such as in CORE2), a weak and broad WSC emerges and causes the Sverdrup balance to hold, which in turn causes an overshoot of the Angola Current that transports warm tropical water into the cold upwelling region and forms the SST bias. When the core of the BLLCJ is located near the coast (such as in WRF27), the strong and narrow WSC will cause the Sverdrup balance to break down near the coast, thereby preventing the Angola Current from overshooting across the ABF, resulting in a much reduced warm SST bias. Under realistic wind forcing, the increase of ocean model resolution does result in some relief of the SST bias problem. In particular, when the ocean model resolution increases from eddy permitting (27 km) to eddy resolving, the

warm SST bias in the Lüderitz Upwelling Cell region is reduced (Fig.3.2), suggesting a possible role of ocean eddies in reducing the SST bias. However, the overall effect of ocean model resolution appears to be of secondary importance. Furthermore, the heat budget analysis reveals that in the inner coastal region, advection is the main contributor to the warm SST bias, while diffusion mainly works against advection and buffer the formation of the SST bias. Further examination is required to find out whether it is the mean flow or eddies that contribute to the warm SST bias in the SETA region.

CHAPTER IV

ROLE OF OCEAN EDDIES IN BENGUELA SST BIAS

4.1 Introduction

As introduced in Chapter 1, Hypothesis II was based on previous eddy heat transport (EHT) studies in other EBUSs, which gives us a testable prediction about the contribution of eddies to the warm SST bias in the SETA region. Robust eddy activity in the SETA region has been reported in previous studies, but, to the best of our knowledge, its potential effect on SST has not been fully evaluated. This motivates us to seek a general understanding about the role of ocean eddies in the local heat budget along the Benguela upwelling region.

Previous studies documented that strong eddy activity emerges in the vicinity of the ABF and Benguela upwelling regions (Shannon et al. 1987; Rae et al. 1996; Rubio et al. 2009; Bettencourt et al. 2012). Observations and numerical models revealed some general eddy characteristics in these regions. The overall heat, salt, and volume transport by eddies are estimated at 2.2~3.3x10^{20} J/yr, 14~21x10^{12} kg/yr, and 2.6~3.8x10^{6} m^3/s, respectively (Rae et al. 1996), suggesting that these off-shore moving eddies can be a significant player in the exchange between the coastal and the open ocean (Rubio et al. 2009). Both warm-core and cold-core eddies are found to be active near the ABF, generally forming within the region between 11°S-16°S and 5°E-11°E, and found to emerge almost exclusively in austral summer (Stander 1964; Filippov and Kolesnikov 1971). Since eddies are most prominent near the ABF and Lüderitz Upwelling Cell

regions, i.e. the same locations as the BLLCJ double-core, it is reasoned that the coastal eddies in these two regions are induced by instabilities of the strong ABF and upwelling front, which are ultimately caused by the local surface wind forcing. Therefore, it is conceivable that the activity and distribution of the coastal eddies are sensitive to the structure of the BLLCJ.

In Chapter 3, the total advection was shown to be the major contributor to the warm SST bias in the SETA region. However, the advection heat budget term consists of both mean flow and eddy induced components. To what extent the eddy induced component contributes to the local heat budget has not been quantified. As the simulation of eddies high model resolution, we use in this chapter the pair of 3 km ROMS experiments with daily output to conduct our analyses. Comparisons between the low-resolution CORE2 forced and high-resolution WRF27 forced runs allow us to reveal the sensitivity of simulated ocean eddies to wind forcing.

This chapter is organized as follows. The data analysis strategies are introduced in Section 4.2. The annual mean and seasonal mean climatology of eddy statistics are discussed in Section 4.3. Section 4.4 uses the DTA method to quantify the contribution of eddy and mean flow to the warm SST bias in the SETA region. Finally, Section 4.5 gives a discussion and conclusion of this chapter.

4.2 Data Analysis Strategy

As introduced in Chapter 2, ROMS sensitivity experiments with 3 km horizontal resolution and daily model output are carried to assess the role of ocean eddies in the

warm SST bias. At 3 km resolution, the model is capable of resolving ocean mesoscale eddies and permitting submesoscale eddies, which in turn allows an assessment of the role of ocean eddies in the local heat budget. This chapter is devoted to the analysis of the contribution of ocean eddies to the heat budget. The data analysis strategy will be discussed below.

4.2.1 Model Validation

Before proceeding to analyze the heat budget, model eddy fields are validated against observed datasets. Since observing eddies in the ocean requires high spatial and temporal measurements that are lacking, it is expected that eddies calculated directly from the model simulations may be different from the existing observations because the model resolution at 3 km is substantially higher than the resolution of the global observations. To minimize the resolution mismatch, we spatially smoothed and temporally re-sampled the 3 km daily model outputs to derive a $1/4^{o}$ weekly dataset that is consistent with the $1/4^{o}$ weekly AVISO SLA data. The variance of simulated SLAs is then computed and compared with AVISO SLA variance. This comparison gives an indication of the strength and distribution of geostrophic eddies in model experiments and observations. In addition, the vorticity of geostrophic eddies can be estimated by taking the Laplacian of SLAs, $\nabla^2 z$, where ∇^2 represents the 2-D Laplacian operator and z represents SLA. Enstrophy ($E = \frac{1}{2}(\nabla^2 z)^2$) that measures the vorticity variance of geostrophic eddies can then be calculated and compared. In addition, Reynolds satellite SST data is used to compare the observed SST variance with that of the simulations.

Since Reynolds SST is daily data with 1/4^{o} resolution, the 3 km resolution ocean model output has been smoothed to this resolution, while the daily sampling frequency has been maintained to keep consistency with the observation.

To further validate the SLA and SST variances of the experiments, the Hybrid Coordinate Ocean Model (HYCOM) ocean reanalysis has been employed. Since HYCOM data has 1/12^{o} horizontal resolution and provides 3-hourly output, to keep consistency between HYCOM data and the 3 km ROMS experiments, we first smoothed the model output to the 1/12^{o} resolution grid of HYCOM, and then averaged the HYCOM data every 8 time points to obtain daily data. This way, the HYCOM data and ROMS output were rendered comparable with each other.

4.2.2 Eddy Kinetic Energy and Eddy Heat Transport

Ocean fields (such as temperature and velocity) can be decomposed into a climatological component and a transient component:

$$T = \bar{T} + T', \quad (10)$$

where T is the total temperature field, $\bar{T}$ climatological temperature field and T' transient component. Various methods can be applied to define eddy fields. Among these methods, the time-mean method is most frequently used, which uses time average of a relevant field as climatological state and the difference between the mean and total field as eddies (Roemmich and Gilson 2001; Jayne and Marotzke 2002; Trani et al. 2011; Isachsen et al. 2012; Colas et al. 2013). In this chapter, we subtract the seasonal mean from the total fields, assuming that the departure from the seasonal mean represents eddies.

In each season, EKE can be estimated by:

$$EKE = \frac{1}{2}\overline{(\boldsymbol{V} - \overline{\boldsymbol{V}})^2}. \quad (11)$$

Similarly, the mean eddy heat transport is computed using the covariance of temperature and velocity (Jayne and Marotzke, 2002):

$$EHT = \overline{\boldsymbol{V}'T'} = \overline{\boldsymbol{V}T} - \overline{\boldsymbol{V}}\overline{T}. \quad (12)$$

In (11) and (12), $\boldsymbol{V}$ is ocean current velocity vector ($\boldsymbol{u} + \boldsymbol{v}$), the overbar represents the season mean and prime the deviation from the seasonal mean. Note that EHT is a vector, and its zonal and meridional components are computed as $\overline{\boldsymbol{u}'T'}$ and $\overline{\boldsymbol{v}'T'}$ respectively.

4.2.3 Eddy Contribution to Heat Budget

As introduced in Chapter 2, all heat budget terms can be computed using the DTA method, which provides a concise way to compare the difference between CORE2- and WRF27-forced run. Since this heat budget analysis covers the entire period of the respective 5-year simulations, the difference between the DTA heat budget terms allows us to eliminate the influence of initial condition, as discussed in Chapter 3. This way, we can examine the contribution of eddies and mean flow to the heat budget difference between the pair of experiments.

We will compute the divergence of eddy heat transport using the estimated eddy heat transports to quantify the contribution of eddies to the upper ocean heat budget. According to the temperature equation (Qiu and Kelly 1993):

$$\frac{\partial T}{\partial t} = -\left(\boldsymbol{u} \cdot \nabla T + w\frac{\partial T}{\partial z}\right) + A_h \nabla^2 T - \frac{\partial}{\partial z}\overline{w'T'} + \frac{1}{\rho_0 c}\frac{\partial q}{\partial z}, \quad (13)$$

where A_h is the horizontal diffusivity, c is the heat capacity of sea water and q is the downward radiative flux. On the left hand side of (13), $\frac{\partial T}{\partial t}$ is the temperature tendency. On the right hand side: $-\boldsymbol{u} \cdot \nabla T$ is the horizontal advection (Q_{hadv}), $-w\frac{\partial T}{\partial z}$ is the vertical advection (Q_{vadv}), and the summation of these two terms is total advection (Q_{adv}); $A_h \nabla^2 T$ is the horizontal diffusion (Q_{hdiff}), $-\frac{\partial}{\partial z}\overline{w'T'}$ is the vertical mixing, $\frac{1}{\rho_0 c}\frac{\partial q}{\partial z}$ is the net heat flux from radiation (Q_{net}) and the summation of these terms is total diffusion (Q_{diff}). In this chapter, we further decompose the total advection into mean flow advection (Q_{mean}), and eddy advection (Q_{eddy}):

$$Q_{adv} = Q_{mean} + Q_{eddy}. \quad (14)$$

This will allow us to estimate the magnitude of Q_{eddy} compared to other terms in the upper ocean heat budget, so that we can quantify the contribution of ocean eddies to the local heat budget. In order to quantify the contribution of eddies to the surface ocean, and to keep consistency with the heat budget analysis in Chapter 3, we will integrate the heat advection terms over the top 20 m, so that we can evaluate each term's contribution to the SST.

4.3 Eddy Statistics in the Southeast Tropical Atlantic Region

4.3.1 Model Validation

We compared the SLA variance of observed and simulated experiments (Fig.4.1a-c). The AVISO altimetry SLA data (Fig.4.1a) shows extremely small variance roughly to the north of 25°S and large variance to the south. South of 25°S, the region with high

variance is located around 3^{o} off-shore with the highest value near the southern boundary and decreasing strength towards north, which suggests that the energetic eddy activity originates from the Agulhas Leakage region and propagates into the SETA. Therefore, this high SLA variance is likely connected to the Agulhas Leakage, which sheds strong and deep-reaching geostrophic eddies (Agulhas Rings) into the SETA region and produces large SLA variability. On the other hand, both experiments (Fig.4.1b and c) show similar general spatial pattern to the observation, with weak SLA variance north of 25^{o}S and high variance to the south. However, the magnitude of SLA variance is substantially weaker in the simulations than that in the observation. High-variance regions in the model simulations are also about 3^{o} off-shore. The major difference between the observed and simulated fields is in the magnitude of SLA variance. In the observations, the SLA variance shows a high value of more than 150 cm^{2}, whereas the model simulations show a value of 100 cm^{2} only in a small area within the high variance region. This indicates that the eddy shedding process from the Agulhas Leakage is underrepresented in the model simulations, which may be caused by the use of the CFSR flow fields at the southern boundary. We note that the energetic eddy activity in the southernmost part of the SETA region is unlikely to have a major impact on the SST bias, because it is located offshore away from the strong SST bias region. Along the coast where the SST bias is the strongest, even though the SLA variance is much weaker, there is some indication of geostrophic eddy activity. Along the inner coastal region, relatively strong EKE can be observed in all datasets near ABF. Near the Lüderitz Upwelling Cell, relatively stronger EKE only occurs in the 3km_WRF27 run.

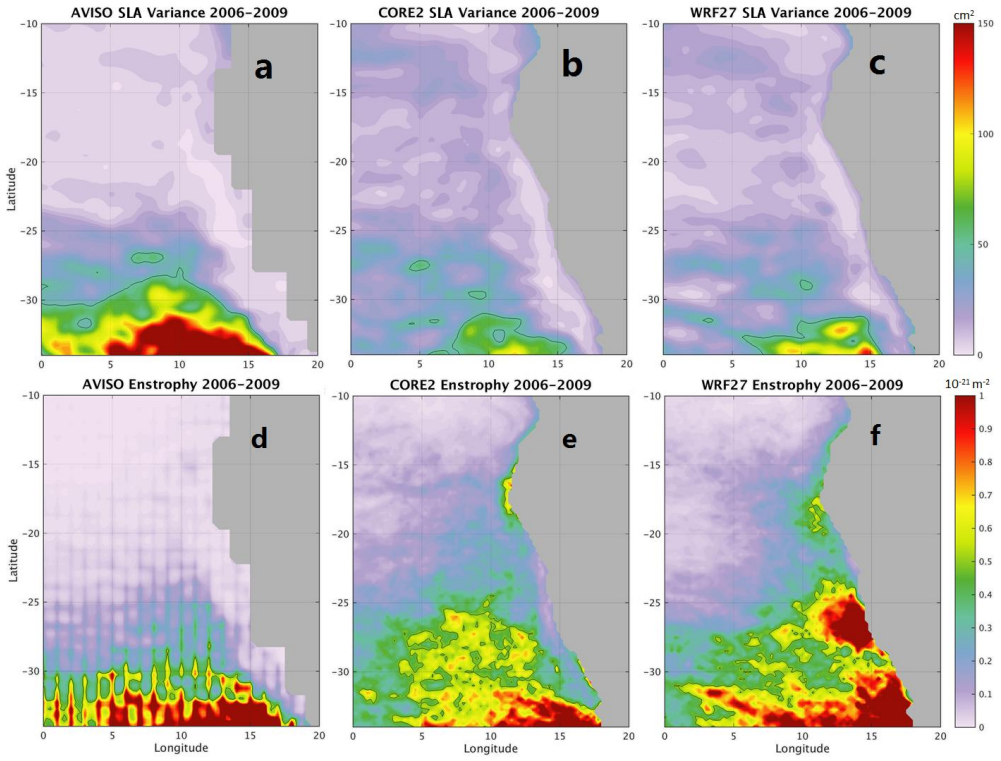

Fig.4.1 Top panel shows annual mean SLA variance (cm^2) from AVISO data (a), 3km_CORE2 run (b) and 3km_WRF27 run (c). Bottom panel shows annual mean enstrophy (m^{-2}) calculated from SLA from AVISO data (d), 3km_CORE2 run (e) and 3km_WRF27 run (f). Both SLA variance and enstrophy are averaged for 2006-2009 period.

To further reveal eddy activity in the SETA region, enstrophy is computed and compared between observation and model simulations (Fig.4.1d-f). Enstrophy calculated from the AVISO data (Fig.4.1d) shows strong similarity to the SLA variance field, with high values to south of 30^{o}S. However, enstrophy patterns in the model simulations are different from those of the SLA variance. In the 3km_CORE2 run, the enstrophy has high values along the coast to the north of 20^{o}S, including the ABF region, in addition to the high value region in the southernmost SETA area. In the 3km_WRF27 run, the enstrophy shows similar structure to that of the 3km_CORE2 run north of 20^{o}S, except

that it extends further offshore. However, in the Benguela upwelling region, a very different structure emerges with high enstrophy values near the Lüderitz Upwelling Cell (26^{o}S) and near the coast of the Agulhas Leakage region. This finding suggests that eddies in the coastal region of the SETA are sensitive to the fine structure of coastal wind forcing. We further note that the fact that the SLA variance and enstrophy show different distributions in the model simulations suggests that eddies along the coast have smaller spatial scales than those in the offshore region of the Agulhas Leakage. This is because a small scale eddy tends to have small SLA magnitude, which can result in a small SLA variance, but the horizontal gradient of SLA may still be significant and cause a large enstrophy (see Section 4.2.1).

From Fig.4.1, it is evident that the simulated enstrophy is different from that in the observations. This difference may be partially explained by the different resolutions between observation and model simulations. Along the coast, eddies are likely to be generated by frontal instability of the ABF and Benguela upwelling front and thus can be highly sensitive to the local wind forcing. These coastal eddies tend to have shallow vertical structures and small spatial scales compared to eddies of the Agulhas Leakage in the southernmost part of the SETA region. Therefore, the $1/4^{o}$ AVISO product that is based on multiple satellite altimeter images and heavily smoothed may not be able to resolve these coastal eddies. These eddies may thus be completely absent in the AVISO data, even when using enstrophy as a measure of eddy activity. In contrast, the 3 km ROMS simulations explicitly resolve such eddies and their activity is readily captured by enstrophy because of their small spatial structures.

Even though direct satellite observations cannot confirm the existence of the coastal eddies, existing in situ observations have revealed these coastal eddy activities. For example, in situ observations of Stander (1964) and Filippov and Kolesnikov (1971) show strong eddy signatures near the ABF, and Chen et al. (2012) shows evidence of energetic eddies near the Lüderitz Upwelling Cell. Collectively, these existing in situ and satellite observations do offer support to the simulated eddy activity in the 3km_WRF27 run.

The shallow and strong ageostrophic eddy activity induced by the inner coastal wind forcing can potentially be captured by the coastal SST. Therefore, we also use the Reynolds SST data to calculate its variance and compare it with the model results (Fig.4.2). Since SST has a very strong seasonality, we first subtracted the seasonal mean SST from the original SST and then calculated the variance. Reynolds satellite data demonstrates a large SST variance along the coast near the ABF region (SST variance $>2^{o}C^{2}$). In the 3 km ROMS experiments, both runs have large SST variance along the coast of ABF, but the area is smaller than that in Reynolds SST. In the 3km_WRF27 run, SST variance appears to be larger near the Lüderitz Upwelling Cell region, which differs from Reynolds. In both Reynolds SST and the 3km_CORE2 run, SST variance is small near the Lüderitz Upwelling Cell. It seems that the 3km_CORE2 run has a better representation of the observed SST variance and ocean eddies in the Lüderitz Upwelling Cell region, but this could be an artifact of the coarse resolution of Reynolds SST data.

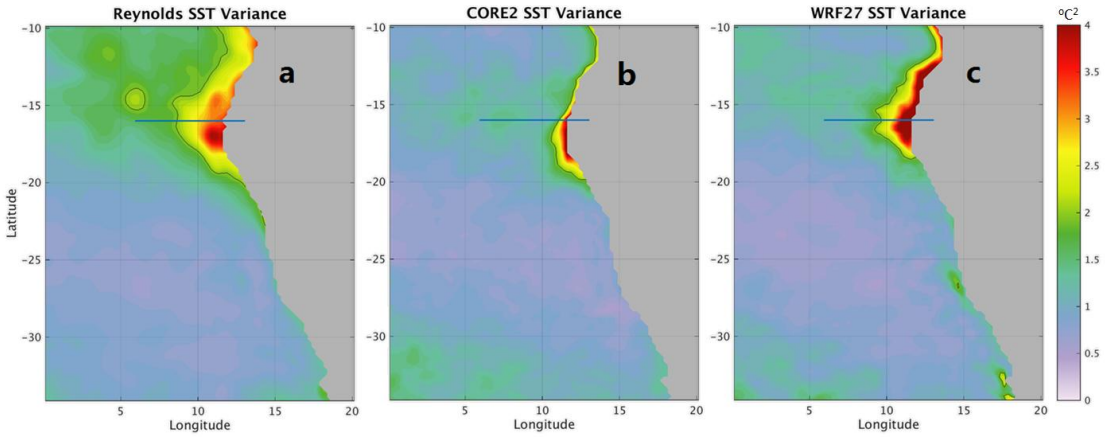

Fig.4.2 Annual mean SST variance ($^oC^2$) from the Reynolds SST data (a), 3km_CORE run (b) and 3km_WRF27 run (c). All data averaged for 2006-2009 period.

Since the spatial resolutions of both AVISO SLA and Reynolds SST datasets are still relatively coarse, to show whether increasing the resolution can further influence the eddy behavior, we use the $1/12^o$ resolution HYCOM data to evaluate the simulated SLA and SST (Fig.4.3). The SLA and SST variances in both runs are similar to those of the last four years. The HYCOM SLA variance is also similar to the satellite observed fields, with more fine structures being observed. However, the HYCOM SST variance appears to be different from Reynolds SST, with a smaller variance near the ABF region, and larger variance in the Lüderitz Upwelling Cell region. In this case, SST variance of the 3km_WRF27 run is closer to the HYCOM data. We therefore suggest that changing the ocean grid resolution from $1/4^o$ to $1/12^o$ can revolve more fine structure eddies. Since the HYCOM data is not an observation product, its credibility is questionable. However, since there is no other global observation that has a resolution finer than $1/4^o$ to the best of our knowledge, we can only use the comparisons shown in this section to validate the simulated eddies.

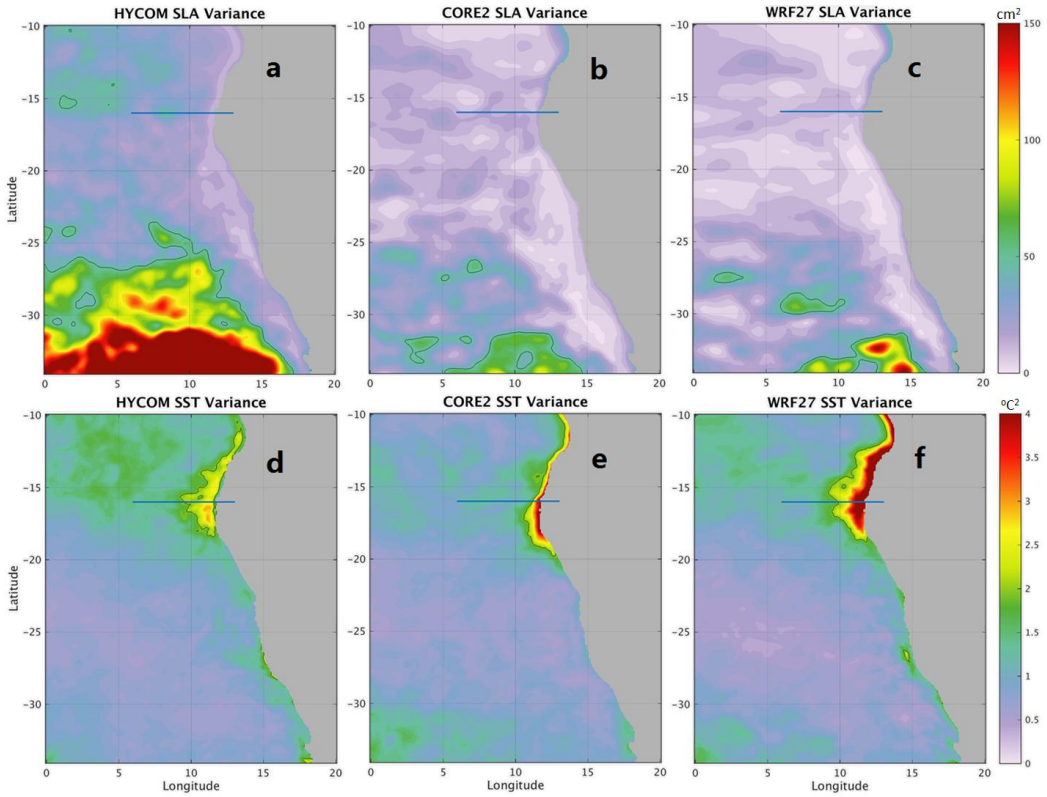

Fig.4.3 Top panel shows annual mean SLA variance (cm^2) from HYCOM data (a), 3km_CORE2 run (b) and 3km_WRF27 run (c). Bottom panel shows annual mean SST variance ($^oC^2$) from HYCOM SST data (a), 3km_CORE run (b) and 3km_WRF27 run (c). All data averaged for 2008-2009 period.

4.3.2 Impact of Wind Forcing on Ocean Eddy Statistics

As shown in the previous chapter, the coastal circulation system along the Angola-Benguela coast is sensitive to the detailed structure of the coastal winds, particularly the double core structure of the BLLCJ. As such, we expect that the simulated ocean eddy activity is also sensitive to the winds. To illustrate this sensitivity, we compare EKEs from both 3km_CORE and 3km_WRF27 runs.

Fig.4.4 compares the annual mean EKE averaged over the top 10 m from both runs and the depth where EKE reaches 50 cm^2/s^2. Fig.4.5 and Fig.4.6 show similar maps for

each of the four seasons to reveal the seasonality of EKE and eddy depth. There are three regions where eddies are most active: one is near and to the north of the ABF (hereafter referred to as ABF-eddying region), the other is in the vicinity of the Lüderitz Upwelling Cell (LUC-eddying region) and finally the third area is located in the Agulhas influx region (AIF-eddying region).

In the ABF-eddying region, the two experiments share similar annual mean EKE patterns (Fig.4.4a and b). Strong surface EKE (> 100 cm^2/s^2) can be observed in both coastal and off-shore regions, where EKE reaches a high value of 300 cm^2/s^2 along the coast. Strong eddies in this region tend to be very shallow in the off-shore region, reaching only about 50 m (Fig.4.4c and d). However, within a narrow band along the coast the influence of eddy activity can reach 150 m or deeper. One difference between the two simulations is that eddies near the ABF are stronger and have deeper structures in the 3klm_CORE2 run than in the 3km_WRF27 run. The seasonality of EKE from both simulations is also similar, showing stronger amplitude during austral summer and fall (Fig.4.5a, b, e and f) and weaker during winter and spring (Fig.4.5c, d, g and h). Eddies near the ABF are more energetic and have deeper structure in the 3km_CORE2 run than the 3km_WRF27 run for all seasons except for austral winter.

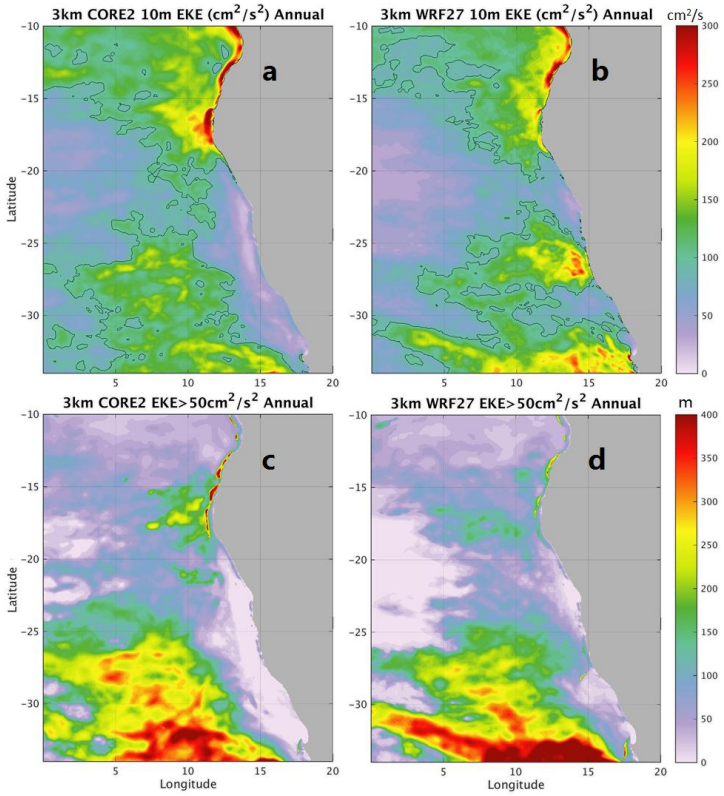

Fig.4.4 Top panel shows annual mean EKE (cm^2/s^2) averaged over the surface 10 m, from the 3km_CORE2 run (a) and the 3km_WRF27 run (b). Bottom panel shows the depth (m) where annual mean EKE>50 cm^2/s^2, from the 3km_CORE2 run (c) and the 3km_WRF27 run (d). All data averaged for 2006-2009 period.

The difference between the two simulations is more striking in the LUC-eddying region and AIF-eddying region. The annual mean EKE and its depth in the WRF-forced run show local maxima in these two regions, but the 3km_CORE2 run shows no such features. The seasonality of EKE is also different between two runs. In the 3km_CORE2 run, EKE along the coast remains to be very weak in all seasons with no deep structures (Fig.4.5a, b, c and d and Fig.4.6a, b, c and d). In contrast, the WRF-forced run shows strong EKE values with significant depth structures in these two regions in all seasons except for the austral winter. The absence of strong eddy activities in these regions in

the 3km_CORE2 run is likely related to the weak upwelling along the Benguela coast as shown in Chapter 3, which reduces the instability along the upwelling front, and suppresses the eddy activities.

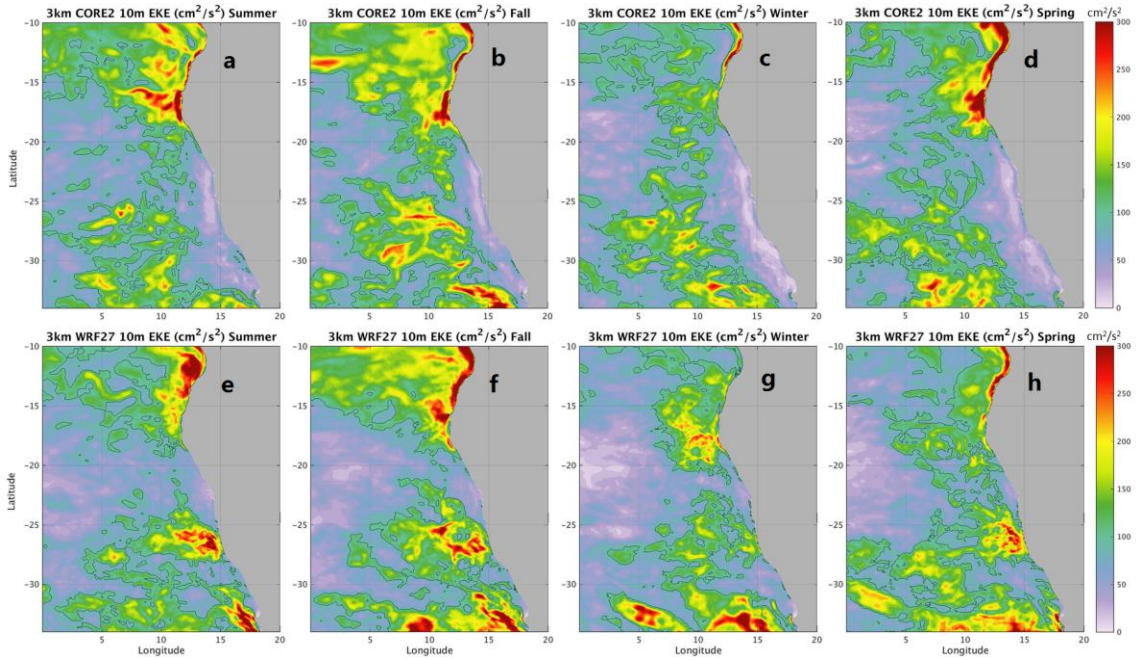

Fig.4.5 Seasonal mean EKE (cm^2/s^2) averaged over the surface 10 m from the 3km_CORE2 run (top panel) and the 3km_WRF27 run (bottom panel), in austral summer (first column), fall (second column), winter (third column) and spring (fourth column). All data averaged for 2006-2009 period.

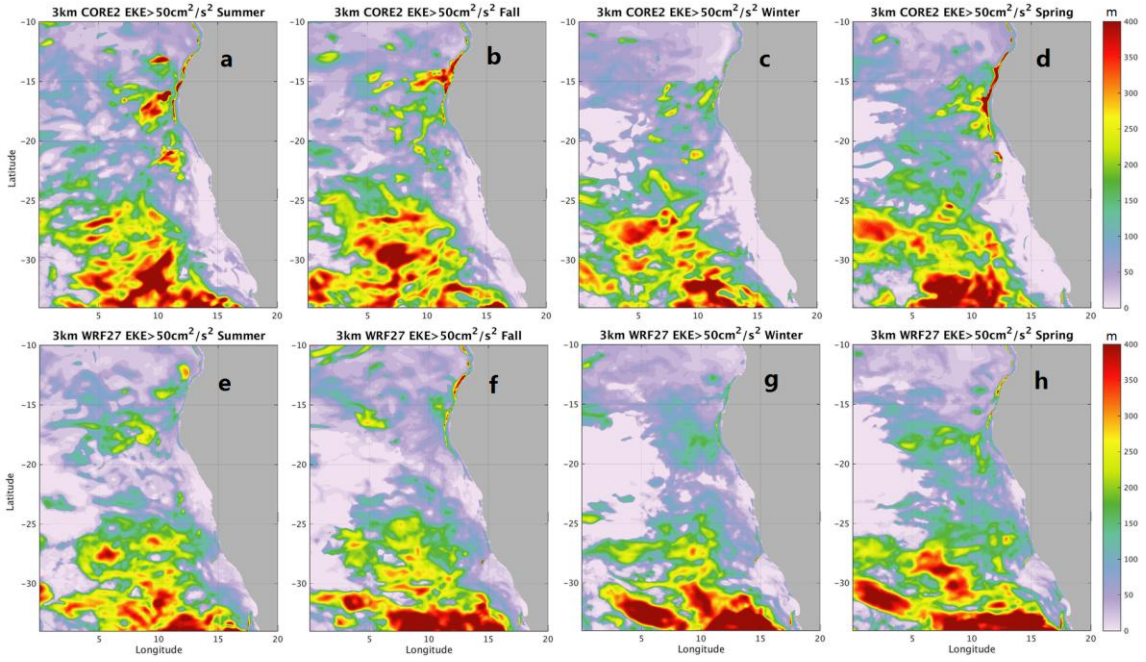

Fig.4.6 Depth (m) where seasonal mean EKE>50 cm^2/s^2 from the 3km_CORE2 run (top panel) and the 3km_WRF27 run (bottom panel), in austral summer (first column), fall (second column), winter (third column) and spring (fourth column). All data averaged for 2006-2009 period.

Recall that in Chapter 3, we showed that near the ABF-eddying region the poleward Angola Current is significantly stronger in the CORE2-forced run than in the WRF-forced run. This difference is attributed to the WSC structure between the coarse-resolution CORE2 winds and high-resolution WRF27 winds. We hypothesize that the stronger EKE in the CORE2-forced run near the ABF-eddying region is related to the much stronger Angola Current in this run than in the WRF-forced run. Further analysis that is beyond the scope of this study is needed to validate this hypothesis. Similarly, near the LUC-eddying and AIF-eddying region the WRF-forced run produces much stronger equatorward Benguela Current than the CORE2-forced run does. This difference is also attributed to the difference between the CORE2 winds and WRF27

winds. We reason that the much stronger Benguela Current in the WRF-forced run is also responsible for the stronger eddy activity in these regions compared to the CORE2-forced run. Therefore, we conclude that the primary reason for the different eddy activities between the two simulations is the different coastal wind structure. This implies that the role of eddies in heat transport is also different between the two experiments, which will be explored next.

4.4 Heat Budget Analysis

4.4.1 Eddy Heat Transport

EHT is a vector with a meridional component $T'v'$ and a zonal component $T'u'$, which indicates the strength and direction of the heat transported by eddies. Heat transport induced by eddies and mean flow is compared along three zonal cross-sections within the ABF-eddying region (16^{o}S), LUC-eddying region (26^{o}S) and AIF-eddying region (32^{o}S) for the upper 300 m.

Along 16^{o}S (Fig.4.7), strong heat transport is mainly confined within the top 150 m. In the 3km_CORE2 run, a strong westward EHT (>0.04^{o}C*m/s) dominates the upper 50 m within 1-2^o of the coast with a deeper but weaker extension into the open ocean. A strong eastward EHT (>0.04^{o}C*m/s) dominates the upper 100 m in the off-shore region. Therefore, a strong convergence of EHT is expected near 10-11^{o}E. At this latitude, strong meridional EHT mainly resides within the upper 50 m in the 3km_CORE2 run, with an extremely strong southward EHT (>0.06^{o}C*m/s) within 100 km of the coast and weaker southward transport off-shore. Northward EHT is much weaker than the

southward transport and only appears as small patches (<0.02^{o}C*m/s) in the subsurface. In contrast, the 3km_WRF27 run shows much weaker and shallower zonal EHT than in the 3km_CORE2 run, with a small region of eastward EHT (>0.02^{o}C*m/s) near the coast and westward EHT (0.02^{o}C*m/s) off-shore, suggesting a divergence of EHT near 8^{o}E. The meridional EHT in the 3km_WRF27 run, however, is similar to that in the 3km_CORE2 run, with a very strong and narrow southward EHT near the coast and much weaker values off-shore. Mean flow heat transports in both experiments are more than one order of magnitude stronger than eddy-induced components and shows similar structures along 16^{o}S. Zonally, the mean flow at this latitude transports heat westward almost uniformly, and is especially strong (>2^{o}C*m/s) in the surface 20 m, suggesting a weak convergence/divergence of mean flow heat transport. The mean flow heat transport extends deeper and further offshore in the 3km_WRF27 run than in the 3km_CORE2 run, consistent with the finding in Chapter 3 that the ABF, where offshore transport is strong, is better represented in the WRF-forced run. The meridional transport is mainly southward with the strongest value near the coast in both runs. However, it is stronger in the 3km_CORE2 run (4^{o}C*m/s) than in then 3km_WRF27 run (2^{o}C*m/s). In sum, along 16^{o}S, mean flow heat transports dominate over eddy. The meridional component of the mean flow heat transport is particularly strong in the 3km_CORE2 run, consistent with the result in Chapter 3 that the simulated Angola Current overshoots the ABF and produces unrealistically strong southward transport in that experiment. For the zonal component, both runs show much weaker spatial variations, despite of much higher values, compared to the EHT. This suggests that even though EHT's values are order of

magnitude weaker than that of the mean flow heat transport, EHT may still make an important contribute to the convergence/divergence of heat transport that ultimately affect temperature changes in the region.

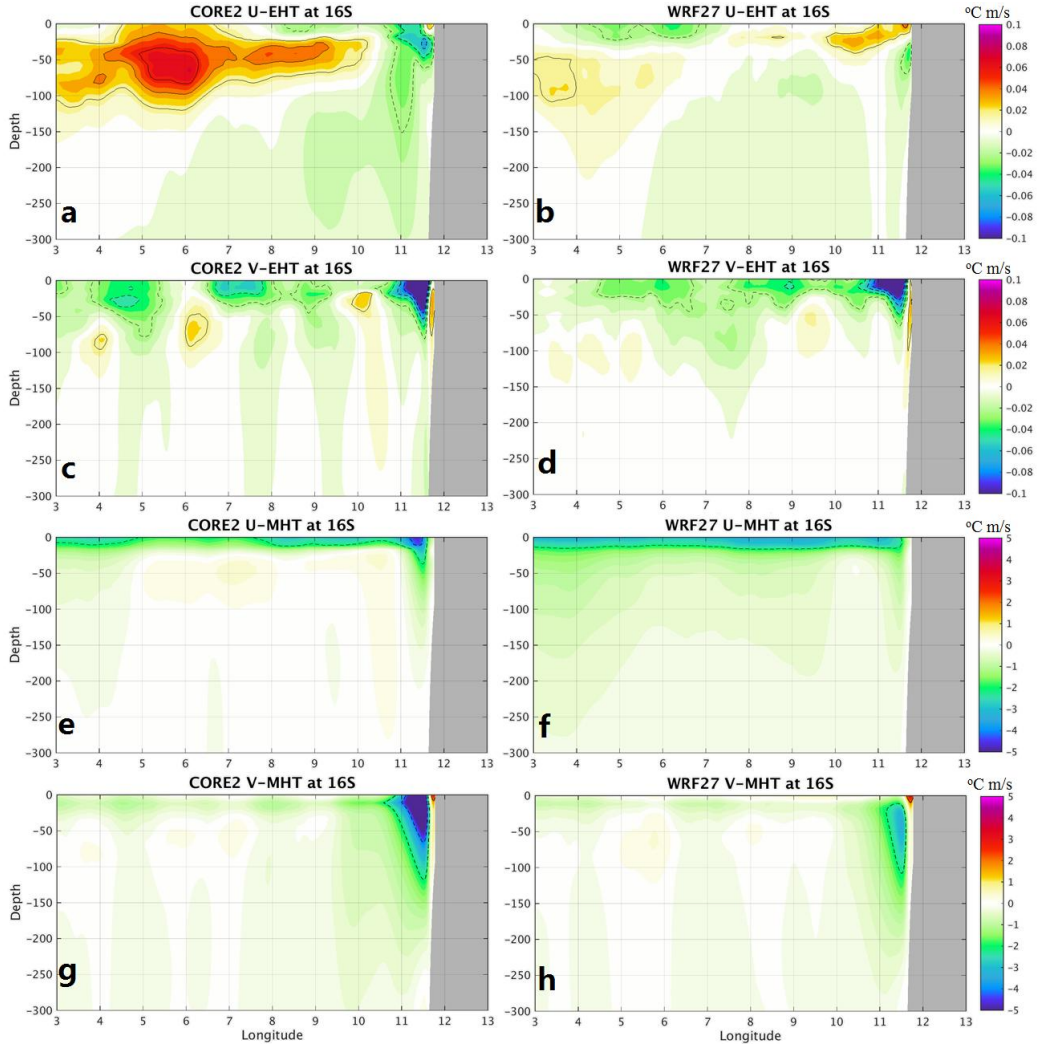

Fig.4.7 Annual mean heat transport (^{o}C*m/s) along 16^{o}S. Top panel shows zonal EHT, second panel shows meridional EHT, third panel show zonal mean flow heat transport and bottom panel shows meridional mean flow heat transport, in the 3km_CORE2 run (left column) and the 3km_WRF27 run (right column). All data averaged for 2006-2009 period

Along 26^{o}S (Fig.4.8), mean flow heat transports are still order of magnitude stronger than EHT values in both runs. However, there are strong differences between the two runs for both mean and eddy transports. The most significant difference occurs in the meridional component of the mean flow heat transport near the coast, which shows opposite directions between the two runs with a southward (northward) transport in the 3km_CORE2 (3km_WRF27) run. This is again consistent with the result shown in Chapter 3 that the Angola Current overshoots the ABF in the CORE2-forced run, continuing transporting heat poleward at this latitude. In contrast, equatorward Benguela Current is generated in the 3km_WRF27 run, which transports the heat northward near the coast. The zonal component of EHT at 26^{o}S is also different between the two runs with a much stronger eastward EHT in the 3km_WRF27 run compared to the 3km_CORE2 run. It suggests that in the 3km_WRF27 run EHT acts to warm the coastal region, counteracting the cooling due to the offshore mean flow heat transport induced by Ekman upwelling. This is again consistent with the results in Chapter 3, which show that the upwelling circulation near the Lüderitz Upwelling Cell is severely underestimated in the CORE2-forced run.

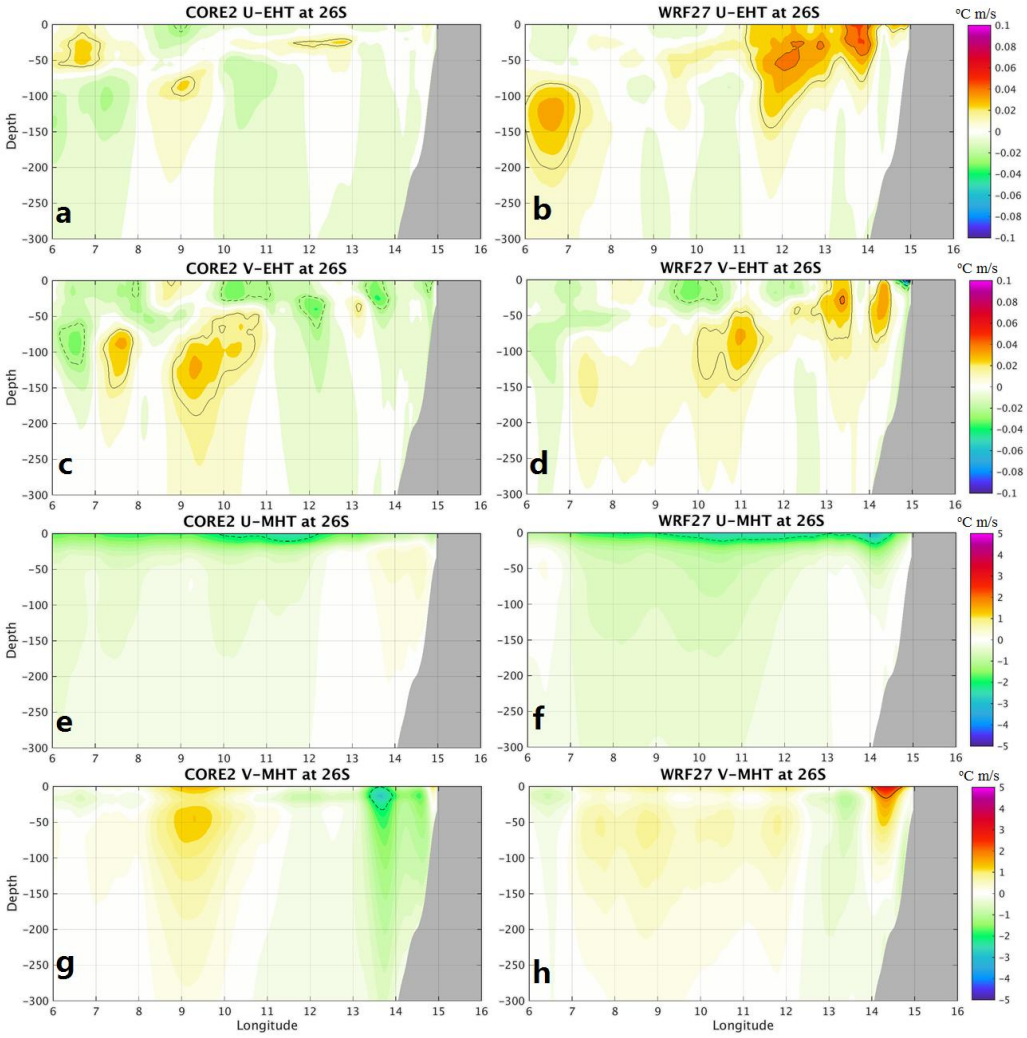

Fig.4.8 Annual mean heat transport (^{o}C*m/s) along 26^{o}S. Top panel shows zonal EHT, second panel shows meridional EHT, third panel show zonal mean flow heat transport and bottom panel shows meridional mean flow heat transport, in the 3km_CORE2 run (left column) and the 3km_WRF27 run (right column). All data averaged for 2006-2009 period.

Finally, along 32^{o}S (Fig.4.9), the results are similar to those along 26^{o}S: The near-coast mean meridional heat transport is southward in the 3km_CORE2 run, but northward in the 3km_WRF27 run; the ETH is considerably stronger in the 3km_WRF27 run than in the 3km_CORE2 run, and overall mean flow heat transports

dominates over ETH. Therefore, these analyses indicate that 1) ocean heat transport in the SETA region is dominated by mean flow heat transports, particularly within the upper ocean, 2) both mean flow heat transport and EHT are sensitive to the detailed structure of local atmospheric forcing, 3) EHT, albeit having much weaker strength, exhibits more spatial variations than mean flow heat transport, and thus may still generate significant local heat transport convergence and divergence, contributing to local heat budget.

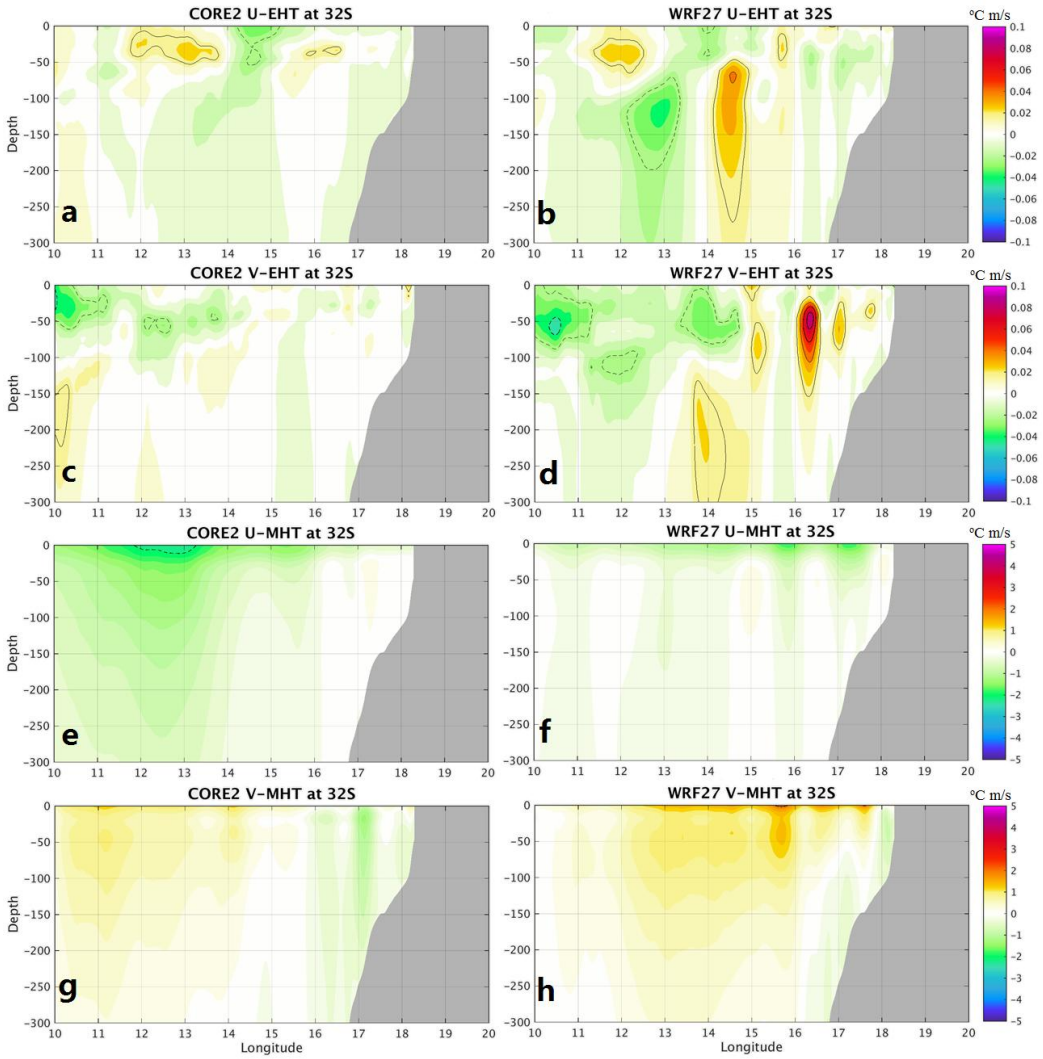

Fig.4.9 Annual mean heat transport (^{o}C*m/s) along 32^{o}S. Top panel shows zonal EHT, second panel shows meridional EHT, third panel show zonal mean flow heat transport and bottom panel shows meridional mean flow heat transport, in the 3km_CORE2 run (left column) and the 3km_WRF27 run (right column). All data averaged for 2006-2009 period.

4.4.2 Double-time Averaged Eddy and Mean Flow Advections

In order to use the DTA method for the heat budget analysis, we first checked the heat balance of the 3 km resolution experiments. Similar to Fig.3.18, Fig.4.10 also compares the differences of true temperature (Fig.4.10a), double-time averaged

temperature tendency (Fig.4.10b), total advection (Fig.4.10c) and total diffusion (Fig.4.10d) between the 3km_CORE2 run and the 3km_WRF27 run. The true annual mean temperature and double-time averaged temperature tendency are almost identical with each other, which verifies the feasibility of DTA method in analyzing the 3 km resolution experiments. Meanwhile, it is total advection that works to increase the SST bias and total diffusion to work against the coastal warming due to advection.

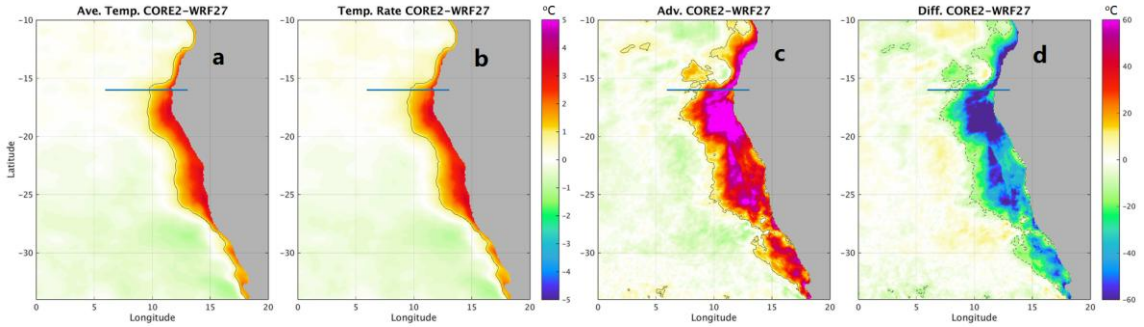

Fig.4.10 True temperature difference (^{o}C) between 3km_CORE2 and 3km_WRF27 runs is shown in panel (a). Difference of double time averaged (DTA) temperature tendency (dT/dt; ^{o}C) between 9km_CORE2 and 9km_WRF27 runs is shown in panel (b). Difference of total advection (c) and total diffusion (d) are shown in other panels. All data shown here is averaged for upper 20 m depth and have units of ^{o}C.

To further examine the contribution of mean and eddy heat transport to heat budget, we calculate total advective heat flux by mean flow and eddies, which is based on the divergence of mean flow and eddy heat transport:

$$Q_{eddy} = -\int_{z_0}^{0} \nabla \cdot \overline{\boldsymbol{V}'T'} \quad (15)$$

$$Q_{mean} = -\int_{z_0}^{0} \nabla \cdot \overline{\boldsymbol{V}}\overline{T} \quad (16)$$

where Q_{eddy} and Q_{mean} are eddy and mean flow head advection, respectively. The overbar indicates the average value over the analyzed time period, and the prime means the deviation from seasonal mean value. z_0 indicates the depth from which the vertical integration starts. Differences of Q_{adv}, Q_{mean} and Q_{eddy} between the 3km_CORE2 run and the 3km_WRF27 run are calculated in this section using DTA method (Fig.4.11). All terms are averaged over the upper 20 m to keep consistency with Chapter 3.

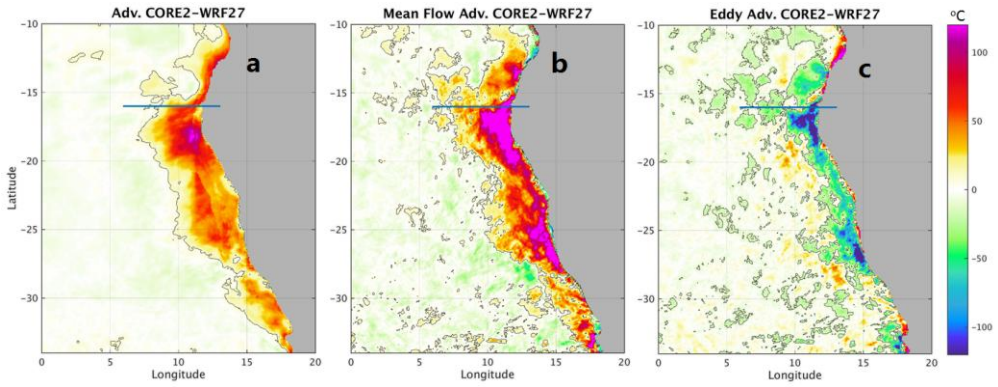

Fig.4.11 Heat budget difference (°C) between the 3km_CORE2 run and the 3km_WRF27 run for total advection (a), mean flow advection (b) and eddy advection (c). All heat budget terms are calculated using DTA method to 2005-2009 period.

Fig.4.11b shows large positive mean flow advection difference (>100°C) in the inner coastal region. Such difference is also strongest at the ABF and Lüderitz Upwelling Cell regions. This suggests that the mean flow advection has positive contribution to the SST difference between the 3km_CORE2 run and the 3km_WRF27 run and such contribution is very sensitive to the surface wind forcing. Fig.4.11c then shows large negative difference (<-100°C) of eddy advection. The eddy advection difference feature is very much alike the mean flow difference, but with negative values,

which reveals that eddy mainly works against the mean flow advection and the warm SST bias. Notice that although both mean flow advection and eddy advection have large magnitude, their summation, the total heat advection (Fig.4.11a), is compensated by diffusion, and finally causes the temperature difference of 1-3^{o}C in the coastal region (Fig.4.10a).

The total diffusion term can also be further decomposed into net downward radiative heat flux (Q_{net}) and vertical mixing term (Q_{mix}), which are shown in Fig.4.12. In the coastal region, the net radiative heat flux term provides less heat into the ocean in the 3km_CORE2 run than in the 3km_WRF27 run. This is because the higher temperature in the 3km_CORE2 run will result in stronger longwave radiation, sensible heat flux and latent heat flux, which means more cooling due to radiation. On the other hand, vertical mixing has a strong positive contribution of ~60^{o}C to the warm SST bias along the coast of ABF and Lüderitz Upwelling Cell regions, while has a weak negative contribution of ~-20^{o}C in the off-shore region.

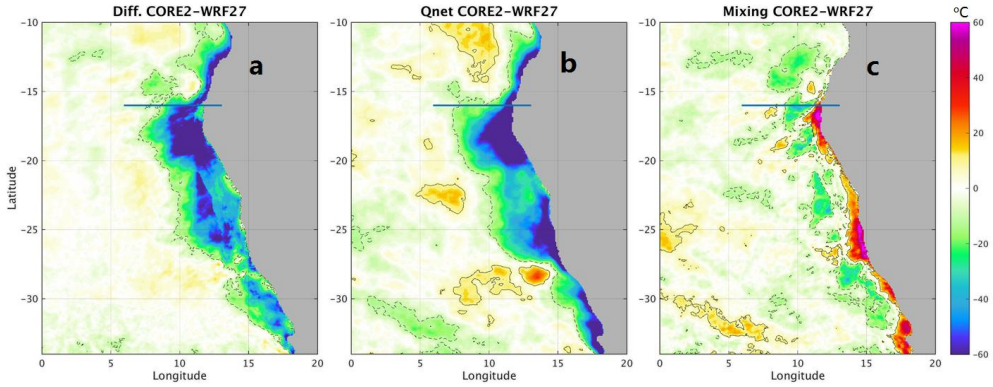

Fig.4.12 Heat budget difference (^{o}C) between the 3km_CORE2 run and the 3km_WRF27 run for total diffusion (a), net radiative heat flux (b) and vertical mixing (c). All heat budget terms are calculated using DTA method to 2005-2009 period.

4.5 Conclusion and Discussion

In this chapter, we analyzed the 3 km resolution ROMS model simulations forced by the coarse resolution CORE2 and fine resolution WRF27 winds, and showed general eddy statistics in the SETA region. Eddies are mainly strongest in the ABF, Lüderitz Upwelling Cell and Agulhas Leakage regions. In the ABF and Lüderitz Upwelling Cell regions, strong eddies are mainly at the surface ocean, and the strongest wind forcing region, which suggests that eddies in these regions are highly sensitive to wind. In the southern region, eddies tend to be strong and deep, and under the influence of the Agulhas Leakage.

Furthermore, eddy advection and mean flow advection were separated from the total advection. Comparison between the two experiments shows that it is mainly the mean flow that contributes to the warm SST bias. The difference of eddy advection is mainly negative in the SST bias region, suggesting that eddies have an opposite influence on the SST bias, mainly as compensation to the mean flow advection.

Furthermore, net radiative heat flux responses to the warm SST bias and causes more cooling doe to longwave radiation, sensible heat flux and latent heat flux. Vertical mixing, on the other hand, works to increase the bias in the inner-coastal region, while has a weak cooling effect off-shore.

However, as argued in Chapter 3, ocean model resolution also influences the SST bias, but it is unclear whether resolving eddies is the main reason. In this study, only the 3 km resolution ROMS experiments have daily output frequency, while all other experiments have 10-day output. This renders the 3 km resolution experiments incomparable to the other experiments. Therefore, further studies need to be pursued to quantify the heat advection by the mean flow and that by eddies in ocean models with different resolutions but same atmospheric forcing.

Some other issues also need further examining. First, the seasonal mean method that we used to define eddies is not accurate, though it is the most widely used method. In fact, the deviation from seasonal mean still contains large scale signals such as the seasonal cycle. Therefore, in future works, a wavelet filter that subtracts the seasonal cycle from the original field needs to be applied to define eddies. This way, the contribution of the mean flow and that of eddies can be more accurately quantified.

Finally, since this study mainly focuses on the contribution of heat budget terms to the SST bias, all DTA analyses are carried out within the surface 20 m. However, as shown in Section 3.4, temperature biases also appear in the subsurface. Therefore, it is also worth further studying how each of the budget terms, including mean flow and eddy advections, can influence such subsurface temperature biases, i.e. as a function of depth.

CHAPTER V

CONCLUSIONS AND FUTURE WORK

A series of experiments have been performed using ROMS model with ocean resolutions ranging from 81, 27, 9 to 3 km to test the impact of ocean model horizontal resolution on the warm SST bias in the SETA region. For each ocean model resolution, the experiments are forced with coarse resolution CORE2 winds and fine resolution WRF simulated winds, in order to show the influence of surface wind forcing, especially the spatial structure of BLLCJ, on the SST bias.

Comparisons between Reynolds satellite SST data and the ROMS experiments show that the application of high resolution WRF simulated wind has successfully reduced the SST bias in the SETA region, which suggests that increasing the spatial resolution of the wind forcing is of first order importance for reducing the SST bias. For the same WRF forcing, the SST bias is reduced upon switching the ocean model resolution from 27 km to 9 km, though the magnitude. On the other hand, there is no noticeable reduction of the bias upon increasing the resolution from 9 km to 3km. This suggests that the horizontal ocean model resolution is of second order importance to the SST bias in the SETA region.

Application of Sverdrup balance further relates the spatial structure of wind forcing to the SST bias. When the BLLCJ core is located further off-shore, the WSC in the inner coastal region will be weak and broad, which exceeds the region where boundary friction and non-linear processes are effective, therefore the Sverdrup balance will hold

and induce a poleward overshoot of the warm Angola Current across the ABF region, and causes the bias. When the BLLCJ core is located near the coast, the WSC will be strong and confined to the coast, which causes the Sverdrup balance to break down, and to suppress the SST bias.

The off-shore Ekman transport induces coastal divergence and upwelling. Therefore, coastal upwelling is highly sensitive to the along-shore wind stress. The off-shore Ekman transport will also induce an elevation of sea surface height in the off-shore region, and induce a down-wind geostrophic flow. Thus, when the equatorward along-shore wind stress is weak (such as in the CORE2 wind), both upwelling and the geostrophic flow will be weakened, which would bring less cold water from deep ocean to the surface, as well as from higher latitudes to lower latitudes. On the other hand, Ekman divergence is also caused by WSC, which can cause upwelling further off-shore. To summarize, deficiencies in the magnitude of the wind stress, as well as the pattern and magnitude of the WSC can readily lead to the SST bias. A high resolution wind product that can resolve the fine features of the BLLCJ is thus important for simulating the SST field in the SETA region.

Contribution of total advection is compared to total diffusion using DTA method. The difference of total advection between the CORE2-forced and WRF-forced experiments dominates the SST bias by creating the warm SST bias in the first place. The diffusive process then works to counteract with advective processes by removing the warm SST bias through surface heat flux damping and vertical and horizontal mixing.

Eddy statistics are calculated for the CORE2- and WRF27-forced experiments. In the ABF, Lüderitz Upwelling Cell and Agulhas Leakage regions, strong eddy activities can be located in the WRF27-forced run. In the CORE2-forced run, strong eddy activities are mainly in the ABF and Agulhas Leakage regions, suggesting the eddies may be sensitive to the surface wind forcing.

To further decompose the total advection term, contribution of mean flow and eddy advection is also quantified using DTA method. Difference of mean flow advection between the CORE2- and WRF27 forced runs works to increase the warm SST bias, while eddy advection difference counteract with mean flow advection, which buffers the formation of SST bias. In addition, vertical mixing is also an important contributor to the warm SST bias in the inner-coastal region.

This study subtracts seasonal mean values from the original temperature and velocity fields to define eddy. However, taking a seasonal mean may still leave some low frequency signals in the eddy field. Therefore, eddies should be more accurately defined using the wavelet filter method, which subtracts the seasonal cycle from the original value, and leaves very weak mean flow signals in the eddy field. Moreover, comparison of eddy vs. mean flow advection should also be done to other experiments with different ocean resolutions. To keep consistency with the 3 km resolution ROMS model, other experiments should be rerun and output daily. Finally, contribution of each heat budget term within different depths needs to be further examined because 1) the temperature bias does not only appear at the surface, but also in the subsurface, and 2) mean flow and eddy advections may have different sensitivity to the depths, therefore

the conclusions based on their contributions to the surface ocean cannot be applied to the subsurface.

REFERENCES

Becker, J. J., Sandwell, D. T., Smith, W. H. F., Braud, J., Binder, B., Depner, J., ... & Ladner, R. (2009). Global bathymetry and elevation data at 30 arc seconds resolution: SRTM30_PLUS. Marine Geodesy, 32(4), 355-371.

Beckmann, A., Böning, C. W., Köberle, C., & Willebrand, J. (1994). Effects of increased horizontal resolution in a simulation of the North Atlantic Ocean. Journal of physical oceanography, 24(2), 326-344.

Bettencourt, J. H., López, C., & Hernández-García, E. (2012). Oceanic three-dimensional Lagrangian coherent structures: A study of a mesoscale eddy in the Benguela upwelling region. Ocean Modelling, 51, 73-83.

Bonjean, F., & Lagerloef, G. S. (2002). Diagnostic model and analysis of the surface currents in the tropical Pacific Ocean. Journal of Physical Oceanography, 32(10), 2938-2954.

Breugem, W. P., Chang, P., Jang, C. J., Mignot, J., & Hazeleger, W. (2008). Barrier layers and tropical Atlantic SST biases in coupled GCMs. Tellus A, 60(5), 885-897.

Capet, X. J., Marchesiello, P., & McWilliams, J. C. (2004). Upwelling response to coastal wind profiles. Geophysical Research Letters, 31(13).

Capet, X., Colas, F., McWilliams, J. C., Penven, P., & Marchesiello, P. (2008a). Eddies in eastern boundary subtropical upwelling systems. Ocean Modeling in an Eddying Regime, 131-147.

Capet, X., McWilliams, J. C., Molemaker, M. J., & Shchepetkin, A. F. (2008b). Mesoscale to submesoscale transition in the California Current System. Part I: Flow

structure, eddy flux, and observational tests. Journal of physical oceanography, 38(1), 29-43.

Capet, A., Mason, E., Rossi, V., Troupin, C., Faugere, Y., Pujol, I., & Pascual, A. (2014). Implications of refined altimetry on estimates of mesoscale activity and eddy‐driven offshore transport in the Eastern Boundary Upwelling Systems. Geophysical Research Letters, 41(21), 7602-7610.

Chaigneau, A., Gizolme, A., & Grados, C. (2008). Mesoscale eddies off Peru in altimeter records: Identification algorithms and eddy spatio-temporal patterns. Progress in Oceanography, 79(2-4), 106-119.

Chang, C. Y., Carton, J. A., Grodsky, S. A., & Nigam, S. (2007). Seasonal climate of the tropical Atlantic sector in the NCAR Community Climate System Model 3: Error structure and probable causes of errors. Journal of Climate, 20(6), 1053-1070.

Chapman, D. C. (1985). Numerical treatment of cross-shelf open boundaries in a barotropic coastal ocean model. Journal of Physical oceanography, 15(8), 1060-1075.

Chelton, D. B., Deszoeke, R. A., Schlax, M. G., El Naggar, K., & Siwertz, N. (1998). Geographical variability of the first baroclinic Rossby radius of deformation. Journal of Physical Oceanography, 28(3), 433-460.

Chen, Z., Yan, X. H., Jo, Y. H., Jiang, L., & Jiang, Y. (2012). A study of Benguela upwelling system using different upwelling indices derived from remotely sensed data. Continental shelf research, 45, 27-33.

Chiang, J. C., & Lintner, B. R. (2005). Mechanisms of remote tropical surface warming during El Niño. Journal of climate, 18(20), 4130-4149.

Chiang, J. C., & Sobel, A. H. (2002). Tropical tropospheric temperature variations caused by ENSO and their influence on the remote tropical climate. Journal of climate, 15(18), 2616-2631.

Colas, F., McWilliams, J. C., Capet, X., & Kurian, J. (2012). Heat balance and eddies in the Peru-Chile current system. Climate dynamics, 39(1-2), 509-529.

Colas, F., Capet, X., McWilliams, J. C., & Li, Z. (2013). Mesoscale eddy buoyancy flux and eddy-induced circulation in Eastern Boundary Currents. Journal of Physical Oceanography, 43(6), 1073-1095.

Colberg, F., & Reason, C. J. C. (2006). A model study of the Angola Benguela Frontal Zone: Sensitivity to atmospheric forcing. Geophysical research letters, 33(19).

Defant, A. (1961). Physical oceanography vol. 1. Pergamon press.

Delworth, T. L., Rosati, A., Anderson, W., Adcroft, A. J., Balaji, V., Benson, R., Dixon, K., Griffies, S. M., Lee, H. C., Pacanowski, R. C. and Vecchi, G. A. (2012). Simulated climate and climate change in the GFDL CM2. 5 high-resolution coupled climate model. Journal of Climate, 25(8), 2755-2781.

Deser, C., Phillips, A. S., & Alexander, M. A. (2010). Twentieth century tropical sea surface temperature trends revisited. Geophysical Research Letters, 37(10).

De Szoeke, S. P., Yuter, S., Mechem, D., Fairall, C. W., Burleyson, C. D., & Zuidema, P. (2012). Observations of stratocumulus clouds and their effect on the eastern Pacific surface heat budget along 20 S. Journal of Climate, 25(24), 8542-8567.

Ding, H., Keenlyside, N., Latif, M., Park, W., & Wahl, S. (2015). The impact of mean state errors on equatorial Atlantic interannual variability in a climate model. Journal of Geophysical Research: Oceans, 120(2), 1133-1151.

Doi, T., Vecchi, G. A., Rosati, A. J., & Delworth, T. L. (2012). Biases in the Atlantic ITCZ in seasonal–interannual variations for a coarse-and a high-resolution coupled climate model. Journal of Climate, 25(16), 5494-5511.

Dong, C., McWilliams, J. C., Liu, Y., & Chen, D. (2014). Global heat and salt transports by eddy movement. Nature communications, 5, 3294.

Ekman, V. W. (1905). On the influence of the earth's rotation on ocean-currents.

Enriquez, A. G., & Friehe, C. A. (1995). Effects of wind stress and wind stress curl variability on coastal upwelling. Journal of Physical Oceanography, 25(7), 1651-1671.

Fairall, C. W., Bradley, E. F., Hare, J. E., Grachev, A. A., & Edson, J. B. (2003). Bulk parameterization of air–sea fluxes: Updates and verification for the COARE algorithm. Journal of climate, 16(4), 571-591.

Fennel, W., Junker, T., Schmidt, M., & Mohrholz, V. (2012). Response of the Benguela upwelling systems to spatial variations in the wind stress. Continental Shelf Research, 45, 65-77.

Filippov, E. A., & Kolesnikov, G. I. (1971). On the origin of southward components of the Benguela current system. Trudy Atlantniro, 33, 42-49.

Flather, R. A. (1976). A tidal model of the northwest European continental shelf. Mem. Soc. Roy. Sci. Liege, 10, 141-164.

Florenchie, P., Lutjeharms, J. R., Reason, C. J. C., Masson, S., & Rouault, M. (2003). The source of Benguela Niños in the south Atlantic Ocean. Geophysical Research Letters, 30(10).

Fu, L. L. (1981). The general circulation and meridional heat transport of the subtropical South Atlantic determined by inverse methods. Journal of Physical Oceanography, 11(9), 1171-1193.

Gent, P. R., Yeager, S. G., Neale, R. B., Levis, S., & Bailey, D. A. (2010). Improvements in a half degree atmosphere/land version of the CCSM. Climate Dynamics, 34(6), 819-833.

Grodsky, S. A., Carton, J. A., Nigam, S., & Okumura, Y. M. (2012). Tropical Atlantic biases in CCSM4. Journal of Climate, 25(11), 3684-3701.

Gruber, N., Lachkar, Z., Frenzel, H., Marchesiello, P., Münnich, M., McWilliams, J. C., ... & Plattner, G. K. (2011). Eddy-induced reduction of biological production in eastern boundary upwelling systems. Nature geoscience, 4(11), 787.

Haidvogel, D. B., Arango, H., Budgell, W. P., Cornuelle, B. D., Curchitser, E., Di Lorenzo, E., ... & Levin, J. (2008). Ocean forecasting in terrain-following coordinates: Formulation and skill assessment of the Regional Ocean Modeling System. Journal of Computational Physics, 227(7), 3595-3624.

Hopkins, J., Lucas, M., Dufau, C., Sutton, M., Stum, J., Lauret, O., & Channelliere, C. (2013). Detection and variability of the Congo River plume from satellite derived sea surface temperature, salinity, ocean colour and sea level. Remote sensing of environment, 139, 365-385.

Huang, B., Hu, Z. Z., & Jha, B. (2007). Evolution of model systematic errors in the tropical Atlantic basin from coupled climate hindcasts. Climate dynamics, 28(7-8), 661-682.

Hurlburt, H. E., & Thompson, J. D. (1973). Coastal upwelling on a β-plane. Journal of Physical Oceanography, 3(1), 16-32.

Isachsen, P. E., Koszalka, I., & LaCasce, J. H. (2012). Observed and modeled surface eddy heat fluxes in the eastern Nordic Seas. Journal of Geophysical Research: Oceans, 117(C8).

Jayne, S. R., & Marotzke, J. (2002). The oceanic eddy heat transport. Journal of Physical Oceanography, 32(12), 3328-3345.

Junker, T. (2014). Response of the Benguela upwelling system to changes in the wind forcing (Doctoral dissertation).

Kopte, R., Brandt, P., Dengler, M., Tchipalanga, P. C. M., Macuéria, M., & Ostrowski, M. (2017). The Angola Current: Flow and hydrographic characteristics as observed at 11 °S. Journal of Geophysical Research: Oceans, 122(2), 1177-1189.

Large, W. G., McWilliams, J. C., & Doney, S. C. (1994). Oceanic vertical mixing: A review and a model with a nonlocal boundary layer parameterization. Reviews of Geophysics, 32(4), 363-403.

Large, W. G., & Danabasoglu, G. (2006). Attribution and impacts of upper-ocean biases in CCSM3. Journal of Climate, 19(11), 2325-2346.

Large, W. G. & Yeager, S. G. (2008). CORE. 2 global air-sea flux dataset. National Center for Atmospheric Research Computational and Information Systems Laboratory Research Data Archive, doi, 10, D6WH2N0S.

Lass, H. U., Schmidt, M., Mohrholz, V., & Nausch, G. (2000). Hydrographic and current measurements in the area of the Angola–Benguela Front. Journal of Physical Oceanography, 30(10), 2589-2609.

Lemarié, F., Kurian, J., Shchepetkin, A. F., Molemaker, M. J., Colas, F., & McWilliams, J. C. (2012). Are there inescapable issues prohibiting the use of terrain-following coordinates in climate models?. Ocean Modelling, 42, 57-79.

Lübbecke, J. F., Böning, C. W., Keenlyside, N. S., & Xie, S. P. (2010). On the connection between Benguela and equatorial Atlantic Niños and the role of the South Atlantic Anticyclone. Journal of Geophysical Research: Oceans, 115(C9).

Lumpkin, R., & Johnson, G. C. (2013). Global ocean surface velocities from drifters: Mean, variance, El Niño–Southern Oscillation response, and seasonal cycle. Journal of Geophysical Research: Oceans, 118(6), 2992-3006.

Ma, C. C., Mechoso, C. R., Robertson, A. W., & Arakawa, A. (1996). Peruvian stratus clouds and the tropical Pacific circulation: A coupled ocean-atmosphere GCM study. Journal of Climate, 9(7), 1635-1645.

Madec, G. (2008). NEMO ocean engine: Note du Pôle de modélisation de l'Institut Pierre-Simon Laplace No 27.

Marchesiello, P., McWilliams, J. C., & Shchepetkin, A. (2003). Equilibrium structure and dynamics of the California Current System. Journal of Physical Oceanography, 33(4), 753-783.

McClean, J. L., Bader, D. C., Bryan, F. O., Maltrud, M. E., Dennis, J. M., Mirin, A. A., Jones, P. W., Kim, Y. Y., Ivanova, D. P., Vertenstein, M. and Boyle, J. S. (2011). A prototype two-decade fully-coupled fine-resolution CCSM simulation. Ocean Modelling, 39(1-2), 10-30.

McCreary, J. P., & Chao, S. Y. (1985). Three-dimensional shelf circulation along an eastern ocean boundary. Journal of marine research, 43(1), 13-36.

McCreary, J. P., Kundu, P. K., & Chao, S. Y. (1987). On the dynamics of the California Current System. Journal of Marine Research, 45(1), 1-32.

Meeuwis, J. M., & Lutjeharms, J. R. E. (1990). Surface thermal characteristics of the Angola-Benguela front. South African Journal of Marine Science, 9(1), 261-279.

Mohrholz, V., Schmidt, M., Lutjeharms, J. R. E., & John, H. C. (2004). Space–time behaviour of the Angola–Benguela Frontal Zone during the Benguela Niño of April 1999. International Journal of Remote Sensing, 25(7-8), 1337-1340.

Nicholson, S. E. (2010). A low-level jet along the Benguela coast, an integral part of the Benguela current ecosystem. Climatic Change, 99(3), 613-624.

Nigam, S. (1997). The annual warm to cold phase transition in the eastern equatorial Pacific: Diagnosis of the role of stratus cloud-top cooling. Journal of climate, 10(10), 2447-2467.

Oerder, V., Colas, F., Echevin, V., Masson, S., Hourdin, C., Jullien, S., ... & Lemarié, F. (2016). Mesoscale SST–wind stress coupling in the Peru–Chile current system: Which mechanisms drive its seasonal variability?. Climate dynamics, 47(7-8), 2309-2330.

Parish, T. R. (2000). Forcing of the summertime low-level jet along the California coast. Journal of Applied Meteorology, 39(12), 2421-2433.

Patricola, C. M., & Chang, P. (2017). Structure and dynamics of the Benguela low-level coastal jet. Climate Dynamics, 49(7-8), 2765-2788.

Pedlosky, J. (2013). Geophysical fluid dynamics. Springer Science & Business Media.

Qiu, B., & Kelly, K. A. (1993). Upper-ocean heat balance in the Kuroshio Extension region. Journal of physical oceanography, 23(9), 2027-2041.

Rae, C. M., Garzoli, S. L., & Gordon, A. L. (1996). The eddy field of the southeast Atlantic Ocean: A statistical census from the Benguela Sources and Transports Project. Journal of Geophysical Research: Oceans, 101(C5), 11949-11964.

Reid, J. L., Nowlin Jr, W. D., & Patzert, W. C. (1977). On the characteristics and circulation of the southwestern Atlantic Ocean. Journal of Physical Oceanography, 7(1), 62-91.

Reid, J. L. (1989). On the total geostrophic circulation of the South Atlantic Ocean: Flow patterns, tracers, and transports. Progress in Oceanography, 23(3), 149-244.

Renault, L., Dewitte, B., Marchesiello, P., Illig, S., Echevin, V., Cambon, G., ... & Ayers, J. K. (2012). Upwelling response to atmospheric coastal jets off central Chile: A

modeling study of the October 2000 event. Journal of Geophysical Research: Oceans, 117(C2).

Reynolds, R. W., Smith, T. M., Liu, C., Chelton, D. B., Casey, K. S., & Schlax, M. G. (2007). Daily high-resolution-blended analyses for sea surface temperature. Journal of Climate, 20(22), 5473-5496.

Richter, I., Behera, S. K., Masumoto, Y., Taguchi, B., Komori, N., & Yamagata, T. (2010). On the triggering of Benguela Niños: Remote equatorial versus local influences. Geophysical Research Letters, 37(20).

Richter, I., Xie, S. P., Behera, S. K., Doi, T., & Masumoto, Y. (2014). Equatorial Atlantic variability and its relation to mean state biases in CMIP5. Climate dynamics, 42(1-2), 171-188.

Richter, I. (2015). Climate model biases in the eastern tropical oceans: Causes, impacts and ways forward. Wiley Interdisciplinary Reviews: Climate Change, 6(3), 345-358.

Risien, C. M., Reason, C. J. C., Shillington, F. A., & Chelton, D. B. (2004). Variability in satellite winds over the Benguela upwelling system during 1999–2000. Journal of Geophysical Research: Oceans, 109(C3).

Risien, C. M., & Chelton, D. B. (2008). A global climatology of surface wind and wind stress fields from eight years of QuikSCAT scatterometer data. Journal of Physical Oceanography, 38(11), 2379-2413.

Rodrigues, R. R., & Lorenzzetti, J. A. (2001). A numerical study of the effects of bottom topography and coastline geometry on the Southeast Brazilian coastal upwelling. Continental Shelf Research, 21(4), 371-394.

Roemmich, D., & Gilson, J. (2001). Eddy transport of heat and thermocline waters in the North Pacific: A key to interannual/decadal climate variability?. Journal of Physical Oceanography, 31(3), 675-687.

Rossi, V., López, C., Sudre, J., Hernández - Garcia, E., & Garçon, V. (2008). Comparative study of mixing and biological activity of the Benguela and Canary upwelling systems. Geophysical Research Letters, 35(11).

Rubio, A., Blanke, B., Speich, S., Grima, N., & Roy, C. (2009). Mesoscale eddy activity in the southern Benguela upwelling system from satellite altimetry and model data. Progress in Oceanography, 83(1), 288-295.

Saha, S., Moorthi, S., Pan, H. L., Wu, X., Wang, J., Nadiga, S., ... & Liu, H. (2010). NCEP Climate Forecast System Reanalysis (CFSR) 6-hourly Products, January 1979 to December 2010. Research Data Archive at the National Center for Atmospheric Research, Computational and Information Systems Laboratory, Boulder, CO.

Samelson, R. M. (1992). Supercritical marine-layer flow along a smoothly varying coastline. Journal of the atmospheric sciences, 49(17), 1571-1584.

Schneider, R. R., Müller, P. J., Ruhland, G., Meinecke, G., Schmidt, H., & Wefer, G. (1996). Late Quaternary surface temperatures and productivity in the east-equatorial South Atlantic: Response to changes in trade/monsoon wind forcing and surface water advection. In The South Atlantic (pp. 527-551). Springer, Berlin, Heidelberg.

Seo, H., Jochum, M., Murtugudde, R., & Miller, A. J. (2006). Effect of ocean mesoscale variability on the mean state of tropical Atlantic climate. Geophysical research letters, 33(9).

Shannon, L. V., Boyd, A. J., Brundrit, G. B., & Taunton-Clark, J. (1986). On the existence of an El Niño-type phenomenon in the Benguela system. Journal of Marine Research, 44(3), 495-520.

Shannon, L. V., Agenbag, J. J., & Buys, M. E. L. (1987). Large-and mesoscale features of the Angola-Benguela front. South African Journal of Marine Science, 5(1), 11-34.

Shannon, L. V., Lutjeharms, J. R. E., & Agenbag, J. J. (1989). Episodic input of sub-Antarctic water into the Benguela region. South African Journal of Science, 85(5), 317-322.

Shannon, L. V., & Nelson, G. (1996). The Benguela: large scale features and processes and system variability. In The South Atlantic (pp. 163-210). Springer, Berlin, Heidelberg.

Shchepetkin, A. F., & McWilliams, J. C. (2005). The regional oceanic modeling system (ROMS): a split-explicit, free-surface, topography-following-coordinate oceanic model. Ocean Modelling, 9(4), 347-404.

Shchepetkin, A. F., & McWilliams, J. C. (2009). Correction and commentary for "Ocean forecasting in terrain-following coordinates: Formulation and skill assessment of the regional ocean modeling system" by Haidvogel et al., J. Comp. Phys. 227, pp. 3595–3624. Journal of Computational Physics, 228(24), 8985-9000.

Sikirić, M. D., Janeković, I., & Kuzmić, M. (2009). A new approach to bathymetry smoothing in sigma-coordinate ocean models. Ocean Modelling, 29(2), 128-136.

Skamarock, W. C., and Coauthors, (2008). A Description of the Advanced Research WRF Version 3. NCAR Technical Note NCAR/TN-475+STR, doi:10.5065/D68S4MVH.

Small, R. J., Curchitser, E., Hedstrom, K., Kauffman, B., & Large, W. G. (2015). The Benguela upwelling system: Quantifying the sensitivity to resolution and coastal wind representation in a global climate model. Journal of Climate, 28(23), 9409-9432.

Smith, R. L. (1968). Upwelling. Oceanogr. Mar. Biol. Ann. Rev., 6, 11-46.

Stander, G. H. (1964). The Benguela Current off South West Africa. Investl Rep. mar. Res. Lab. S.w. Afr. 12: 43 pp. + Plates 5-81.

Stramma, L., & Peterson, R. G. (1989). Geostrophic transport in the Benguela Current region. Journal of Physical Oceanography, 19(10), 1440-1448.

Stramma, L., & Peterson, R. G. (1990). The South Atlantic Current. Journal of Physical Oceanography, 20(6), 846-859.

Sverdrup, H. U. (1947). Wind-driven currents in a baroclinic ocean; with application to the equatorial currents of the eastern Pacific. Proceedings of the National Academy of Sciences, 33(11), 318-326.

Taylor, K. E., Stouffer, R. J., & Meehl, G. A. (2012). An overview of CMIP5 and the experiment design. Bulletin of the American Meteorological Society, 93(4), 485-498.

Tchipalanga, P., Dengler, M., Brandt, P., Kopte, R., Macuéria, M., Coelho, P., ... & Keenlyside, N. S. (2018). Eastern boundary circulation and hydrography off Angola–building Angolan oceanographic capacities. Bulletin of the American Meteorological Society, (2018).

Toniazzo, T., Mechoso, C. R., Shaffrey, L. C., & Slingo, J. M. (2010). Upper-ocean heat budget and ocean eddy transport in the south-east Pacific in a high-resolution coupled model. Climate dynamics, 35(7-8), 1309-1329.

Trani, M., Falco, P., & Zambianchi, E. (2011). Near-surface eddy dynamics in the Southern Ocean. Polar Research, 30(1), 11203.

Tsuchiya, M. (1985). Evidence of a double-cell subtropical gyre in the South Atlantic Ocean. Journal of Marine Research, 43(1), 57-65.

Veitch, J., Penven, P., & Shillington, F. (2010). Modeling equilibrium dynamics of the Benguela Current System. Journal of Physical Oceanography, 40(9), 1942-1964.

Volkov, D. L., Lee, T., & Fu, L. L. (2008). Eddy‐induced meridional heat transport in the ocean. Geophysical Research Letters, 35(20).

Wahl, S. (2009). The Tropical Atlantic SST Bias in the Kiel Climate Model (Doctoral dissertation, Christian-Albrechts-Universität).

Wahl, S., Latif, M., Park, W., & Keenlyside, N. (2011). On the tropical Atlantic SST warm bias in the Kiel climate model. Climate Dynamics, 36(5-6), 891-906.

Weeks, S. J., Barlow, R., Roy, C., & Shillington, F. A. (2006). Remotely sensed variability of temperature and chlorophyll in the southern Benguela: upwelling

frequency and phytoplankton response. African Journal of Marine Science, 28(3-4), 493-509.

White, R. H., & Toumi, R. (2014). River flow and ocean temperatures: The Congo River. Journal of Geophysical Research: Oceans, 119(4), 2501-2517.

Wunsch, C. (2011). The decadal mean ocean circulation and Sverdrup balance. Journal of Marine Research, 69(2-3), 417-434.

Xu, Z., Li, M., Patricola, C. M., & Chang, P. (2014a). Oceanic origin of southeast tropical Atlantic biases. Climate dynamics, 43(11), 2915-2930.

Xu, Z., Chang, P., Richter, I., & Tang, G. (2014b). Diagnosing southeast tropical Atlantic SST and ocean circulation biases in the CMIP5 ensemble. Climate dynamics, 43(11), 3123-3145.

Yu, L., Weller, R. A., & Sun, B. (2004). Mean and variability of the WHOI daily latent and sensible heat fluxes at in situ flux measurement sites in the Atlantic Ocean. Journal of climate, 17(11), 2096-2118.

Yu, J. Y., & Mechoso, C. R. (1999). A discussion on the errors in the surface heat fluxes simulated by a coupled GCM. Journal of climate, 12(2), 416-426.

Zhang, Z., Wang, W., & Qiu, B. (2014). Oceanic mass transport by mesoscale eddies. Science, 345(6194), 322-324.

Zebiak, S. E. (1993). Air–sea interaction in the equatorial Atlantic region. Journal of Climate, 6(8), 1567-1586.